

TECHNICAL REPORT 1924
June 2005

Sea-Surface Specular Multipath for Surface-Level Antennas: Phase 1

J. C. Allen
R. E. Goshorn
SSC San Diego

B. Zeidler
Adaptive Dynamics, Inc.

A. A. Beex
Virginia Tech

Approved for public release;
distribution is unlimited.

SSC San Diego

Report Documentation Page				Form Approved OMB No. 0704-0188	
Public reporting burden for the collection of information is estimated to average 1 hour per response, including the time for reviewing instructions, searching existing data sources, gathering and maintaining the data needed, and completing and reviewing the collection of information. Send comments regarding this burden estimate or any other aspect of this collection of information, including suggestions for reducing this burden, to Washington Headquarters Services, Directorate for Information Operations and Reports, 1215 Jefferson Davis Highway, Suite 1204, Arlington VA 22202-4302. Respondents should be aware that notwithstanding any other provision of law, no person shall be subject to a penalty for failing to comply with a collection of information if it does not display a currently valid OMB control number.					
1. REPORT DATE JUN 2005		2. REPORT TYPE		3. DATES COVERED -	
4. TITLE AND SUBTITLE Sea-Surface Specular Multipath for Surface-Level Antennas: Phase 1				5a. CONTRACT NUMBER	
				5b. GRANT NUMBER	
				5c. PROGRAM ELEMENT NUMBER	
6. AUTHOR(S)				5d. PROJECT NUMBER	
				5e. TASK NUMBER	
				5f. WORK UNIT NUMBER	
7. PERFORMING ORGANIZATION NAME(S) AND ADDRESS(ES) SPAWAR Systems Center ,San Diego,CA,92152-5001				8. PERFORMING ORGANIZATION REPORT NUMBER	
9. SPONSORING/MONITORING AGENCY NAME(S) AND ADDRESS(ES)				10. SPONSOR/MONITOR'S ACRONYM(S)	
				11. SPONSOR/MONITOR'S REPORT NUMBER(S)	
12. DISTRIBUTION/AVAILABILITY STATEMENT Approved for public release; distribution unlimited					
13. SUPPLEMENTARY NOTES The original document contains color images.					
14. ABSTRACT see report					
15. SUBJECT TERMS					
16. SECURITY CLASSIFICATION OF:			17. LIMITATION OF ABSTRACT	18. NUMBER OF PAGES 88	19a. NAME OF RESPONSIBLE PERSON
a. REPORT unclassified	b. ABSTRACT unclassified	c. THIS PAGE unclassified			

TECHNICAL REPORT 1924
June 2005

Sea-Surface Specular Multipath for Surface-Level Antennas: Phase 1

J. C. Allen
R. E. Goshorn
SSC San Diego

B. Zeidler
Adaptive Dynamics, Inc.

A. A. Beex
Virginia Tech

Approved for public release;
distribution is unlimited.



SSC San Diego
San Diego, CA 92152-5001

EXECUTIVE SUMMARY

This document describes a specular multipath simulation for antennas located close to a sea surface. The antennas are circularly polarized but the ray-trace implementation readily accommodates any other polarizations. The transmitted signal $s_T(t)$ arrives at the receiver's antenna along the direct path and from multiple reflections off the sea surface. The surface-level antenna turns the multipath into *multiplicative noise*—assuming the receiver is narrow band. Under this narrow-band assumption, the received signal $s_R(t)$ is approximated by modulating the transmitted signal $s_T(t)$ with this multiplicative noise:

$$s_R(t) = a(t) \times s_T(t).$$

The multiplicative noise $\{a(t)\}$ is determined by the sea surface, the elevation angle of the transmitted signal path, and the receiver's antenna. By sweeping over various realizations of the sea surfaces, elevation angles, and various antenna heights and speeds, the systems engineer can estimate sea-surface specular multipath effects on the surface-to-satellite link.

Contents

1	Time-Varying Random Channels	1
2	In-Plane Scattering	2
3	Flat-Surface Scattering	4
3.1	Time Delays	7
3.2	Antenna Gains	7
3.3	Reflected Path	8
3.4	Diffuse Scatter	13
3.5	Specular Scattering at a Surface-Level Antenna	14
4	Antenna Patterns	17
4.1	Baseline Quadrifilar Pattern	18
4.2	Electronically Reconfigurable Antenna (ERA) Patterns	19
4.3	OE-538 Patterns	21
4.4	Antenna Mismatch	27
5	Sea Surfaces	28
6	Scattering From Sea-Surface Slices	35
6.1	Flat-Surface Blending	38
6.2	Reflecting Points	39
6.3	Time Delay	40
6.4	Reflected Angles	42
6.5	Scattering Examples	43
7	Specular Multipath Noise Simulations	49
7.1	Baseline Quadrifilar Antenna	49
7.2	OE-538 Antenna	56
7.3	Multipath Phase	60
7.4	Multipath Correlation	63
7.5	Multipath Envelope	66
8	Modeling Issues	70
A	Back Reflections	73

List of Figures

1	Coordinates for incident and reflected polarizations of the electric field.	3
2	Direct path, specular reflection, and diffuse scatter.	4
3	Specular reflection and diffuse scatter off a slightly rough surface. . .	5
4	Rayleigh criterion (blue) at 1-meter wavelength in the θ_T - σ_ζ plane. . .	6
5	Time-Delay geometry for elevation angle $\theta_T \leq 45^\circ$	7
6	Time delays for a short mast and flat reflections.	8
7	Vertical reflection coefficient for seawater.	10
8	Horizontal reflection coefficient for seawater.	10
9	Circular reflection coefficient for seawater.	12
10	Cross-circular reflection coefficient for seawater.	13
11	Surface roughness coefficient.	15
12	Diffuse scatter power σ_g^2 as a function of wind speed.	16
13	Electronically Reconfigurable SATCOM Antenna (courtesy of Toyon Research Corporation).	17
14	Measured gain as a function of elevation angle for a resonant quadrifilar helix [38].	18
15	Toyon's low-beam ERA at 250 MHz (courtesy of Toyon Research Corporation).	19
16	Toyon's low-beam ERA at 310 MHz (courtesy of Toyon Research Corporation).	20
17	E_ϕ at 300 MHz for High-Angle OE-538 antenna (courtesy of NUWC).	21
18	E_θ at 300 MHz for High-Angle OE-538 antenna (courtesy of NUWC).	22
19	E_ϕ at 300 MHz for Low-Angle OE-538 antenna (courtesy of NUWC).	23
20	E_θ at 300 MHz for Low-Angle OE-538 antenna (courtesy of NUWC).	24
21	E fields at 300 MHz for Low-Angle OE-538 (courtesy of NUWC). . .	25
22	Estimated RCP and LCP gain at 300 MHz for Low-Angle OE-538. . .	26
23	RCP reflecting from sea surface and received by non-ideal RCP antenna.	27
24	Sea-surface parameters.	29
25	Wavenumber spectrum (3-D display).	30
26	Wavenumber spectrum (top view).	31
27	Slices of Donelan-Pierson-Banner-Ryan spectrum; no capillaries. . . .	32
28	Gaussian sea surface.	33
29	Top view of Gaussian sea surface.	34
30	(a) Plane wave reflecting from flat surface; (b) plane wave reflecting from tangent planes.	35
31	Closeup of incident and reflecting rays that arrive in the antenna's aperture.	36
32	Gaussian sea slice and scattering points.	37
33	Sea surface reflecting a ray.	39
34	Time-delay geometry.	41

35	Range and delays of the sea surface; transmitter's elevation $\theta_T = 30^\circ$.	44
36	Range and delays of the sea surface; transmitter's elevation $\theta_T = 20^\circ$.	45
37	Range and delays of the sea surface; transmitter's elevation $\theta_T = 10^\circ$.	46
38	Range and delays of the sea surface; transmitter's elevation $\theta_T = 5^\circ$.	47
39	Baseline Quadrifilar Antenna DSR.	50
40	Sea-surface multipath; transmitter at 30° elevation; Baseline Quadrifilar Antenna.	50
41	Sea-surface multipath; transmitter at 10° elevation; Baseline Quadrifilar Antenna.	51
42	Sea-surface multipath; transmitter at 5° elevation; Baseline Quadrifilar Antenna.	51
43	Sea-surface multipath for the Baseline Quadrifilar Antenna.	52
44	Sea-surface realization with wind at 5 m/s.	53
45	Sea-surface multipath for the Baseline Quadrifilar Antenna; wind at 5 m/s.	54
46	Sea-surface multipath; Baseline Quadrifilar Antenna; wind at 1 m/s.	55
47	DSR for the OE-538	56
48	Sea-surface multipath for the OE-538 Low-Angle Antenna.	57
49	Sea-surface multipath for the OE-538 Low-Angle Antenna; wind at 5 m/s.	58
50	Sea-surface multipath for the OE-538 Low-Angle Antenna; wind at 1 m/s.	59
51	Multipath phase; baseline QHA; wind at 10 m/s.	60
52	Multipath phase; baseline QHA; wind at 5 m/s.	61
53	Multipath phase; baseline QHA; wind at 1 m/s.	62
54	Multipath correlation; baseline QHA; wind at 10 m/s.	63
55	Multipath correlation; baseline QHA; wind at 5 m/s.	64
56	Multipath correlation; baseline QHA; wind at 1 m/s.	65
57	Multipath probability density estimate; baseline QHA; wind at 10 m/s.	66
58	Multipath standard deviation estimate; Baseline QHA; wind at 10 m/s.	67
59	Rician GOF of the normalized multipath; baseline QHA; wind at 10 m/s.	68
60	Rician GOF of the normalized multipath—angles below 5° omitted; baseline QHA; wind at 10 m/s.	69
61	Measured GPS satellite SNR at a sea-level receiver.	72
62	Back reflection—upper ray.	73
63	Back reflection—lower ray.	74

List of Tables

1	Table of Notation.	ix
2	Gravity and capillary spectral variables for $\Phi(\mathbf{k})$	31
3	Reflection data: $f = 250$ (MHz); $\sigma_\zeta = 0.5028$ (m); $\theta_T = 30^\circ$	43
4	Reflection data: $f = 250$ (MHz); $\sigma_\zeta = 0.5028$ (m); $\theta_T = 5^\circ$	48

Table 1: Table of Notation.

CP	circularly polarized
RCP	right-handed circularly polarized
LCP	left-handed circularly polarized
$G_T(\theta)$	gain of the transmitter's antenna
$G_R(\theta)$	gain of the receiver's antenna
θ	elevation angle
θ_T	elevation angle to the transmitter
θ_g	grazing angle
θ_i	angle of incidence
θ_r	angle of reflection
Γ	surface reflection coefficient
Γ_0	plane surface reflection coefficient
$\Gamma_{0,V}$	plane surface reflection coefficient for vertical polarization
$\Gamma_{0,H}$	plane surface reflection coefficient for horizontal polarization
$\Gamma_{0,C}$	plane surface reflection coefficient for circular polarization
$\Gamma_{0,X}$	plane surface reflection coefficient for cross-circular polarization
h_R	height of the receiving antenna
h_R^+	upper height of the receiving antenna aperture
h_R^-	lower height of the receiving antenna aperture
λ_T	wavelength of the transmitted wave
p_T	polarization of the transmitter's antenna
p_R	polarization of the receiver's antenna
\mathbf{E}	complex electric field
E_H	horizontal component of \mathbf{E}
E_V	vertical component of \mathbf{E}
η	polarization efficiency
$s_T(t)$	transmitted signal
$s_R(t)$	received signal
$\zeta(\mathbf{r})$	height of the sea surface at \mathbf{r}
σ_ζ	standard deviation of the sea surface height
H_s	significant wave height
DSR	Direct-to-Specular Ratio
QHA	Quadrifilar Helix Antenna

1 Time-Varying Random Channels

Starting in the early 1960s, Bello [7] created a mathematical framework for random, *time-varying*¹ filters to model RF channels. This time-varying channel model maps the transmitted signal $s_T(t)$ to the received signal $s_R(t)$ as discussed by Bello [7], [8], [9], [10]:

$$s_R(t) = \int_{-\infty}^{\infty} h(t, t - \tau) s_T(\tau) d\tau.$$

The channel model $h(t, \tau)$ is called the *input delay-spread function*. A canonical example is the *Quadrature-Modulation Fading Simulator* [31], [35, pages 697–703]:

$$h(t, \tau) = \sum_{n=1}^N a_n(t) \delta(\tau - \tau_n).$$

In this model, the received signal is the sum of delayed and faded versions of the transmitted signal:

$$s_R(t) = \sum_{n=1}^N a_n(t) s_T(t - \tau_n).$$

Specific channels, such as the surface scattering channel, are described by the delays and fading processes. In particular, if the delays τ_n are **not** resolvable in the bandwidth f_B of the receiver, say

$$|\tau_n| \leq 10^{-6} f_B,$$

then the channel can be approximated as *multiplicative noise*:

$$s_R(t) \approx \left\{ \sum_{n=1}^N a_n(t) \right\} \times s_T(t). \quad (1)$$

This report simulates the multiplicative noise caused by the transmitted signal reflecting off a sea surface and received by a surface-level antenna.

Equation 1 is obtained by making several simplifying assumptions. Section 2 introduces the model assumptions that restrict us to *in-plane scattering*. Consequently, we only will scatter off a one-dimensional sea surface rather than a two-dimensional sea surface.

Scattering off a one-dimensional surface is still difficult—even for a signal bouncing off a flat surface, there is a mix of *specular* and *diffuse* scattering. Section 3 illustrates both types of scattering and discusses the restriction to specular scattering. The restriction to specular scattering offers a simple, qualitative simulation of the multipath noise.

¹Key terms are italicized.

Section 4 reviews several quadrifilar helical antenna patterns. An antenna model is developed that accounts for the circular polarization on the direct path and the cross-circular polarization that arrives from the sea-surface reflections. This model can be coupled to the flat-plane scattering to estimate the *direct-to-specular ratio* (DSR) that will benchmark the simulations.

Section 5 reviews the sea-surface models. The models are two-dimensional Gaussian surfaces obtained by filtering the sea-surface spectrum. Looking into the wind of a fully developed sea surface, we can see that in-plane scattering is a reasonable approximation. Therefore, by picking off a “slice” of a sea surface that points into the wind, we have a one-dimensional surface appropriate for in-plane scattering.

Section 6 adapts the flat-plane scattering of Section 3 to local tangent planes of the one-dimensional sea surface. That is, the scattering mechanism are little flat plates tangent to the sea surface that reflect a ray from the transmitter into the antenna aperture. This *specular multipath noise* is the multiplicative noise in Equation 1.

Section 7 applies this specular tangent-plane scattering to several sea surfaces and antennas. These simulations show that the specular multipath reflecting off a smooth sea surface follows the two-path DSR. This DSR depends, in part, on the receiving antenna. For the low-angle antennas used in the simulations, the bulk of the specular multipath arrives from the lower elevation angles ($\approx 10^\circ$). However, as the sea surface becomes less smooth, the specular multipath migrates into the upper elevation angles.

Section 8 emphasizes that this specular multipath model only obtains a qualitative model for Equation 1. The approximations made to obtain this qualitative model are non-trivial. Consequently, the temptation for endless tweaking is unbounded. Tweaking is kept in check by knowing how the approximations intertwine—a single small “improvement” does not “improve” the multipath model. Rather, all the approximations must be simultaneously tightened before the multipath model registers significant improvements. Such a shift in the modeling fidelity migrates this qualitative model into a full-up scattering model. Consequently, there is no middle ground in scattering—either a simple model is used with the understanding that the results are qualitative or a full-blown propagation model is used that accurately captures both the local scattering off the sea surface and the long-range propagation through the atmosphere and surface ducts.

2 In-Plane Scattering

Figure 1 illustrates an electric field scattering off a two-dimensional surface. The incident electric field is decomposed into a vertical component determined by the *incident plane* and the horizontal component orthogonal to the incident plane (right-hand rule). Likewise, the reflected electric field is decomposed into a vertical component in

the reflected plane and the horizontal component orthogonal to the *reflected plane*. If the transmitter is aimed orthogonal to the wave direction, the bulk of the scattering will stay near the incident plane. Equivalent descriptions of this “in-plane scattering” are as follows:

- The scattering is such that purely horizontal or purely vertical polarization is not depolarized.
- There is only longitudinal scattering—not lateral scattering.
- The normal to any reflecting plane lies in the plane of incidence.

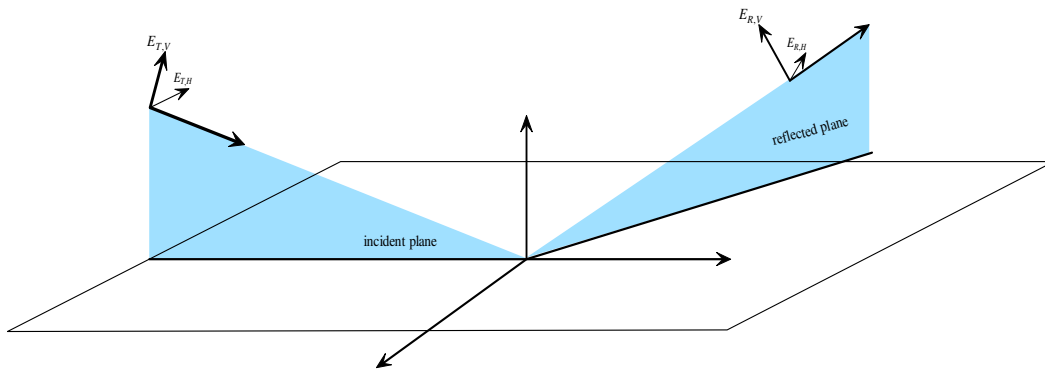


Figure 1: Coordinates for incident and reflected polarizations of the electric field.

In-plane scattering allows the use of a one-dimensional “slice” of a sea surface for this Phase 1 effort. Phase 2 will tackle the full two-dimensional sea surface. For one-dimensional scattering, assume the following:

RF-1 Homogenous atmosphere.

RF-2 Distant transmitter.

RF-3 Surface-level receiver.

RF-4 No surface-level diffraction or aerosol effects.

RF-5 The sea surface is constant in each plane orthogonal to the signal direction.

A homogenous atmosphere has a constant index of refraction or, equivalently, a constant speed of propagation. In a homogenous atmosphere, rays travel in straight lines. The distant transmitter justifies the plane-wave approximation of the transmitter’s EM field. The surface-level antenna justifies a flat-earth approximation for ray tracing. The absence of diffraction over the waves allows ray tracing after reflection.

Finally, RF-5 forces in-plane scattering. There is no lateral scattering. Consequently, the scattering takes place in a two-dimensional plane reflecting off a one-dimensional surface. The simplest scattering is flat-surface scattering.

3 Flat-Surface Scattering

Figure 2 illustrates the ray bundles for flat-surface scattering. A transmitter is broadcasting a narrow-band signal $s_T(t)$ at wavelength λ_T and polarization p_T .² The distant transmitter's electric field is approximated by plane waves traveling in the direction shown by the rays with elevation angle θ_T . The receiver has an antenna located at height h_R .

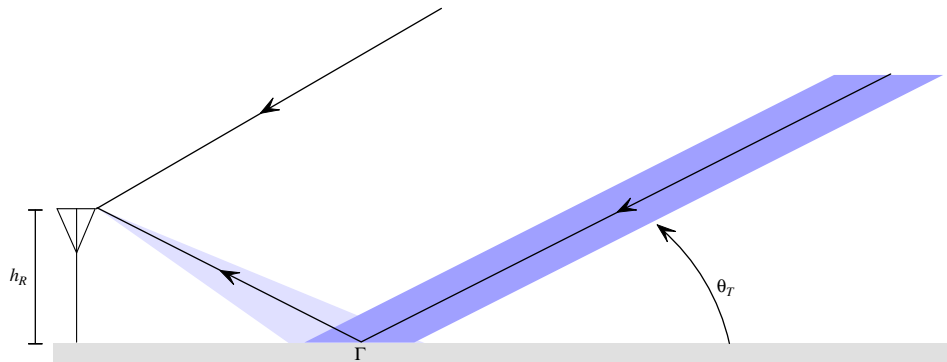


Figure 2: Direct path, specular reflection, and diffuse scatter.

The direct path follows free-space propagation to the antenna to arrive delayed in time by τ_1 and scaled by the *complex gain* g_1 of the antenna in the direct path:

$$s_R(t) = g_1 s_T(\tau - \tau_1).$$

Because the signal $s_T(t)$ is narrow band, the transfer function of the antenna only multiplies the direct-path signal with a complex gain.³

The plane wave also illuminates the entire surface. Each piece of the surface projects some energy into the antenna. A flat surface reflects most of the energy in the *specular direction* defined by Bello [10]:

The direction that the reflected plane wave would take if the incident plane were reflected from a mirror located at the mean surface height.

² p_T is a complex number characterizing the polarization and is the stereographic projection of the Poincaré sphere [30].

³There is no loss of generality for ignoring the free-space loss and scaling only by the antenna.

The specular reflection is modeled as a ray that travels to the antenna. However, the surface's *reflection coefficient* Γ reduces power, changes phase, and modifies the polarization. For a flat, mirror-like surface, the received signal is the sum of the direct path and specular reflection:

$$s_R(t) = g_1 s_T(\tau - \tau_1) + g_2 \Gamma s_T(\tau - \tau_2),$$

where g_2 is the complex gain of the antenna in the specular direction. Consequently, the input delay-spread function $h(t, \tau)$ has the form determined by Matthews [28, Eq. 2.25], and Parsons [36, Eq. 2.19]:

$$h(t, \tau) = \underbrace{g_1 \delta(\tau - \tau_1)}_{\text{direct path}} + \underbrace{g_2 \Gamma \delta(\tau - \tau_2)}_{\text{specular reflection}}. \quad (2)$$

In this flat-surface model, the signal does not change if the surface is moved horizontally. This model can be extended to *slightly rough surfaces* by incorporating *diffuse scatter*. For example, Figure 3 shows a rough surface breaking the specular reflection into non-specular directions or into *diffuse scatter*.⁴ The *Fraunhofer criterion* or *Rayleigh criterion* quantifies the surface roughness in terms of the standard deviation σ_ζ of the sea surface.

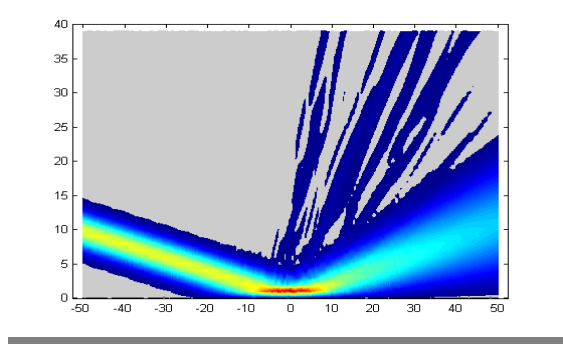


Figure 3: Specular reflection and diffuse scatter off a slightly rough surface.

The surface is considered smooth and produces a strong specular reflection provided [15, Eq. 1], [36, Eq. 2.29]:

$$\sigma_\zeta < \frac{1}{32} \times \frac{\lambda_T}{\sin(\theta_T)} \iff \text{The RMS phase difference between two rays reflected at two different heights on the surface must be smaller than } \pi/8 \text{ in the far field to coherently combine.}$$

⁴John Rockway, Akira Ishimaru, Yasuo Kuga, Seung-Woo Lee [2005] *Statistical Green's Functions for Applications to Rough Surface and Random Media Scattering, Object Interaction and Detection*, University of Washington Electromagnetics and Remote Sensing Laboratory, Power Point Presentation.

Figure 4 displays the smooth-surface region (the blue region) as a function of angle and surface deviation. Because the sea surfaces in this simulation typically have $\sigma_\zeta < 0.5$ meters, the figure shows that the flat-surface model starts to break down when the transmitter's elevation angle exceeds 5 degrees. Moreover, the Rayleigh criterion does not account for the blocking of the rays that occurs at the low grazing angles.

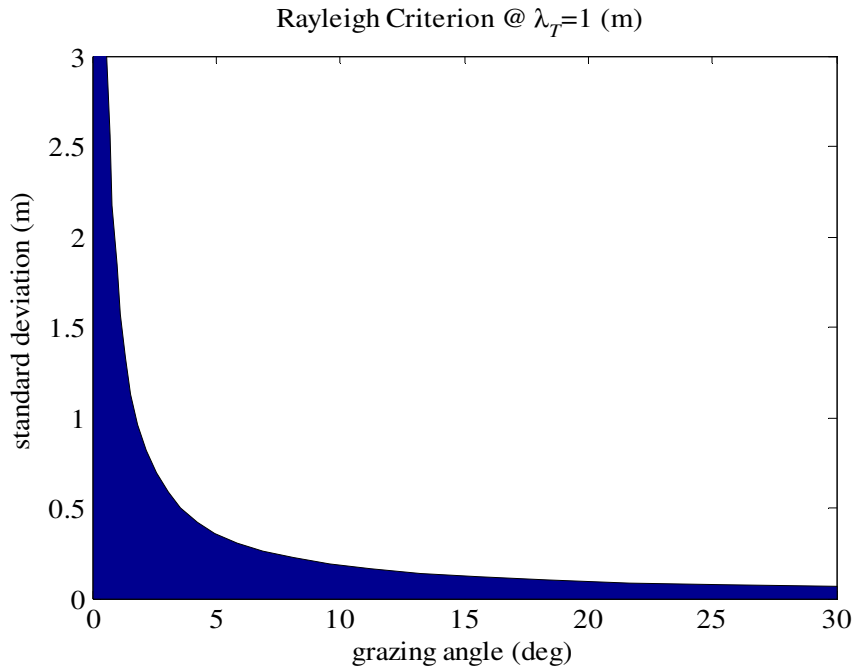


Figure 4: Rayleigh criterion (blue) at 1-meter wavelength in the θ_T - σ_ζ plane.

A typical model uses a Gaussian random process $\{g(t)\}$ to approximate diffuse scattering [26], [11], [29]:

$$h(t, \tau) = \underbrace{g_1 \delta(\tau - \tau_1)}_{\text{direct path}} + \underbrace{g_2 \Gamma \delta(\tau - \tau_2)}_{\text{specular reflection}} + \underbrace{g(t) \delta(\tau - \tau_3)}_{\text{diffuse scatter}}. \quad (3)$$

The following sections unpack the time delays, reflection angles, antenna gains, and reflection coefficients for this model. The final section specializes this model to specular scattering into a surface-level antenna.

3.1 Time Delays

For the receiver simulation, there is no loss of generality to work with the relative delays by taking $\tau_1 = 0$. In Figure 5, provided the transmitter's elevation angle

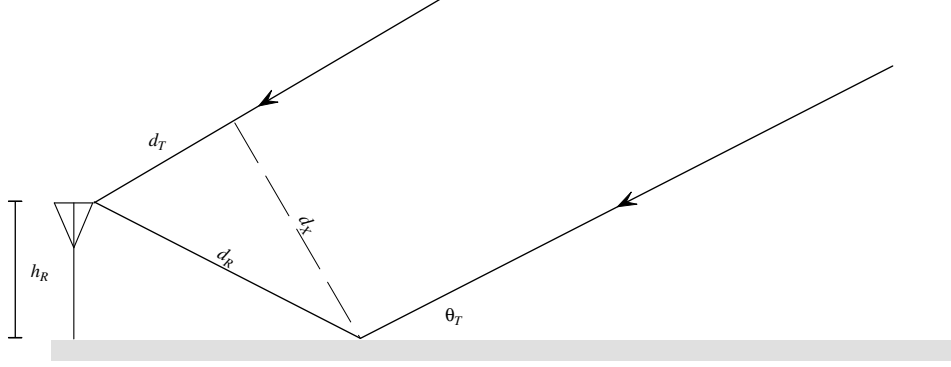


Figure 5: Time-Delay geometry for elevation angle $\theta_T \leq 45^\circ$.

$\theta_T \leq 45^\circ$, the delay between the direct path and reflected path is

$$\tau_2 = c^{-1}(d_R - d_T) = 2h_R \sin(\theta_T). \quad (4)$$

When the transmitter's elevation angle θ_T exceeds 45 degrees, the geometry is different, but the delay formula is the same. Recalling that $1 \text{ ns} \approx 1 \text{ foot}$, a 3-meter mast exhibits a maximum delay of approximately 18 ns. Figure 6 shows that the small elevation angles have time delays of approximately 1 nanosecond. A receiver with a bandwidth of 100 kHz cannot resolve these delays for signal enhancement. Although the simulations show that longer delays are possible because of distant reflections off the sea surface, even these longer delays do not exceed a few hundred nanoseconds. The narrow-band receiver still cannot resolve these longer paths. Consequently, the zero-delay of Equation 1 still applies.

3.2 Antenna Gains

If the polarization p_T of the transmitted signal matches the polarization p_R of the receiving antenna, the magnitude of the gains on the direct and reflected paths are

$$|g_1| = G_R(\theta_T)^{1/2}, \quad |g_2| = G_R(-\theta_T)^{1/2},$$

where the receiving antenna's gain $G_R(\theta)$ is a function of elevation angle.

To handle the polarization mismatch between the receiving antenna with polarization p_R and a single transmitted wave with polarization p_T , the *polarization efficiency*

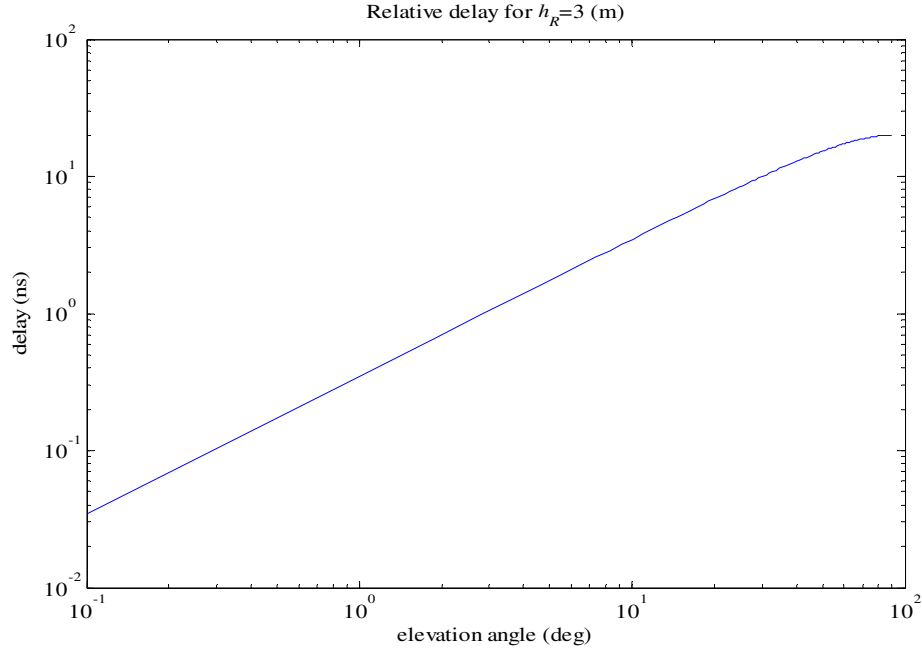


Figure 6: Time delays for a short mast and flat reflections.

η modifies the gains as determined by Beckmann [6, page 186]:

$$|g_1| = G_R(\theta_T)^{1/2} \times \eta(p_R(\theta_T), p_T)^{1/2}.$$

Here, $\eta(p_R, p_T)$ is the ratio of the power delivered to the antenna from a wave with polarization p_T to the maximum power delivered to the antenna from a wave with polarization p_R and computed as

$$\eta(p_R, p_T) = \frac{|1 + p_R \overline{p_T}|^2}{(1 + |p_R|^2)(1 + |p_T|^2)}.$$

When multiple waves of various polarizations arrive at the antenna, the antenna functions as an electrical transducer mapping the received waves into voltages at the antenna's terminal. The antenna's *complex effective length* was conceived by Sinclair [40] to model this transducer and effectively complexifies the gains. When only the antenna gain is available, this limitation is acknowledged by using the gain $G_R(\theta)$.

3.3 Reflected Path

The ray that coherently reflects off the sea surface loses power and is depolarized. The power loss and depolarization are encoded in the factorization of the *reflection*

coefficient [10], [33, pages 19–22], [25, pages 95–125]:

$$\Gamma = D\Gamma_0\mathcal{R}, \quad (5)$$

where D denotes the divergence, \mathcal{R} denotes the roughness coefficient, and Γ_0 is the plane surface reflection coefficient.

Divergence: The divergence $0 \leq D \leq 1$ [25, page 98] “is equivalent to a purely geometric factor that describes additional spreading of a beam of rays due to reflection from a spherical surface.”

Roughness: As the sea surface changes from a glassy “mirror-like” surface to a wind-ruffled chop, the specular reflection of any ray decreases. This decrease is modeled by the *surface roughness coefficient* \mathcal{R} derived from experimental observations [4], [5], [20], [25, pages 122–125], [13, Eq. 2.62]:

$$\mathcal{R}(\theta_g) = e^{-\mathbf{g}^2/2} I_0(\mathbf{g}^2/2); \quad \mathbf{g} = 4\pi \sin(\theta_g) \frac{\sigma_\zeta}{\lambda_T}, \quad (6)$$

where \mathbf{g} is the “electrical roughness parameter” [10] or “apparent ocean roughness” [4], the grazing angle θ_g is the angle between the ray and the local tangent plane ($\theta_g = \theta_T$ in the plot), σ_ζ denotes the standard deviation of the height fluctuation of the surface [33, page 59], [25, pages 50–54], and λ_T is the wavelength of the transmitted waveform.

Plane Surface Reflection Coefficients: The reflection coefficient Γ_0 for a plane surface depends on the complex *permittivity* ϵ of the terrain and the polarization. For sea-water at 20 degrees Centigrade and frequencies less than 1 GHz, the complex permittivity is [13, Eq. 3.1]:

$$\epsilon = \epsilon' - j60\sigma\lambda_T = 70 - j300\lambda_T.$$

The reflection coefficient for vertical polarization [25, page 99], [13, page 53]:

$$\Gamma_{0,V} = \frac{\epsilon \sin(\theta_g) - \sqrt{\epsilon - \cos(\theta_g)^2}}{\epsilon \sin(\theta_g) + \sqrt{\epsilon - \cos(\theta_g)^2}}, \quad (7)$$

where the grazing angle θ_g is the angle between the ray and the local tangent plane ($\theta_g = \theta_T$ in the plot). For horizontal polarization, the reflection coefficient is [21, page 396],

$$\Gamma_{0,H} = \frac{\sin(\theta_g) - \sqrt{\epsilon - \cos(\theta_g)^2}}{\sin(\theta_g) + \sqrt{\epsilon - \cos(\theta_g)^2}}. \quad (8)$$

Figures 7 and 8 plot the reflection coefficient for seawater as a function of the grazing angle. The scales are different for clarity and show that the horizontal reflection coefficient for seawater is essentially -1 .

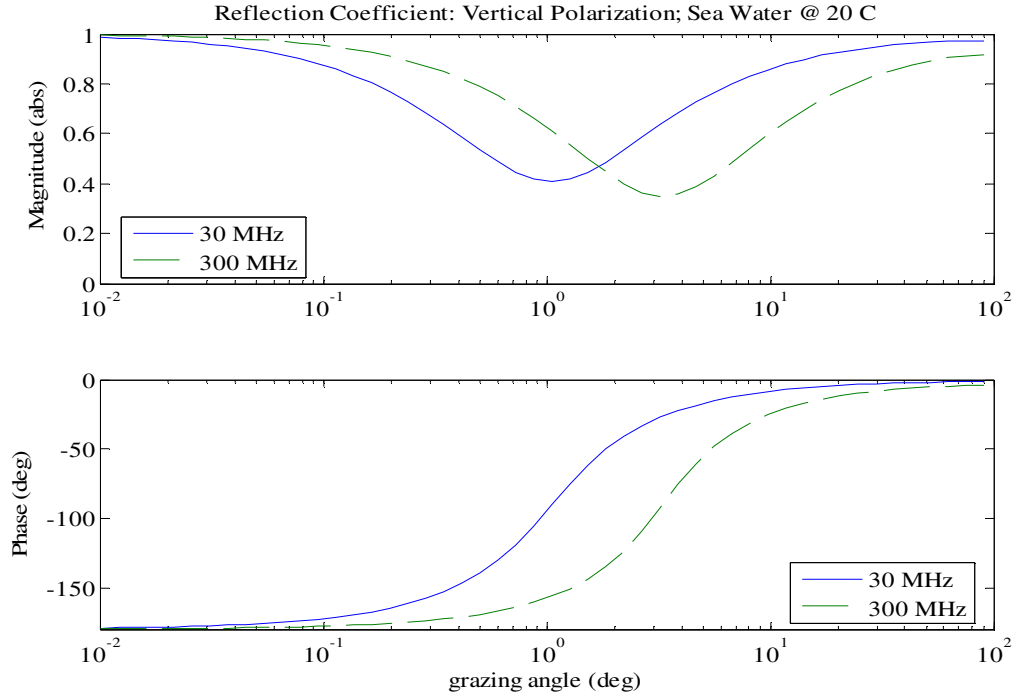


Figure 7: Vertical reflection coefficient for seawater.

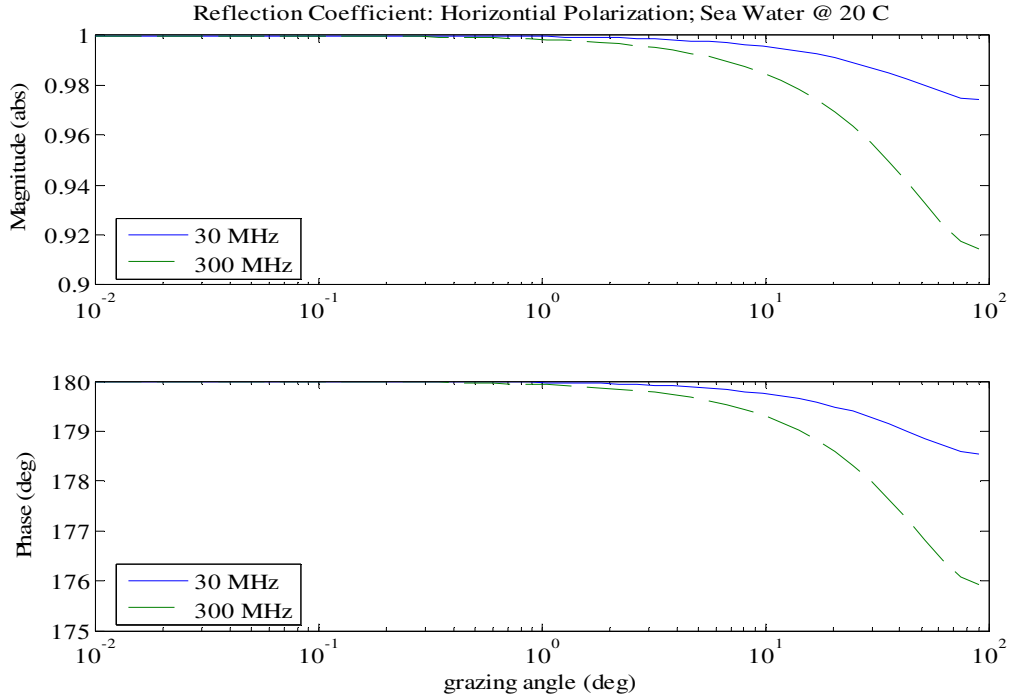


Figure 8: Horizontal reflection coefficient for seawater.

The problem is to use these vertical and horizontal reflection coefficients to compute the reflection coefficient for any elliptical polarization. Of the several approaches, a beautiful “change-of-basis” is found in Stutzmann [42]. The real-valued instantaneous electric field $\mathbf{E}(t)$ can be written as

$$\mathbf{E}(t) = \cos(\omega t)E_H\mathbf{u}_H + \cos(\omega t + \delta)E_V\mathbf{u}_V, \quad (9)$$

where \mathbf{u}_V and \mathbf{u}_H are the orthogonal unit vectors in the vertical and horizontal directions. A *left-handed* circularly polarized (LCP) wave has $E_V = E_H$ and $\delta = +90^\circ$ [42, Eq. 2.30] so that

$$\mathbf{E}_L(t) = \frac{E_L}{\sqrt{2}} \{\cos(\omega t)\mathbf{u}_H - \sin(\omega t)\mathbf{u}_V\}.$$

A *right-handed* circularly polarized (RCP) wave has $E_V = E_H$ and $\delta = -90^\circ$ [42, Eq. 2.31] so that

$$\mathbf{E}_R(t) = \frac{E_R}{\sqrt{2}} \{\cos(\omega t + \delta')\mathbf{u}_H + \sin(\omega t + \delta')\mathbf{u}_V\},$$

where δ' models a phase difference between $E_L(t)$ and $E_R(t)$. Any electric field $E(t)$ can be represented in the $\mathbf{E}_H(t)$ and $\mathbf{E}_V(t)$ basis. Likewise, any electric field can be represented in the $\mathbf{E}_L(t)$ and $\mathbf{E}_R(t)$ basis. The *complex* electric field provides a convenient change-of-basis from linear to circular polarization. The instantaneous electric field $\mathbf{E}(t)$ links to the *phasor* electric field⁵ intensity \mathbf{E} as provided by Stutzmann [42, Eq. 3.11]:

$$\mathbf{E}(t) = \Re[\mathbf{E}e^{j\omega t}].$$

The phasor electric field may be decomposed as provided by Stutzmann [42, Eq. 3.12]

$$\mathbf{E} = E_H\mathbf{u}_H + E_V\mathbf{u}_V,$$

where E_H and E_V are now their *complexified* versions in Equation 9. The complexified components of circular polarization relate to the complexified components of the linear polarizations as provided by Stutzmann [42, Eq. 8.31]:

$$\begin{aligned} \begin{bmatrix} E_V \\ E_H \end{bmatrix} &= \frac{1}{\sqrt{2}} \begin{bmatrix} 1 & 1 \\ j & -j \end{bmatrix} \begin{bmatrix} E_L \\ E_R \end{bmatrix}, \\ \begin{bmatrix} E_L \\ E_R \end{bmatrix} &= \frac{1}{\sqrt{2}} \begin{bmatrix} 1 & -j \\ 1 & j \end{bmatrix} \begin{bmatrix} E_V \\ E_H \end{bmatrix}. \end{aligned}$$

Assumption RF-5 lets us claim in-plane scattering or that *the scattering is such that purely horizontal or purely vertical polarization is not depolarized*. That is, the incident electric field \mathbf{E}_i is mapped to the reflected electric field \mathbf{E}_r as provided by Stutzmann [42, Eq. 8.29]:

$$\begin{bmatrix} E_{r,V} \\ E_{r,H} \end{bmatrix} = \begin{bmatrix} \Gamma_{0,V} & 0 \\ 0 & \Gamma_{0,H} \end{bmatrix} \begin{bmatrix} E_{i,V} \\ E_{i,H} \end{bmatrix}.$$

⁵The Fourier transform of $\mathbf{E}(t)$.

The change-of-basis converts this scattering of the linear polarizations to circular scattering provided by Stutzmann [42, Eq. 8.34]:

$$\begin{bmatrix} E_{r,L} \\ E_{r,R} \end{bmatrix} = \begin{bmatrix} \Gamma_{0,C} & \Gamma_{0,X} \\ \Gamma_{0,X} & \Gamma_{0,C} \end{bmatrix} \begin{bmatrix} E_{i,L} \\ E_{i,R} \end{bmatrix},$$

where the circular and cross-circular reflection coefficients are [42, Eq. 8.35]

$$\Gamma_{0,C} = \frac{1}{2} \{ \Gamma_{0,V} - \Gamma_{0,H} \},$$

$$\Gamma_{0,X} = \frac{1}{2} \{ \Gamma_{0,V} + \Gamma_{0,H} \},$$

and plotted in Figures 9 and 10, respectively.

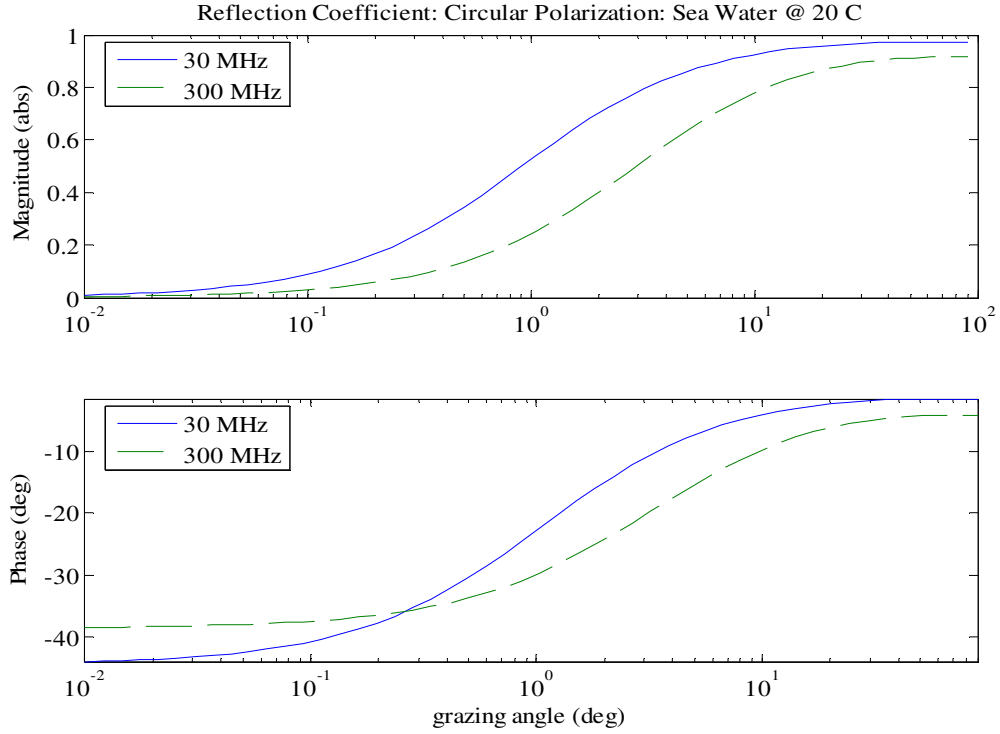


Figure 9: Circular reflection coefficient for seawater.

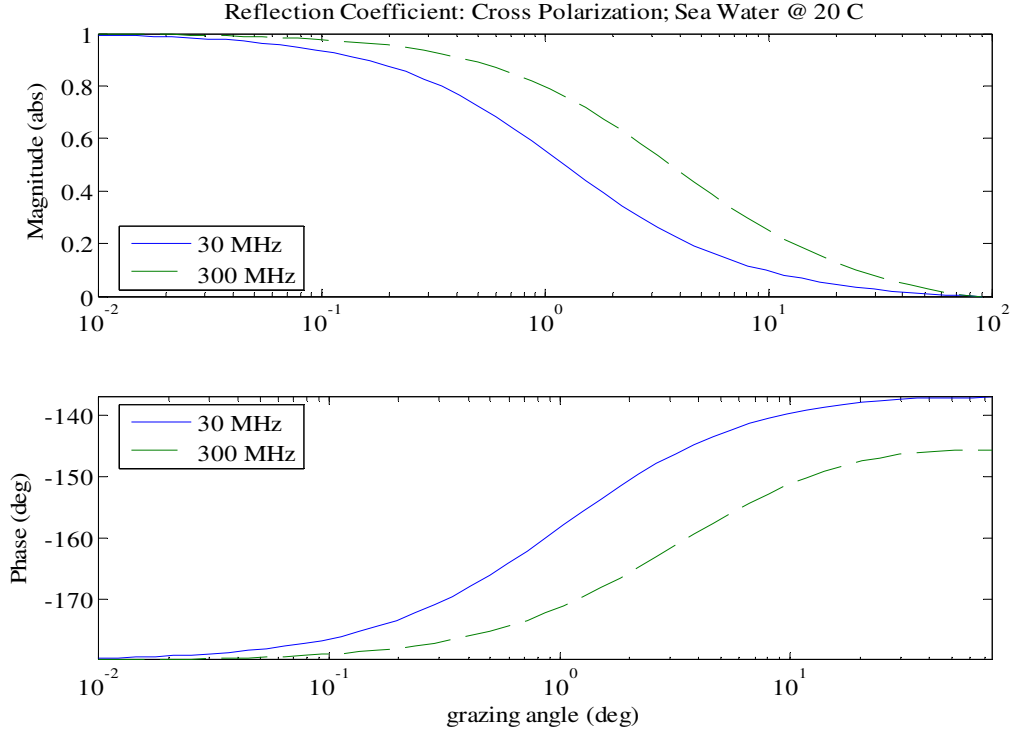


Figure 10: Cross-circular reflection coefficient for seawater.

3.4 Diffuse Scatter

As the sea surface changes from a glassy surface to a wind-ruffled chop, the specular reflection decreases and the diffuse scatter increases. The diffuse scatter is typically modeled by a zero-mean, narrow-band, complex-valued Gaussian random process $\{g(t)\}$. Consequently, only the spectral shape and variance σ_g^2 need be specified. Beard [5], [4] obtains a heuristic model for σ_g^2 using the surface roughness, whereas Ryan⁶ argues from conservation laws that

$$\sigma_g^2 = G_f |\Gamma_0|^2 (1 - \mathcal{R}^2). \quad (10)$$

Here G_f denotes a “forward-scatter” gain. Regardless of the approach, σ_g^2 is a function of the surface roughness \mathcal{R} —assuming the model implicit in Equation 3. The assumption for this model are discussed in the next section.

⁶Personal communication from Frank Ryan, SSC San Diego.

3.5 Specular Scattering at a Surface-Level Antenna

A qualitative model of specular scattering into a surface-level antenna is constructed from the preceding computations. This model captures those effects of specular scattering that generalize to tangent-plane scattering off a sea surface.

Placing the antenna near the a relatively smooth surface allows us to ignore the time delays, the divergence, the surface roughness coefficient, and the diffuse scatter. However, placing the antenna within a wavelength of the surface distorts the antenna pattern.

Regarding the time delays, Section 3.1 shows that the low antenna induced time delays by a few nanoseconds. The sea-surface simulations show that even the distant reflections delay the signal by only a few hundred nanoseconds. If the receiver has a bandwidth of only 100 kHz, these nanosecond delays cannot be resolved. Consequently, the time delays are ignored.

Regarding the divergence D , the sea-surface simulations show reflections are limited to a few kilometers. Consequently, the flat earth is an excellent approximation and $D = 1$ [21, page 113].

Figure 11 plots the surface roughness coefficient \mathcal{R} of Equation 6 as a function of the standard deviation σ_ζ of the surface. The wavelength is $\lambda_T = 1$ meter. Each curve is plotted for a fixed elevation angle: $\theta_T = 5^\circ, 10^\circ, 30^\circ$. Because the sea surface simulations have $\sigma_\zeta \leq 0.5$ meters, the surface roughness coefficient \mathcal{R} approximately 1 for elevation angles $\theta_T < 10^\circ$. Consequently, its effect on surface reflection coefficient Γ of Equation 5 is ignored.

For the larger angles and the rougher seas, \mathcal{R} is fit to widely varying experimental data. From Long [25, pages 122–124]:

- Reflection data are often given with little precision.
- Evaluation of Γ is only an estimate.
- Values for σ_ζ are at best guesses.

Moreover, the form of \mathcal{R} neglects edge and shadowing effects. Consequently, we take $\mathcal{R} = 1$ up to 30° , noting that our sea-surface scattering will include shadowing and the roughness caused by multiple reflectors within the antenna’s footprint.

The following observations justify omitting the diffuse scattering term of Equation 3. First, the diffuse scatter $\{g(t)\}$ approximates the effect multiple reflectors within the antenna’s footprint. Because the model we develop includes these multiple reflectors, some diffuse scattering is actually included. Second, Equation 10 shows the diffuse scatter is small when $\mathcal{R} \approx 1$. The surface roughness \mathcal{R} depends on the

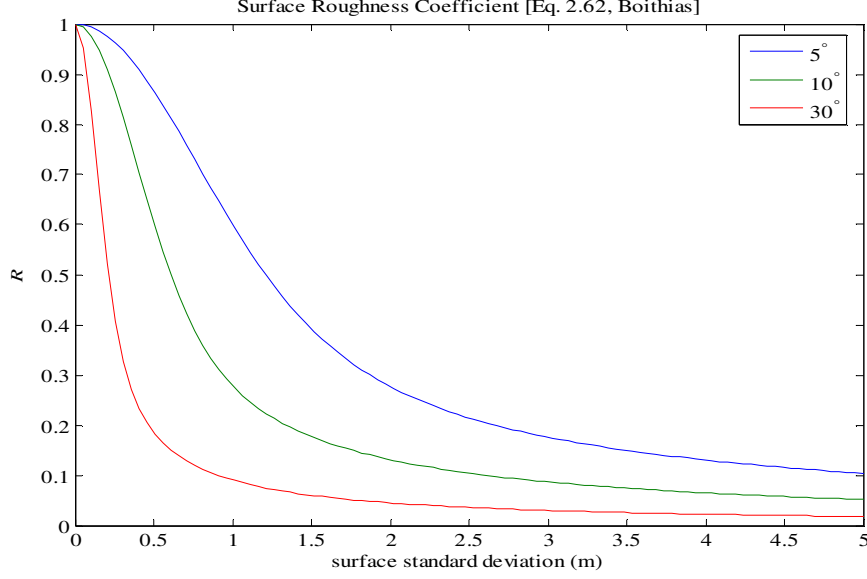


Figure 11: Surface roughness coefficient.

variance σ_ζ^2 of the sea surface $\zeta(\mathbf{r})$. This variance depends on the wind speed U from Equations 13 and 14. Figure 12 plots the diffuse scatter power σ_g^2 at 300 MHz as a function of wind speed U for grazing angles $\theta_T = 5^\circ, 10^\circ$, and 30° . The forward scatter gain is $G_f = 1/2$. The plot shows that omitting σ_g^2 induces errors 10% or less, provided that the wind speed is less than 10 m/s or that the grazing angle is less than 10 degrees.

With negligible time delays, surface roughness coefficient $\mathcal{R} = 1$, and diffuse scatter ignored, the input delay-spread function for this Flat-Surface Scattering is well-approximated by the direct path and a single reflection:

$$h(t, \tau) = \{G_R(\theta_T)^{1/2} + G_R(-\theta_T)^{1/2}\Gamma_{0,C}(\theta_T)\} \times \delta(\tau). \quad (11)$$

Section 6 applies this model to develop tangent plane scattering used for the multipath simulations.

In summary, this Flat-Surface Scattering Model of Equation 11 omits the following:

- Delays: Nanosecond delays are not resolvable with a kHz bandwidth.
- Diffuse scatter ($\mathcal{R} = 1$): The flat surface is assumed to be smooth.
- Curved Earth ($D = 1$): The surface-level antenna allows us to assume a flat earth [21, page 113].
- Scintillation: No fast fading on the rays.

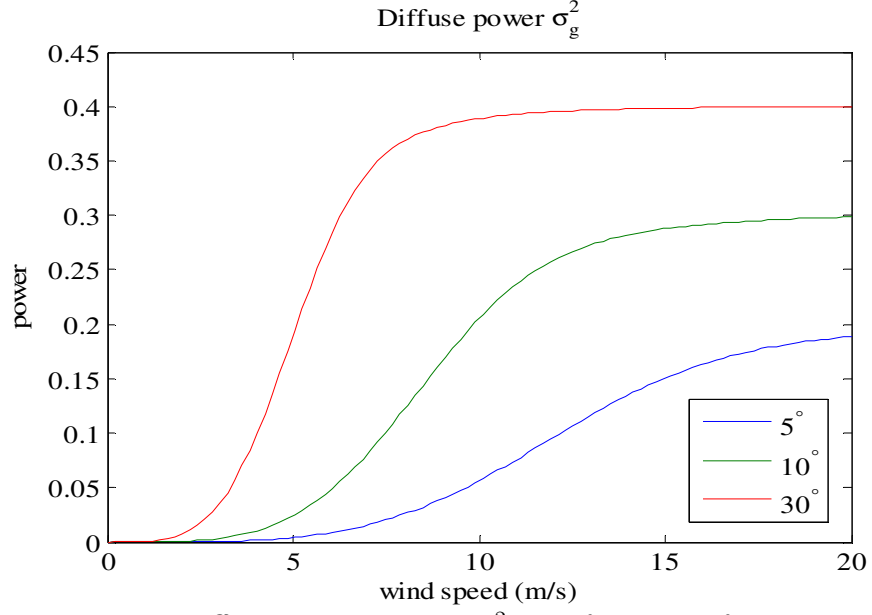


Figure 12: Diffuse scatter power σ_g^2 as a function of wind speed.

- Shadowing and blocking: Not relevant because of flat-surface assumption.
- Loss: Propagation loss on the reflected path is ignored.
- Antenna mismatch: The transmitting and receiving antennas have the same circular polarization.

The next section introduces the antenna patterns $G_R(\theta)$ and extends Equation 11 to account for the antenna mismatch.

4 Antenna Patterns

The simulations use a quadrifilar helix antenna as the receiving antenna. Figure 13 is a picture of a typical quadrifilar helix antenna. Section 4.1 displays a text-book pattern produced by a quadrifilar helix antenna. This pattern has a simple cardioid shape so is an excellent baseline case. Section 4.2 reports on measured patterns for a right circularly polarized (RCP) quadrifilar helix antenna. These patterns are more complex compared to the model quadrifilar helix antenna. The plots also show the antenna's response to both right and left circular polarizations. Section 4.4 makes the final adjustments in the multipath model to include both the RCP and LCP measurements.

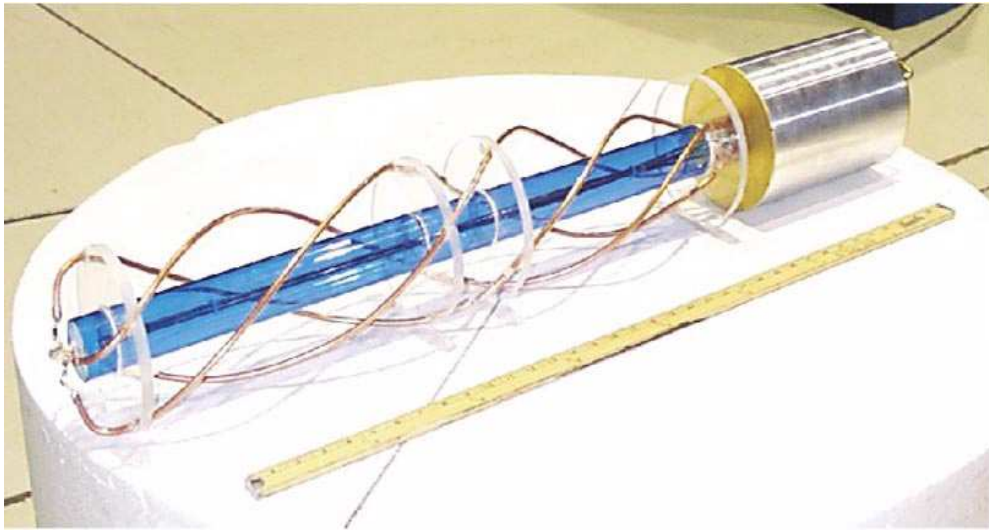


Figure 13: Electronically Reconfigurable SATCOM Antenna (courtesy of Toyon Research Corporation).

4.1 Baseline Quadrifilar Pattern

Kilgus [22], [23] analytically investigated the quadrifilar helix and determined that this antenna exhibits a cardioid pattern. Figure 14 shows such a pattern as measured by Sainati [38]. Because the sea-surface reflections arrive in the lower hemisphere, the lower hemisphere determines the multipath effect. For this reason, the cardioid pattern is the baseline case.

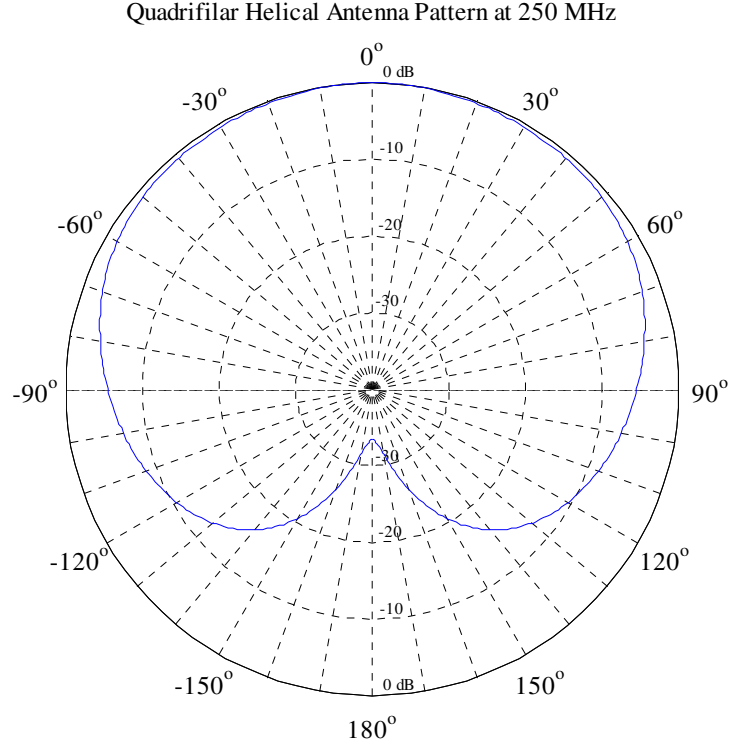


Figure 14: Measured gain as a function of elevation angle for a resonant quadrifilar helix [38].

4.2 Electronically Reconfigurable Antenna (ERA) Patterns

Figures 15 and 16 show the Electronically Reconfigurable Antenna (ERA) patterns. The antenna's RCP response is plotted in blue. Plotted in red is the response to LCP. The low-beam ERA peaks at approximately 10 degrees elevation. The patterns are unexpectedly asymmetric. The asymmetries may be caused by coaxial cable interference, the ground plane being too small, and off-center positioning. In the upper hemisphere, the RCP gain exceeds the LCP gain by 10 dB. In the lower hemisphere, the LCP exceeds the RCP. The reflections from the sea surface arrive in the lower hemisphere and, at low grazing angles, the sea surface changes the polarization from RCP to almost LCP. Consequently, the LCP measurement is needed to register the LCP multipath. Section 4.4 shows how to use both patterns to model the multipath.

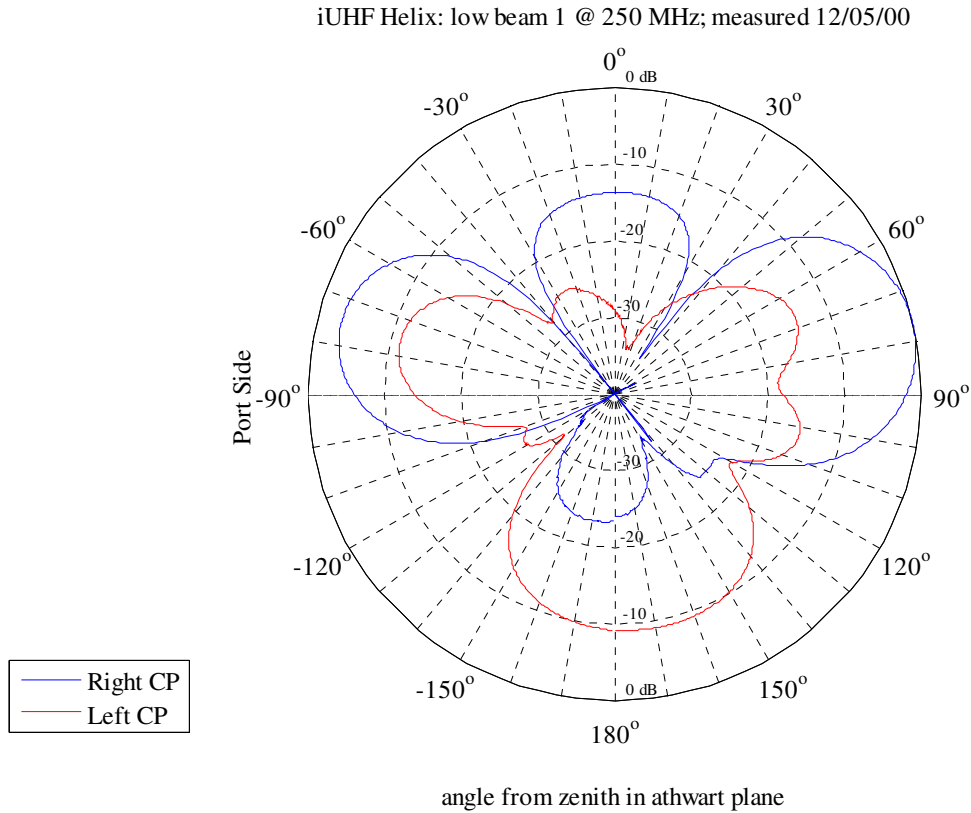


Figure 15: Toyon's low-beam ERA at 250 MHz (courtesy of Toyon Research Corporation).

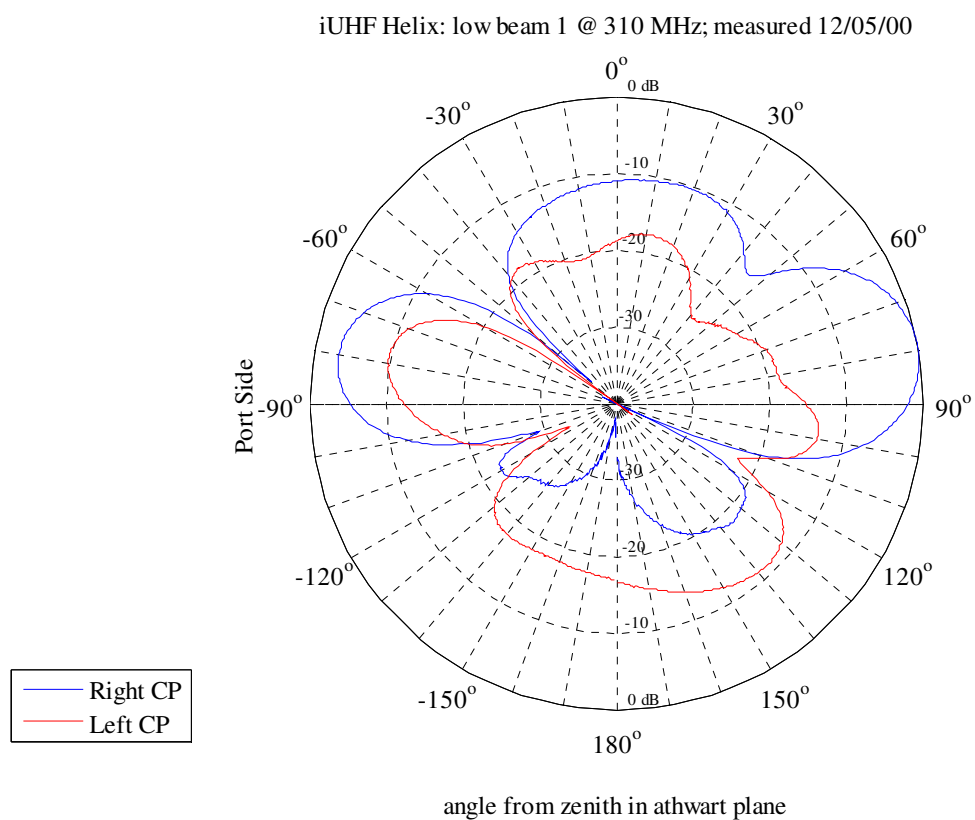


Figure 16: Toyon's low-beam ERA at 310 MHz (courtesy of Toyon Research Corporation).

4.3 OE-538 Patterns

Measurements for the OE-538 antenna were furnished by the Naval Undersea Warfare Center (NUWC). The patterns are plotted in Figures 17, 18, 19, and 20. The patterns are azimuthal (ϕ) slices of the electric field magnitudes $|E_\phi|$ and $|E_\theta|$ plotted against the elevation angle θ . These E-field gains are measured at the base connector of the OE-538 Antenna Assembly. Consequently, the gains are reduced by 1.55 dB because of losses in the internal cabling, diplexers, and switches⁷.

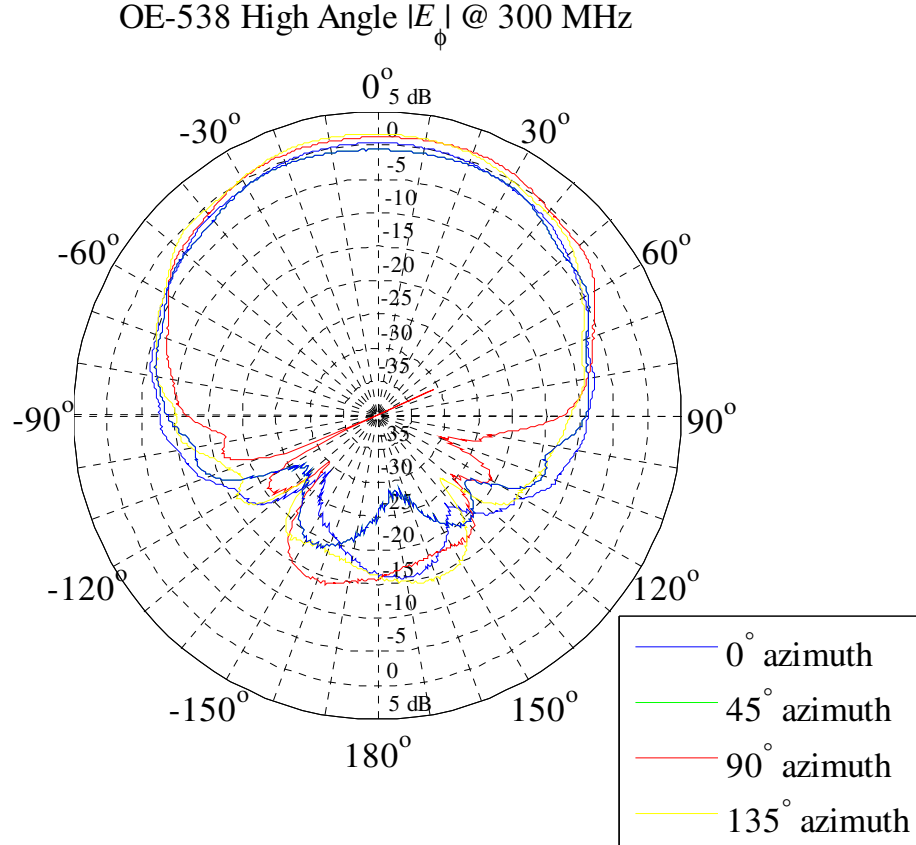


Figure 17: E_ϕ at 300 MHz for High-Angle OE-538 antenna (courtesy of NUWC).

⁷Porco, Pietro G. [2004] OE-538 SATCOM Antennae Gain Footnotes, *NUWC DIVNPT*.

OE-538 High Angle: $|E_\theta|$ @ 300 MHz

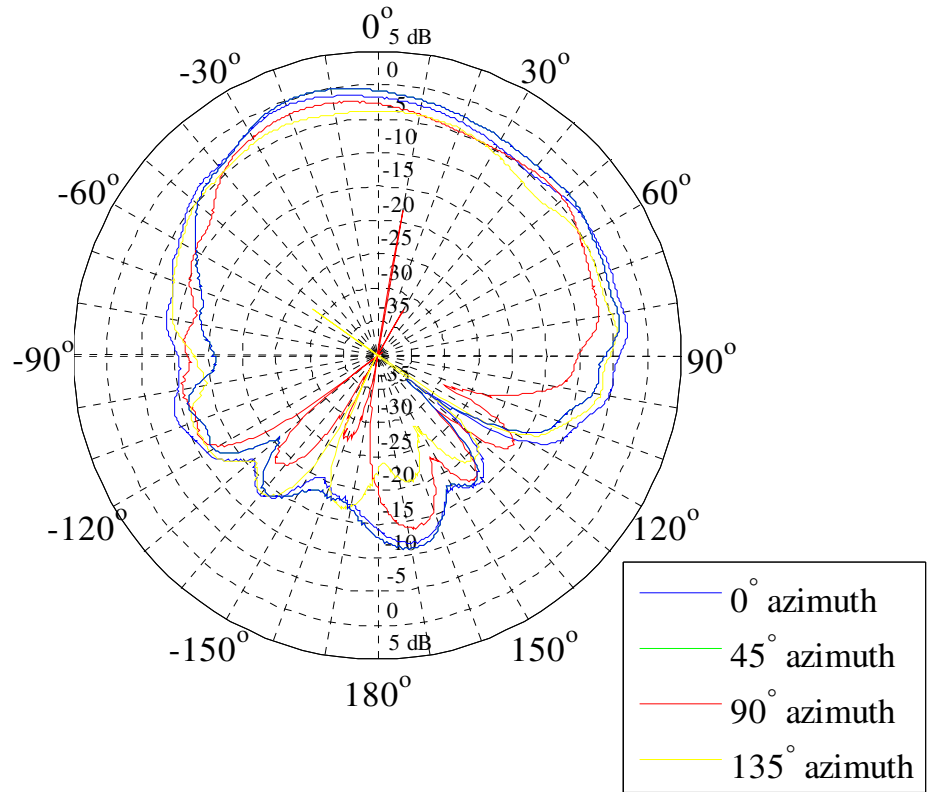


Figure 18: E_θ at 300 MHz for High-Angle OE-538 antenna (courtesy of NUWC).

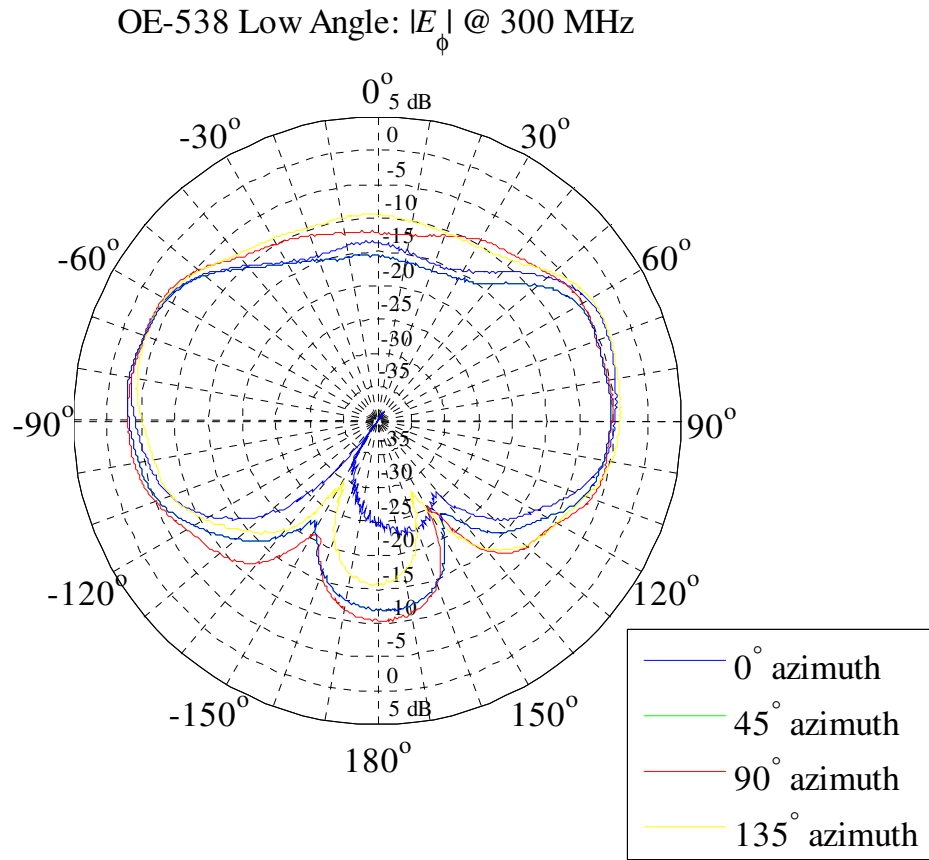


Figure 19: E_ϕ at 300 MHz for Low-Angle OE-538 antenna (courtesy of NUWC).

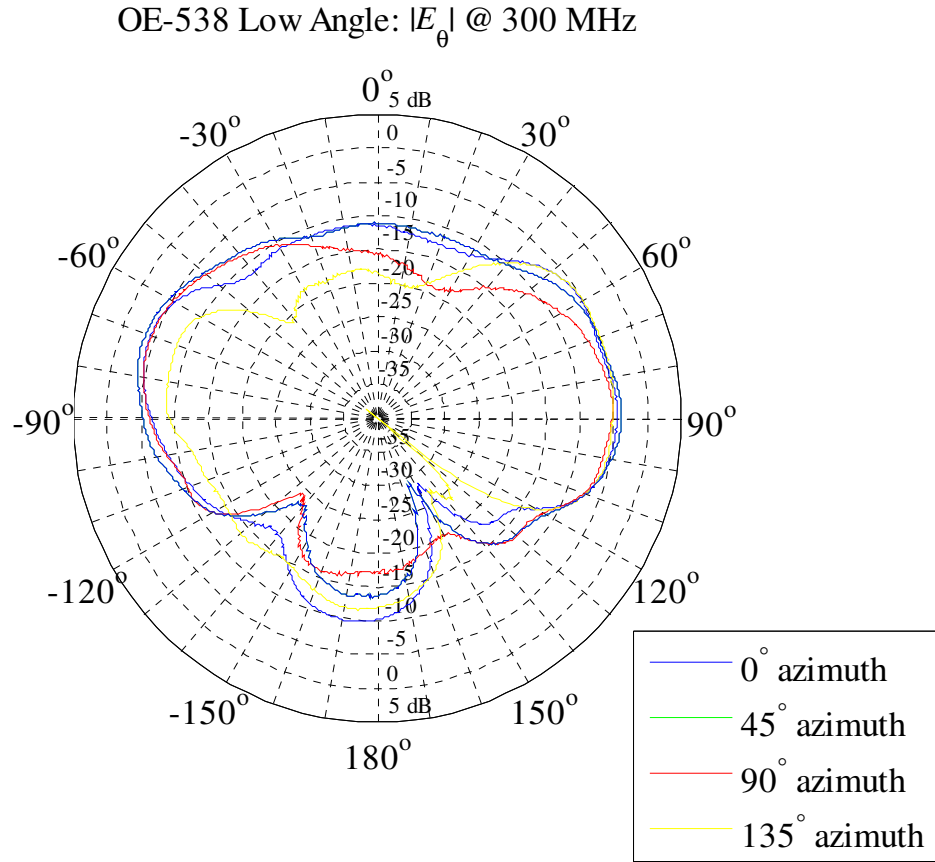


Figure 20: E_θ at 300 MHz for Low-Angle OE-538 antenna (courtesy of NUWC).

The RCP and LCP responses can only be estimated when the phase is missing. The phasor electric field may be decomposed as [42, Eq. 3.12]

$$\mathbf{E} = E_H \mathbf{u}_H + E_V \mathbf{u}_V.$$

We estimate the horizontal and vertical components by assuming RCP or $\delta = -90^\circ$:

$$\begin{aligned} E_H &= |E_\phi| \\ E_V &= |E_\theta| e^{-j\pi/2} \end{aligned}$$

Convert to CP fields as provided by Stutzman [42, Eq. 8.31]:

$$\begin{bmatrix} E_L \\ E_R \end{bmatrix} = \frac{1}{\sqrt{2}} \begin{bmatrix} 1 & -j \\ 1 & j \end{bmatrix} \begin{bmatrix} E_V \\ E_H \end{bmatrix}.$$

Figure 21 plots $|E_\phi|$ and $|E_\theta|$ at $\phi = 0^\circ$ azimuth. Characteristic of a CP antenna, both fields have nearly equal magnitude. Converting these fields to E_R and E_L produces the plots in Figure 22. This plot shows the *estimated* RCP in blue and the *estimated* LCP response in red.

OE-538 Low Angle: E fields @ 300 MHz and 0° azimuth

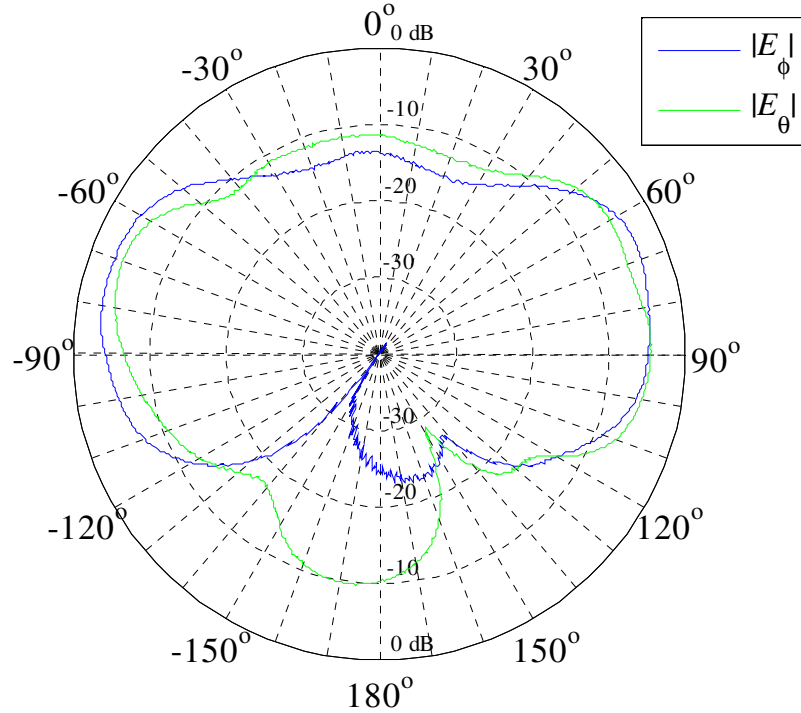


Figure 21: E fields at 300 MHz for Low-Angle OE-538 (courtesy of NUWC).

OE-538 Low Angle: Estimated E_R and E_L @ 300 MHz and 0° azimuth

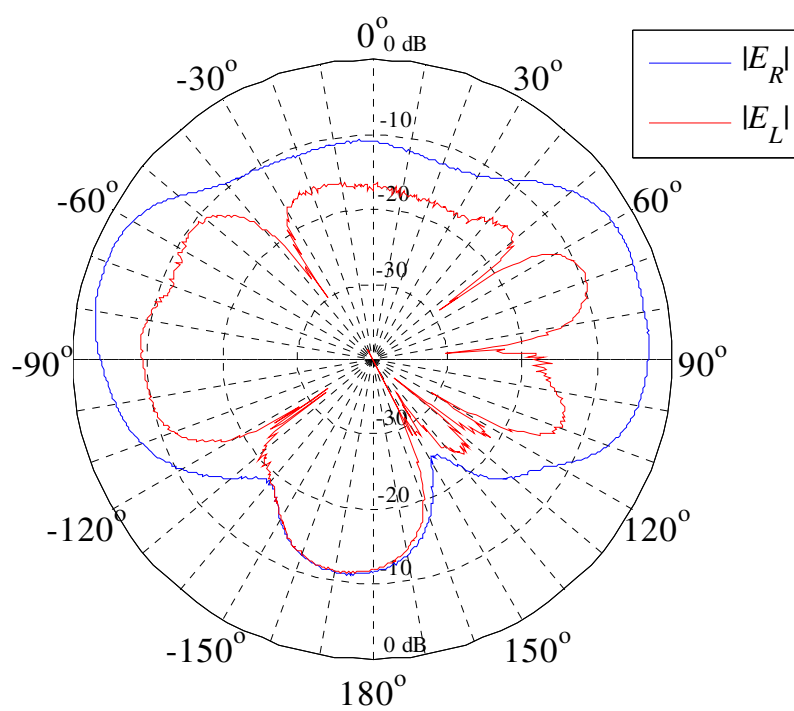


Figure 22: Estimated RCP and LCP gain at 300 MHz for Low-Angle OE-538.

4.4 Antenna Mismatch

When a RCP ray hits a flat sea surface at a low grazing angle, two rays are reflected:

- A weak RCP ray (Figure 9)
- A strong LCP ray (Figure 10)

Arriving at an **ideal** RCP antenna, the LCP rays would **not** generate any voltage in the antenna. However, the antenna plots show that a real-world RCP antenna is not ideal—the real-world RCP antenna factors into an ideal RCP antenna and an ideal LCP antenna. Figure 23 illustrates this antenna and reflection where the received signal is the voltage sum from both ideal antennas: The weak RCP ray exciting the ideal RCP antenna and the stronger LCP ray exciting at the weaker ideal LCP antenna.

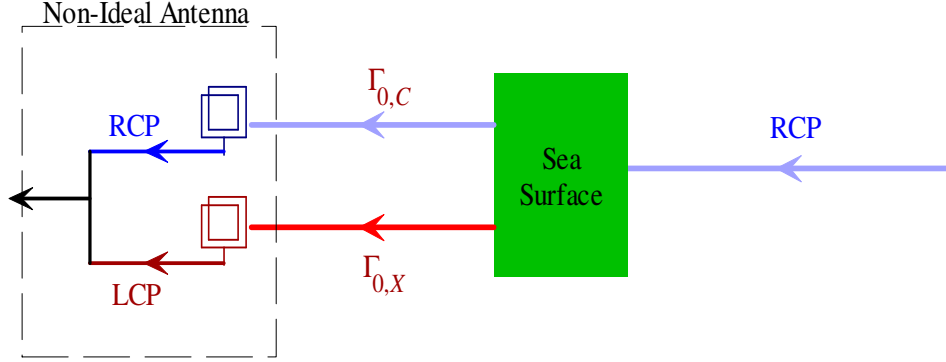


Figure 23: RCP reflecting from sea surface and received by non-ideal RCP antenna.

Figure 23 extends Equation 11 to account for both RCP and LCP reflections from a single ray:

$$\begin{aligned}
 h(t, \tau) = & \underbrace{\{G_{R,RCP}(\theta_T)^{1/2}\}}_{\text{direct path}} + \underbrace{\{G_{R,RCP}(-\theta_T)^{1/2}\Gamma_{0,C}(\theta_T)\}}_{\text{specular RCP reflection}} \\
 & + \underbrace{\{G_{R,LCP}(-\theta_T)^{1/2}\Gamma_{0,X}(\theta_T)\}}_{\text{specular LCP reflection}} \times \delta(\tau). \tag{12}
 \end{aligned}$$

However, a wind-roughened sea surface offers many reflection points. Sea surfaces are introduced in Section 5. Their reflection points are modeled in Section 6.

5 Sea Surfaces

The sea-surface waves are assumed to be generated by a wind blowing across an open fetch of ocean. An excellent description of the wind action on the sea surface and the mechanisms producing the wave types is provided by the Department of Geosciences, University of Houston [14]:

A gentle breeze blowing across the surface causes stresses that are expressed in capillary waves. These are tiny ripples with rounded crests, V-shaped troughs, and wavelengths less than 1.74 cm. They die down immediately if the wind stops blowing, by the restoring force of capillarity (surface tension) . . . These ripples roughen the surface, providing more vertical surface for the wind to push. As the continues to blow, the ripples grow larger and are tranformed into gravity waves . . . The wavelength is generally 15 to 35 times the height. If the wind stops blowing, these waves die down by the restoring force of gravity . . . As winds continue to blow, these gravity waves grow in size. Wave height increases more rapidly than wavelength. The shape changes, with crests becoming more angular and troughs rounded. Eventually the wave reach a maximum size for that particular wind velocity, defined as the point at which the energy supplied by the wind is equaled by the energy lost by breaking waves (white-caps). This is called the fully developed sea.

Figure 24 lays out the sea-surface coordinates and parameters. The wind with mean speed U blows into angle θ over a sea at temperature T_w for a duration measured by the inverse wave age Ω . As indicated in Figure 24, spacial positions are elements of \mathbb{R}^2 denoted as

$$\mathbf{r} = \begin{bmatrix} r_1 \\ r_2 \end{bmatrix}.$$

The height of the sea surface is denoted as $\zeta(\mathbf{r}, t)$ and is a stochastic random field that is a function of position \mathbf{r} and time t . The duration of the signals are so small that the sea surface may be considered stationary or frozen in place. Consequently, the time dependence is omitted. Typically, the sea-surface height $\zeta(\mathbf{r})$ is assumed to be wide-sense stationary with a mean height of zero

$$0 = E[\zeta(\mathbf{r})] \quad [\text{m}],$$

a variance of

$$\sigma_\zeta^2 = E[\zeta(\mathbf{r})^2] \quad [\text{m}^2],$$

and covariance that depends only the spatial difference:

$$R_{\zeta\zeta}(\mathbf{r}) = E[\zeta(\mathbf{r}' + \mathbf{r})\zeta(\mathbf{r}')] \quad [\text{m}^2].$$

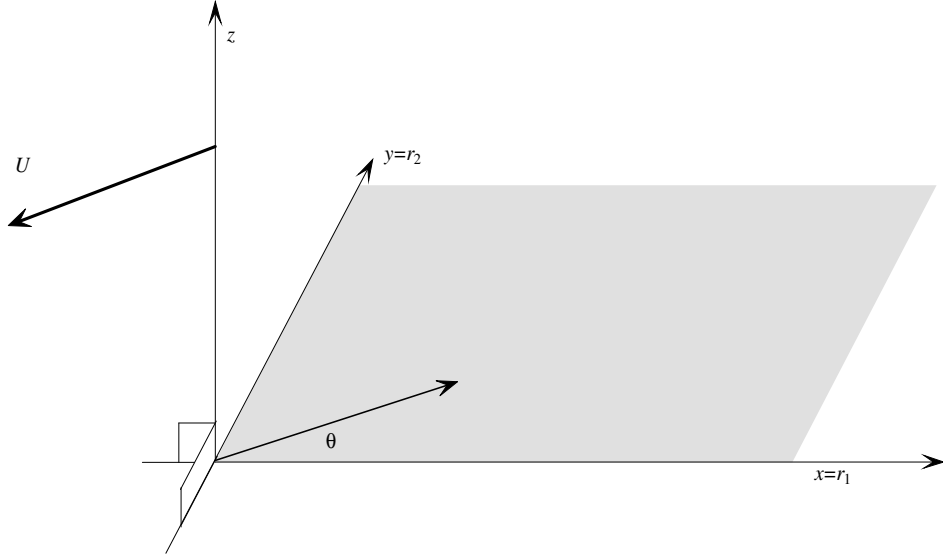


Figure 24: Sea-surface parameters.

The *significant wave height* H_s is the mean of the highest one-third of the waves present in a sea [24, page 302]. Massel derives [27, pages 139–141]

$$H_s \approx 4\sigma_\zeta \quad [\text{m}], \quad (13)$$

assuming the sea is narrow-band, Gaussian, and *fully developed*. A fully developed sea requires both time and area to deliver wind energy to raise the waves [18]: a wind 10 m/s needs to blow with a duration of 18 hours over about 320 km of ocean. The significant wave height H_s links to the sea-surface parameters derived by Massel [27, page 81]:

$$H_s = 0.2092 \frac{U^2}{g} \quad [\text{m}], \quad (14)$$

where g is the gravitational constant. The mean wind speed U denotes the measurement taken at 10 meters height [17, Eq. 17]. Comparing H_s from Equation 14 to the statistical estimate from Equation 13 benchmarks sea-surface simulations.

The sea surfaces are simulated by the *wavenumber spectrum* $\Phi(\mathbf{k})$. The wavenumber spectrum $\Phi(\mathbf{k})$ is the Fourier transform of the covariance of the sea surface:

$$R_{\zeta\zeta}(r_1, r_2) = \int_{-\infty}^{\infty} \int_{-\infty}^{\infty} e^{+j\{k_1 r_1 - k_2 r_2\}} \Phi(k_1, k_2) dk_1 dk_2,$$

where the integral is interpreted in Generalized Random Process Theory [19], [1]. The *wavenumber* vector is denoted

$$\mathbf{k} = \begin{bmatrix} k_1 \\ k_2 \end{bmatrix} \quad [\text{m}^{-1}].$$

Figure 25 shows the wavenumber spectrum down to 50 dB. The spectrum strongly peaked at the *peak wavenumber* k_p .

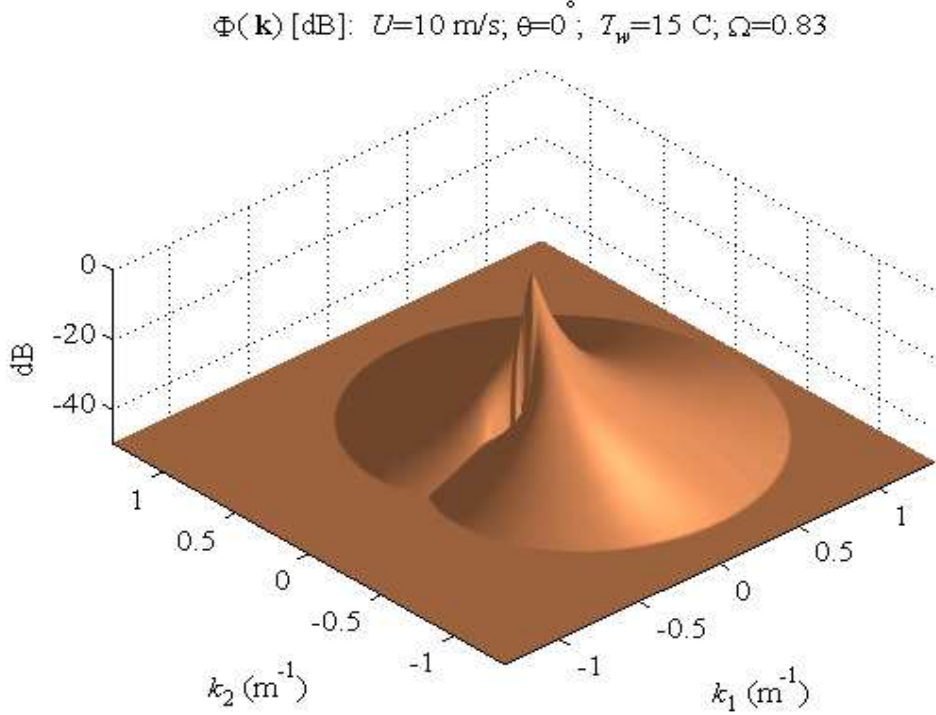


Figure 25: Wavenumber spectrum (3-D display).

Associated with the peak wavenumber k_p is its *peak wave* that travels at speed c_p . The *inverse wave age* Ω measures how closely the wind is aligned with the dominant wave [41]:

$$\Omega = \frac{U}{c_p} \cos(\Delta\theta) \quad \left\{ \begin{array}{ll} > 0.8333 & \text{growing waves or young sea} \\ < 0.8333 & \text{fully developed sea or stable swells} \end{array} \right. ,$$

where $\Delta\theta$ is the angle between the wind and dominant wave direction. Given the inverse wave age, the spectral features can be computed for both a young sea and a fully developed sea. For example, the peak wavenumber and significant wave height for a young sea are modified by Zavoronty and Voronovich [43]:

$$k_p = \Omega^2 \frac{g}{U^2}; \quad H_s = 0.1540 \Omega^{-1.65} \frac{U^2}{g},$$

These models derive from the dependence of wavenumber spectrum $\Phi(\mathbf{k})$ on the inverse waveage. Table 2 lists one choice of variables that model $\Phi(\mathbf{k})$. Variables below the line never change for the simulations. Typically, above the line, only the wind speed varies. Figure 26 presents the spectrum parameterized by the nominal values of Table 2.

Table 2: Gravity and capillary spectral variables for $\Phi(\mathbf{k})$.

Variable	Nominal Values	Description
U	10	mean wind speed at 10 meters (m/s)
θ_{\max}	0	mean wind direction (degrees)
T_w	15	seawater temperature (C)
Ω	0.83	inverse wave age (dimensionless)
f_{slick}	1	slick capillary wave suppression factor
S	35.0	Salinity (psu)
ρ_w	1024.8	sea-water density (kg/m ³)
τ_s	0.074	sea-water surface tension (N/m)
ρ_a	1.225	density of air (kg/m ³)
g	9.7976	gravitational constant (m/s ²)
κ	0.42	Karman constant

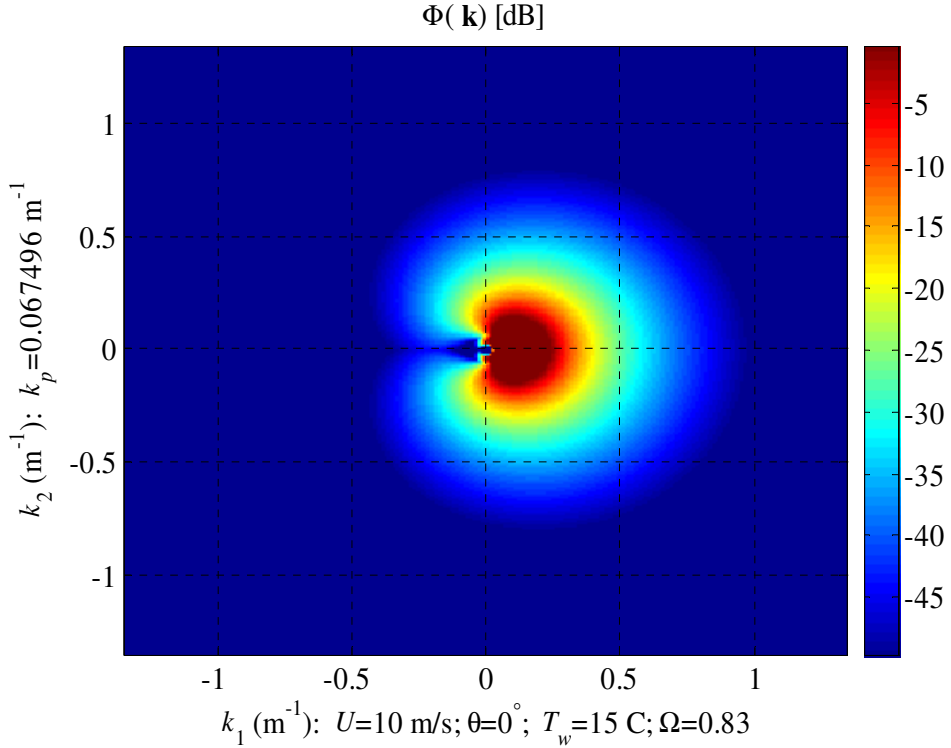


Figure 26: Wavenumber spectrum (top view).

Because the spectral peak is difficult to see in the linear scale, Figure 27 plots “slices” of the spectrum $\Phi(k_1, 0)$ at several wind speeds. Increasing the wind causes the sea surface to resonate more strongly around the peak wavenumber k_p while decreasing the peak wavenumber or increasing the wavelength of the peak wave.

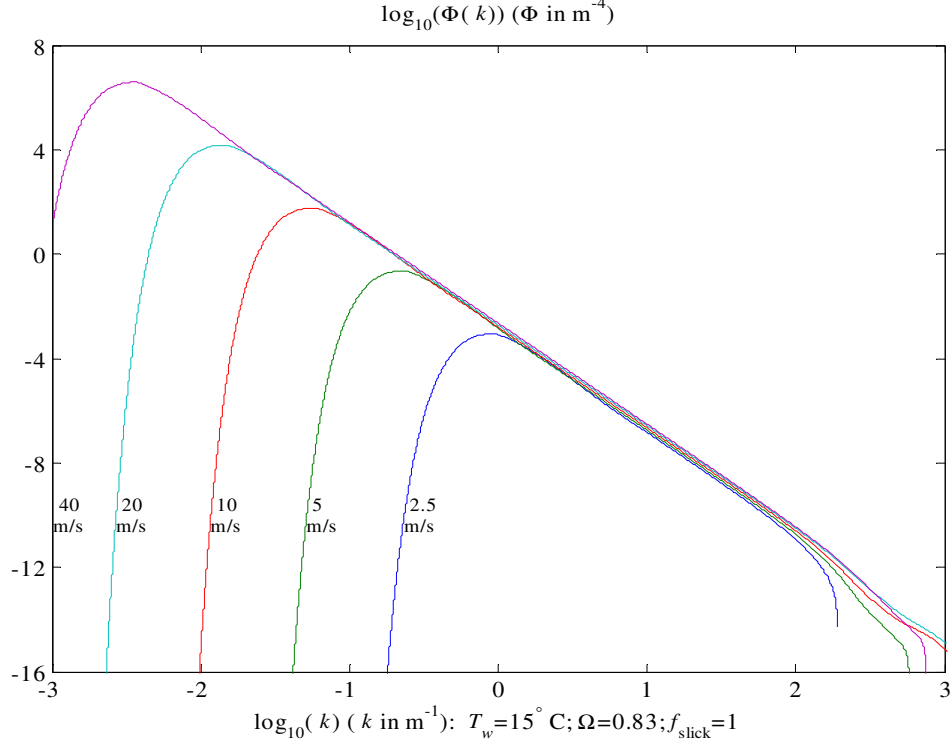


Figure 27: Slices of Donelan-Pierson-Banner-Ryan spectrum; no capillaries.

The sea surface admits a stochastic Fourier representation⁸:

$$\zeta(\mathbf{r}) = \Re \left[\int_{\mathbb{R}^2} e^{j\mathbf{k}^T \mathbf{r}} \Phi(\mathbf{k})^{1/2} G(\mathbf{k}) d\mathbf{k} \right] \quad [\text{m}], \quad (15)$$

where $\{G(\mathbf{k})\}$ is complex-valued, zero-mean Gaussian white noise with covariance [1]:

$$E[G(\mathbf{k})\overline{G(\mathbf{k}')}] = \delta(\mathbf{k} - \mathbf{k}').$$

More formally, $\{G(\mathbf{k})\}$ is a tempered random field that is filtered by $\Phi(\mathbf{k})$ to generate a Gaussian sea surface [19]. Different realizations of $\{G(\mathbf{k})\}$ generate different realizations of the sea surface. The wavenumber spectrum $\Phi(\mathbf{k})$ is based on Donelan

⁸Allen, J. and Frank. J. Ryan [2000] Stochastic Sea-Surfaces for Radar Simulations—Phase 1: Frozen Gaussian Surfaces, *preprint*.

and Pierson's [16] wave spectrum, blended with Banner's [3] observations on the capillary waves and the spreading function, and then unified by Ryan⁹ for both a fully developed sea and a young sea.

Figure 28 shows a digital realization of a Gaussian sea surface plotted over a $40 \times 40 \text{ m}^2$ patch. For clarity, the vertical scale is exaggerated. By a digital realization, we mean Equation 15 is approximated using a digital filter with error control. For example, the wind speed is set as $U = 10 \text{ (m/s)}$. Equation 14 predicts a significant wave height $H_s = 2.1376 \text{ (m)}$. Equation 13 estimates $H_s = 2.1380 \text{ (m)}$. Enforcing this close agreement between the theoretical wave height and estimated wave height is one example of the error control and suggests that the sea-surface simulation has some credible features. The next plot shows this patch in a larger context.

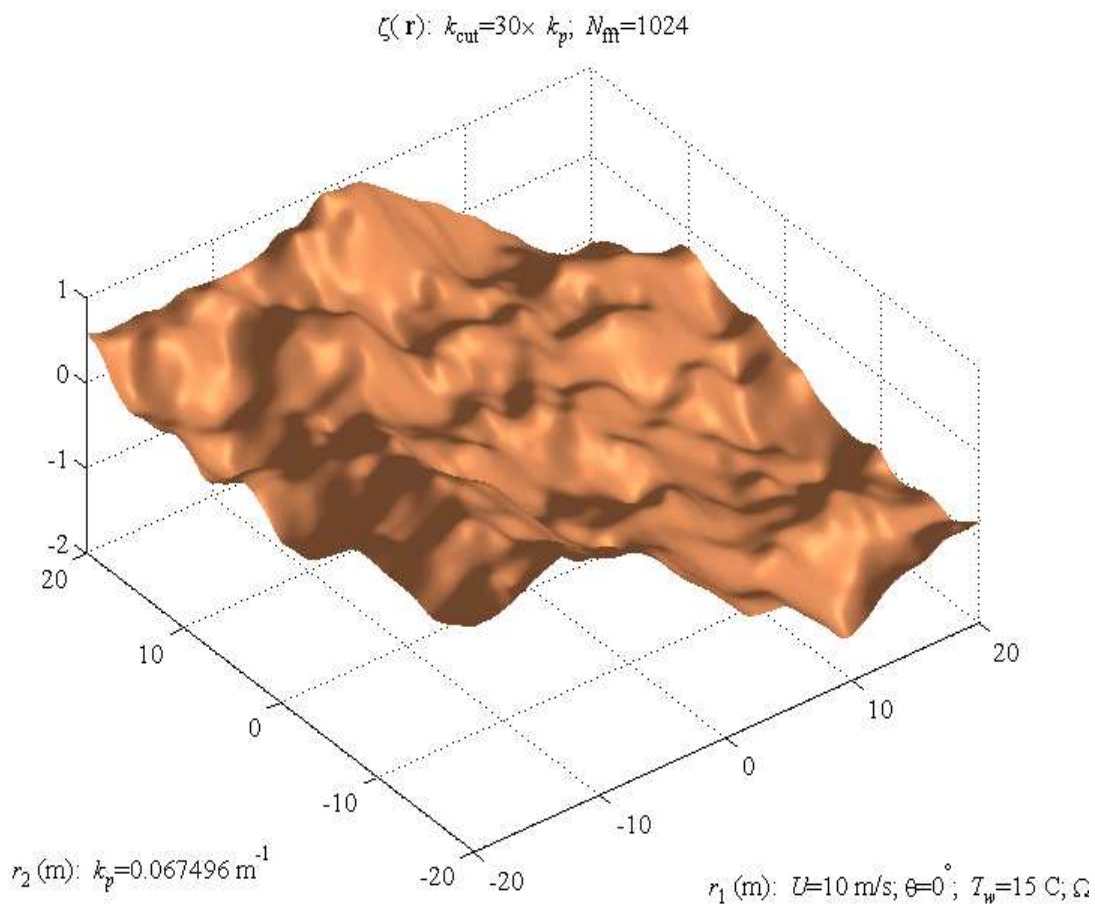


Figure 28: Gaussian sea surface.

⁹Allen, J. and Frank. J. Ryan [2000] Stochastic Sea-Surfaces for Radar Simulations—Phase 1: Frozen Gaussian Surfaces, *preprint*.

Figure 29 looks down upon a Gaussian sea over a $2 \times 2 \text{ km}^2$ patch. The wind is blowing along the r_1 axis and forcing the waves to line up approximately orthogonal to the r_1 axis. If a transmitter aims along the r_1 axis, this sea surface will scatter the bulk of the rays close to the incident plane. This scattering is the in-plane scattering of Section 2. This in-plane scattering approximates the full-surface scattering, but needs only a slice $\zeta(r_1, 0)$ parallel to r_1 axis for scattering.

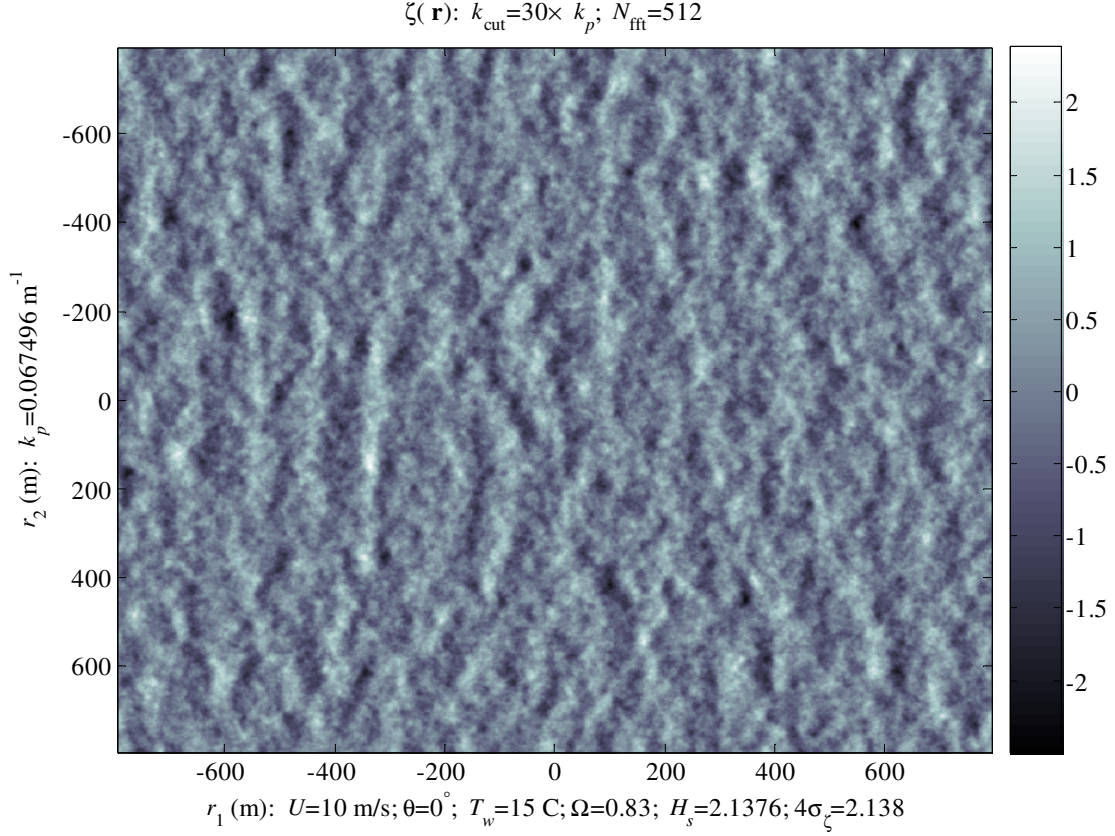


Figure 29: Top view of Gaussian sea surface.

6 Scattering From Sea-Surface Slices

Figure 30 illustrates the scattering model for the sea-surface slice. The incident plane wave reflects off the flat sea surface in the specular direction at every point. As the sea surface becomes non-flat, the incident plane wave reflects off the local tangent planes—subject now to shadowing and blocking. Shadowing occurs when the sea surface prevents the incident plane wave from illuminating a reflecting patch. Blocking occurs when the sea surface intercepts a reflected ray. Shadowing and blocking become significant at small grazing angles.

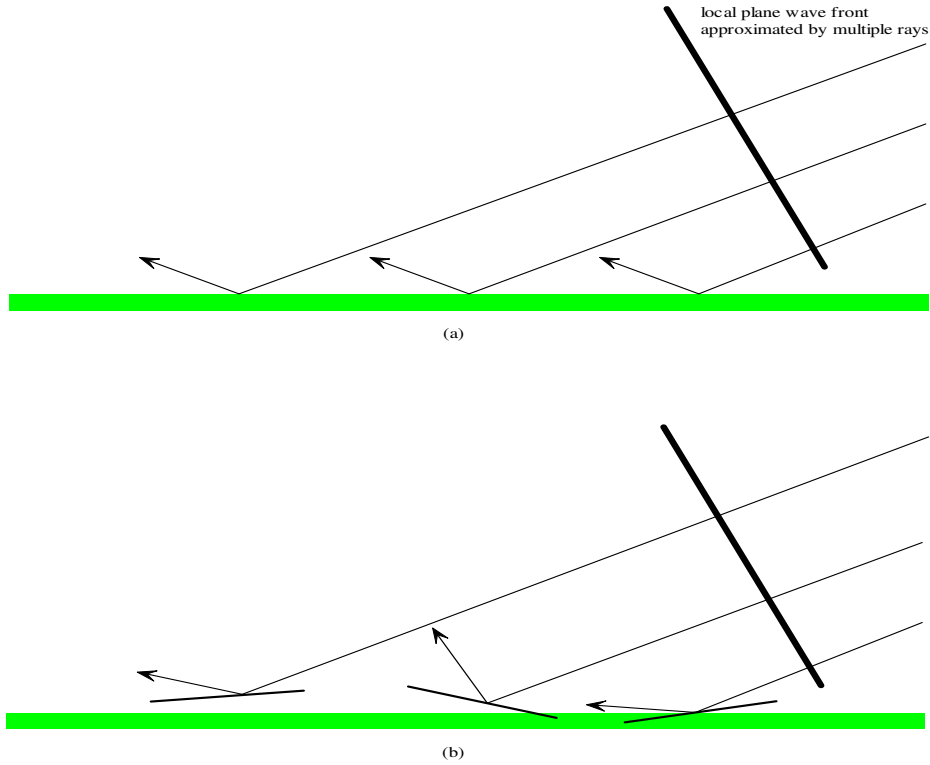


Figure 30: (a) Plane wave reflecting from flat surface; (b) plane wave reflecting from tangent planes.

Figure 31 shows a slice of a Gaussian sea surface along the r_1 axis. An antenna located at 100 meters has a 1-meter aperture (green). The incident, normal, and reflected rays are shown for those reflectors nearest the antenna. This plot is scaled so that the angles are correct—the angle of incidence equals the angle of reflection measured from the normal to the surface. The rest of the reflected rays come from points offscreen.

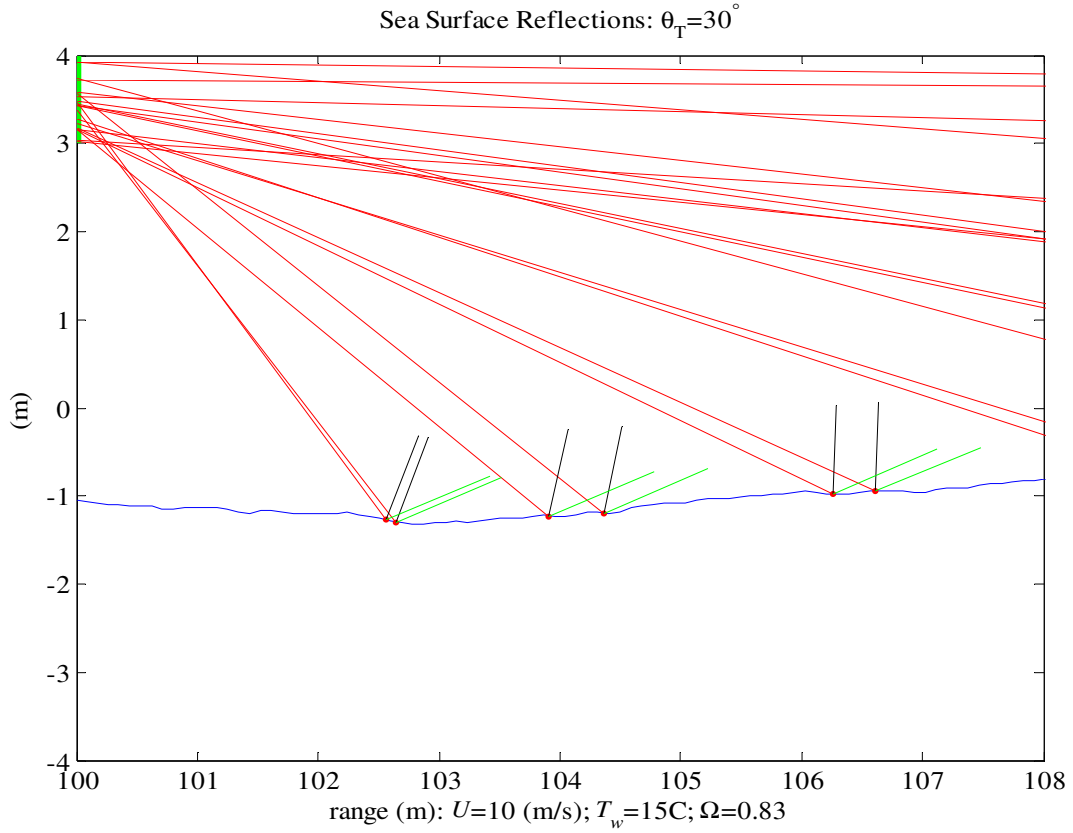


Figure 31: Closeup of incident and reflecting rays that arrive in the antenna's aperture.

Figure 32 enlarges the view to show a long slice of this Gaussian sea surface. Plotted on the sea surface are scattering points (red dots). These points are where the transmitted signal reflects off the sea surface and arrives in the antenna's aperture. That is, the reflecting patch is not shadowed from the transmitter or blocked to the receiver.

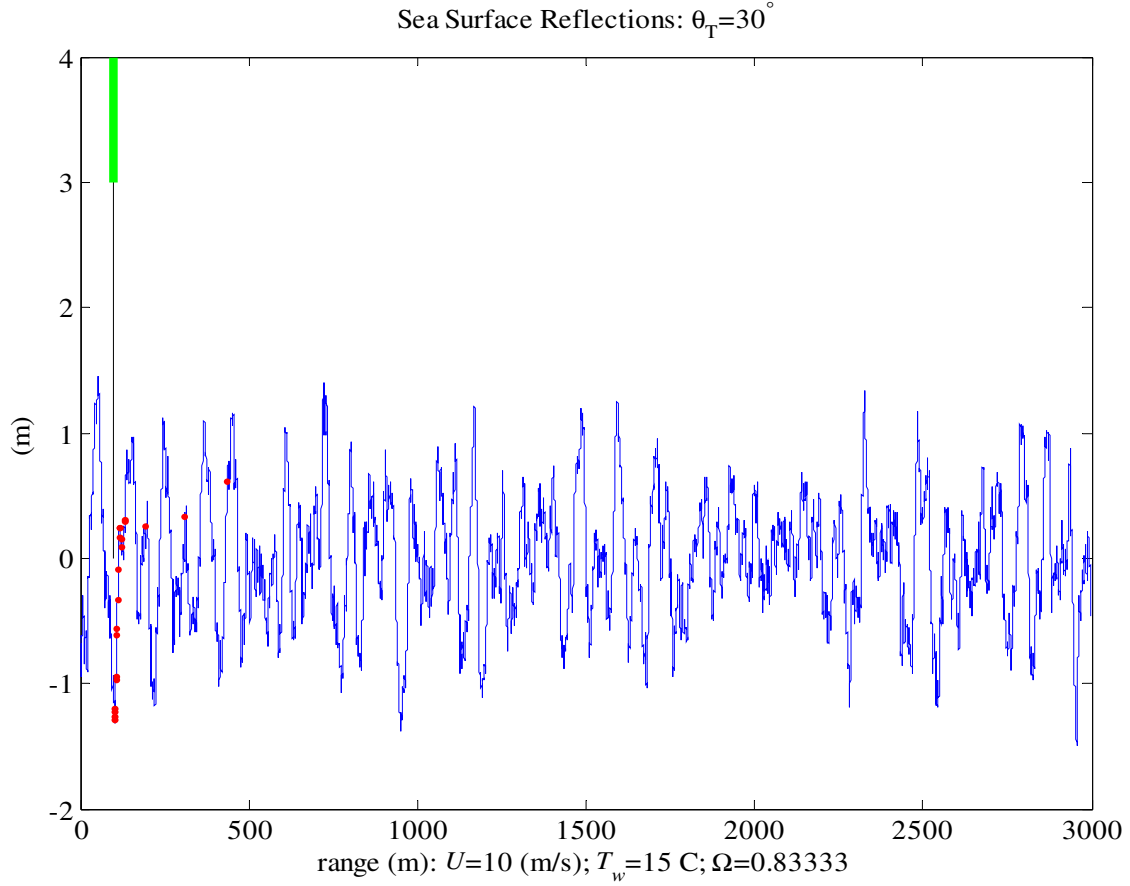


Figure 32: Gaussian sea slice and scattering points.

Associated with the n th scattering point are the following reflection parameters:

- Time delay $\Delta\tau_n$
- Elevation angle θ_n from the antenna pointing to the scattering point
- Grazing angle $\theta_{g,n}$
- Reflection coefficient $\Gamma_n = \Gamma_0(\theta_{g,n})$

These scattering points model the delay-spread function by summing over all the reflectors:

$$\begin{aligned} h(r, \tau) &= G_R^{1/2}(\theta_T) \delta(\tau) + a(\theta_T) \sum_{n=1}^{N_r} G_R^{1/2}(\theta_n) \Gamma_0(\theta_{g,n}) \delta(\tau - \Delta\tau_n) \\ &\approx \left\{ G_R^{1/2}(\theta_T) + a(\theta_T) \sum_{n=1}^{N_r} G_R^{1/2}(\theta_n) \Gamma_n \right\} \delta(\tau). \end{aligned}$$

The diffuse scatter is omitted because we are picking up this effect by summing over all the reflectors. The *patch factor* $a(\theta_T)$ blends the rough surface to the flat-surface model. This section will show that the time delays are negligible for a narrow-band surface-level antenna. The negligible delays allow us to approximate the delay-spread function like multiplicative noise. In this case, we write the delay-spread function as

$$h(r) \approx G_R^{1/2}(\theta_T) + a(\theta_T) \sum_{n=1}^{N_r} G_R^{1/2}(\theta_n) \Gamma_n \quad (16)$$

to act on the signal as a multiplication operator,

$$s_R(t) = s_T(t) \times h(r(t)).$$

Here, $r(t)$ denotes the position of the antenna at time t . Consequently, the multipath received at the antenna as the antenna travels across the sea surface at various speeds can be handled by resampling $h(r)$. The following sections compute the time delays, angles, and the patch factor $a(\theta_T)$ that blends the rough surface to the flat-surface model.

6.1 Flat-Surface Blending

The patch factor $a(\theta_T)$ compensates for the discretization of the sea surface into Δr -sized patches and blends the rough-surface scattering to the flat-surface scattering as the sea surface gets smoother. Denote the upper and lower heights of the antenna aperture as h_R^+ and h_R^- , respectively. Let Δr denote the increment of the range samples. The simulations all use the plate size from Didascalou [15]:

$$\Delta r \approx \frac{\lambda_T}{10}.$$

The number of rays that could reflect off the “footprint” of the antenna looking at a flat surface is

$$N_r = \text{round} \left(\frac{h_R^+ - h_R^-}{\Delta r \tan(\theta_T)} \right). \quad (17)$$

With all the tiny time delays set to zero, the flat-surface multipath scales to the flat surface discretized with Δr as

$$\begin{aligned} h(r) &= G_R^{1/2}(\theta_T) + N_r^{-1} \sum_{n=1}^{N_r} G_R^{1/2}(-\theta_T) \Gamma_{0,C}(\theta_T) \\ &= G_R^{1/2}(\theta_T) + G_R^{1/2}(-\theta_T) \Gamma_{0,C}(\theta_T). \end{aligned}$$

Consequently, the patch factor,

$$a(\theta_T) = \Delta r \frac{\tan(\theta_T)}{h_R^+ - h_R^-}$$

is an estimate of the number of Δr -size reflecting patches that blend rough-surface scattering to flat-surface scattering as the wave heights diminish.

6.2 Reflecting Points

Figure 33 illustrates the geometry required for a ray to reflect off the sea surface and arrive in the antenna aperture. There do exist back reflections—reflections that come from behind the antenna. However, if the transmitter’s elevation angle is small, and the sea is relatively smooth, back reflections into the surface-level antenna are rare. Appendix A discusses back reflections and quantifies this claim.

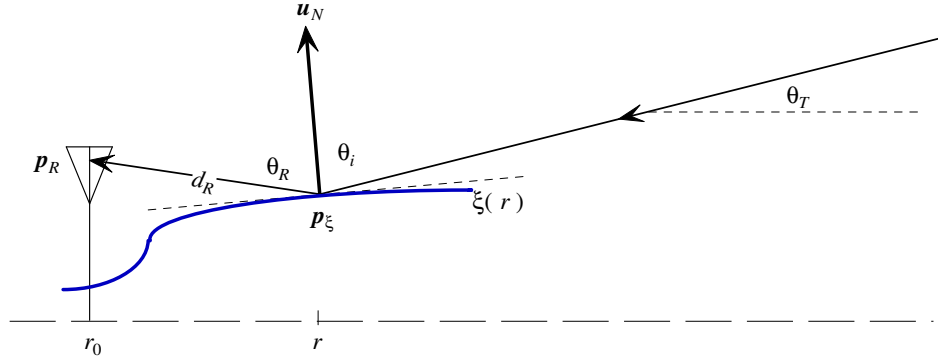


Figure 33: Sea surface reflecting a ray.

The sea surface is the graph of $\zeta(r)$. Points on the sea surface have the form,

$$\mathbf{p}_\zeta = \begin{bmatrix} r \\ \zeta(r) \end{bmatrix}.$$

Let \mathbf{u}_N denote the upward pointing normal at \mathbf{p}_ζ . The unit vector pointing to the transmitter is

$$\mathbf{u}_T = \begin{bmatrix} \cos(\theta_T) \\ \sin(\theta_T) \end{bmatrix}.$$

The angle of incidence θ_i is the angle between \mathbf{u}_N and \mathbf{u}_T :

$$\cos(\theta_i) = \mathbf{u}_N^T \mathbf{u}_T. \quad (18)$$

By adding the angles in Figure 33, the unit vector pointing along the reflected ray is

$$\mathbf{u}_R = \begin{bmatrix} \cos(\theta_R) \\ \sin(\theta_R) \end{bmatrix} \quad (\theta_R = \theta_T + 2\theta_i).$$

For the reflected ray to arrive in the receiver's antenna aperture,

$$\mathbf{p}_R = \begin{bmatrix} r_0 \\ h_R \end{bmatrix} \quad (h_R^- \leq h_R \leq h_R^+),$$

there must be a $d_R > 0$ such that

$$\mathbf{p}_R = \mathbf{p}_\zeta + d_R \mathbf{u}_R$$

or that

$$0 < d_R = \frac{r_0 - r}{\cos(\theta_R)}. \quad (19)$$

Consequently, the reflected ray is in the antenna's aperture provided

$$h_R^- \leq \zeta(r) + (r_0 - r) \tan(\theta_R) \leq h_R^+. \quad (20)$$

Equations 19 and 20 constitute the basic reflection algorithm. The only modification is that if a ray passes these tests, it still must be tested for blockage by the sea surface.

6.3 Time Delay

Figure 34 shows the time delay between the direct and reflected rays (and is distorted for clarity). The reflected ray travels the diagonal d_R from the point of reflection,

$$\mathbf{p}_\zeta = \begin{bmatrix} r \\ \zeta(r) \end{bmatrix},$$

to the antenna

$$\mathbf{p}_R = \begin{bmatrix} r_0 \\ h_R \end{bmatrix}.$$

This reflected ray travels the distance

$$d_R = \|\mathbf{p}_R - \mathbf{p}_\zeta\|.$$

At the same time the reflected ray starts for the antenna, the direct ray starts from

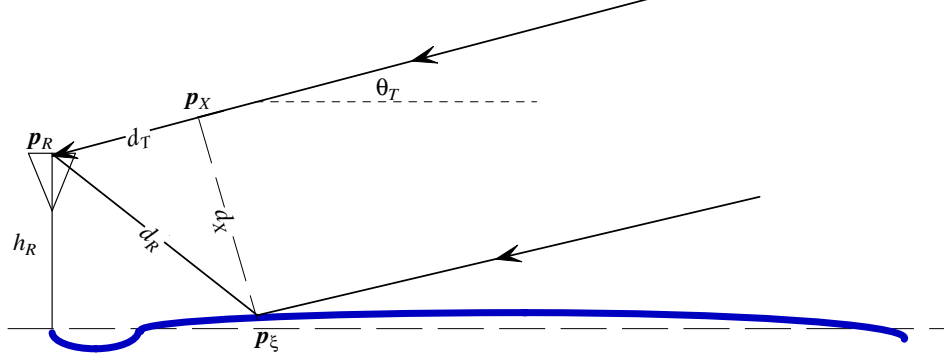


Figure 34: Time-delay geometry.

the crossing point \mathbf{p}_X to the antenna so the time delay is the difference,

$$\Delta t = \frac{d_R - d_T}{c}.$$

The crossing point is located at

$$\mathbf{p}_X = \mathbf{p}_\zeta + d_X e^{i(\theta_T + \pi/2)} = \mathbf{p}_R + d_T e^{i\theta_T}.$$

The linear system is

$$\begin{aligned} \mathbf{p}_\zeta - \mathbf{p}_R &= d_T e^{i\theta_T} - d_X e^{i(\theta_T + \pi/2)} \\ &= d_T \begin{bmatrix} \cos(\theta_T) \\ \sin(\theta_T) \end{bmatrix} - d_X \begin{bmatrix} -\sin(\theta_T) \\ \cos(\theta_T) \end{bmatrix} \\ &= \begin{bmatrix} \cos(\theta_T) & \sin(\theta_T) \\ \sin(\theta_T) & -\cos(\theta_T) \end{bmatrix} \begin{bmatrix} d_T \\ d_X \end{bmatrix} \end{aligned}$$

so that

$$\begin{aligned} d_T &= -1 \times \det \begin{bmatrix} r - r_0 & \sin(\theta_T) \\ \zeta - h_R & -\cos(\theta_T) \end{bmatrix} \\ &= (r - r_0) \cos(\theta_T) + (\zeta - h_R) \sin(\theta_T). \end{aligned}$$

The time delay is

$$\begin{aligned} \Delta t &= c^{-1} \left\{ \sqrt{(r - r_0)^2 + (\zeta - h_R)^2} \right. \\ &\quad \left. - ((r - r_0) \cos(\theta_T) + (\zeta - h_R) \sin(\theta_T)) \right\}. \end{aligned} \quad (21)$$

In the special case of $\zeta = r_0 = 0$, Equation 21 does reduce to Equation 4. However, Equation 21 is an excellent example of the numerical difficulties of extracting

a tiny difference by subtracting two large numbers. The following implementation of Equation 21 appears to overcome this numerical problem—for now. For brevity, set

$$\Delta r = r - r_0, \quad \Delta h = \zeta - h_R.$$

Observe that Δh is negative when the antenna is looking down on the reflector. In this notation,

$$d_R = \sqrt{\Delta r^2 + \Delta h^2}.$$

If we use the positive angle elevation angle from the antenna to the reflector,

$$\tan(\theta_\zeta) = \frac{-\Delta h}{\Delta r},$$

the time delay can take the forms:

$$\begin{aligned} \Delta t &= c^{-1} \{d_R - (\Delta r \cos(\theta_T) + \Delta h \sin(\theta_T))\} \\ &= \frac{d_R}{c} \{1 - \cos(\theta_T + \theta_\zeta)\} \\ &= 2 \frac{d_R}{c} \sin^2 \left(\frac{\theta_T + \theta_\zeta}{2} \right). \end{aligned}$$

6.4 Reflected Angles

In terms of Equation 16, let the n th reflector be located at

$$\begin{bmatrix} r_n \\ \zeta(r_n) \end{bmatrix}$$

and have incident angle $\theta_{i,n}$. Because the incident angle is measured from the normal at the point of reflection and the reflection coefficients are functions of the grazing angle, the reflection coefficient Γ_n of Equation 16 is computed as

$$\Gamma_n = \Gamma_{0,C}(\theta_{g,n}); \quad \theta_{g,n} = \pi/2 - \theta_{i,n}.$$

Likewise, the elevation angle θ_n from the antenna to the n reflector is

$$\theta_n = \tan^{-1} \left(\frac{\zeta(r_n) - h_R}{r_n - r_0} \right).$$

6.5 Scattering Examples

Figure 32 is our baseline scattering simulation. Table 3 reports on the scattering parameters extracted from each reflector. We use these parameters to model the channel in Equation 16. Because the antenna is fixed at a single position, we have only a “slice” of the delay-spread function.

Table 3: Reflection data: $f = 250$ (MHz); $\sigma_\zeta = 0.5028$ (m); $\theta_T = 30^\circ$.

$\Delta\tau$ (ns)	θ_n (deg)	$ \Gamma_{0,C} $	$\angle\Gamma_{0,C}$ (deg)	θ_g (deg)
8.768425	-61.795469	0.918591	-3.989633	45.798992
8.897965	-61.087893	0.918344	-4.000575	45.217588
10.387951	-50.400428	0.914882	-4.154361	39.138560
11.387721	-47.120155	0.914587	-4.167444	38.740913
11.539623	-35.581093	0.907388	-4.486519	31.739575
11.677130	-33.912428	0.906298	-4.534742	30.967993
11.973236	-25.329341	0.899442	-4.837518	27.041772
11.855091	-24.412361	0.898195	-4.892498	26.456014
13.256817	-19.157287	0.895087	-5.029368	25.121505
12.497451	-16.296921	0.889205	-5.287804	22.983759
12.617580	-16.061290	0.889020	-5.295931	22.923185
13.620735	-10.909591	0.880003	-5.690636	20.350789
14.290554	-10.572835	0.879618	-5.707443	20.254948
13.660733	-10.017306	0.876356	-5.849775	19.479986
14.924795	-9.102366	0.873784	-5.961886	18.911842
16.353645	-8.545893	0.875865	-5.871217	19.368592
19.623514	-5.572819	0.866038	-6.298543	17.392974
21.318665	-5.524093	0.869955	-6.128452	18.128062
48.720103	-1.929041	0.857431	-6.671206	15.973054
100.354341	-0.860771	0.854128	-6.813793	15.488003
155.560856	-0.492800	0.852544	-6.882126	15.265474

If we move the antenna to a different position, a different channel or different “slice” of the delay-spread function is observed. Figure 35 displays all the channels obtained by moving the antenna along the sea surface. Equivalently, we have collected slices of the delay-spread function. Consequently, this plot shows the support of the “delay-spread” function. The horizontal axis is the delay. The vertical axis is the antenna’s position. As the antenna moves across the sea surface, the nearby waves offer a scintillating effect, while the more distant waves offer long-term reflections delays up to 200 ns. Even these longer delays are not resolvable in a 100-kHz receiver.

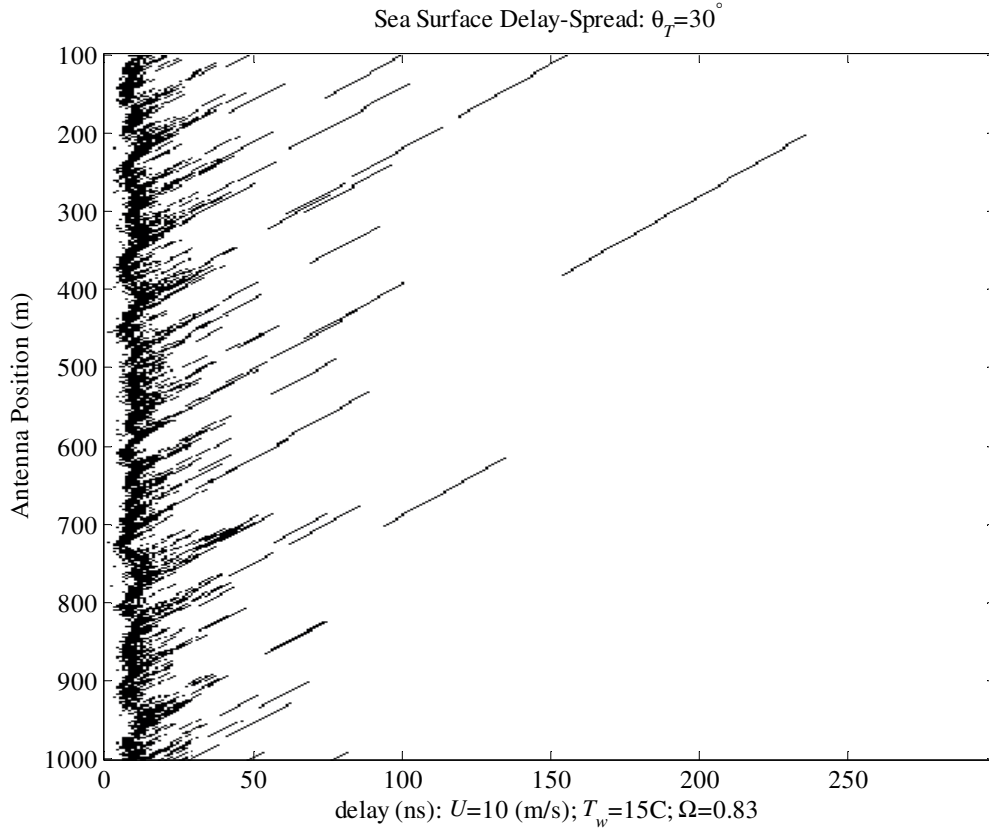


Figure 35: Range and delays of the sea surface; transmitter’s elevation $\theta_T = 30^\circ$.

For comparison, Figures 36, 37, and 38 successively decrease the transmitter's elevation angle. The large-scale structure of the sea surface is lost as the elevation angle is lowered—only close-in reflectors are operating.

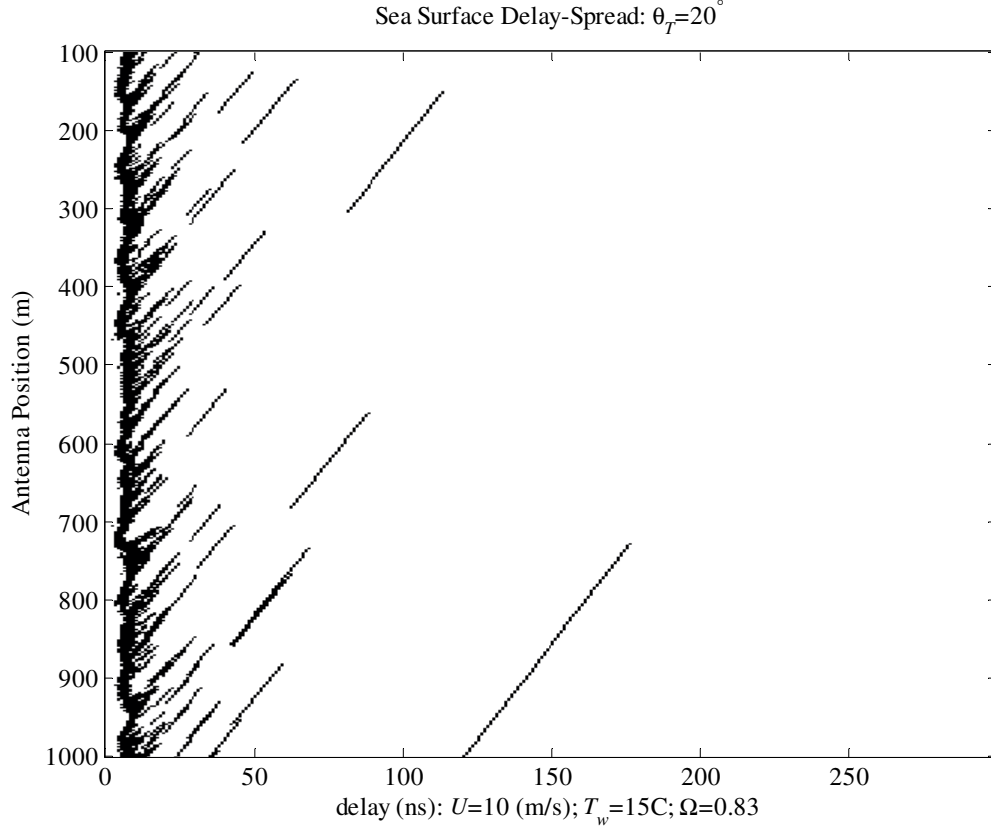


Figure 36: Range and delays of the sea surface; transmitter's elevation $\theta_T = 20^\circ$.

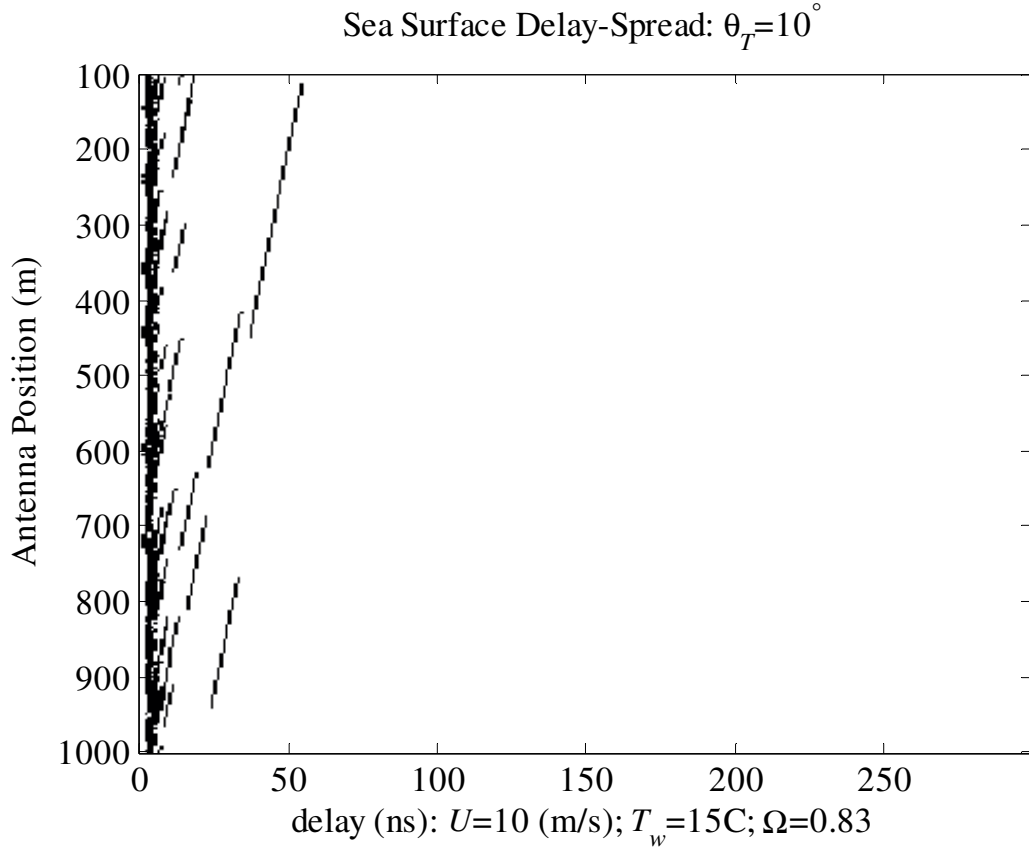


Figure 37: Range and delays of the sea surface; transmitter's elevation $\theta_T = 10^\circ$.

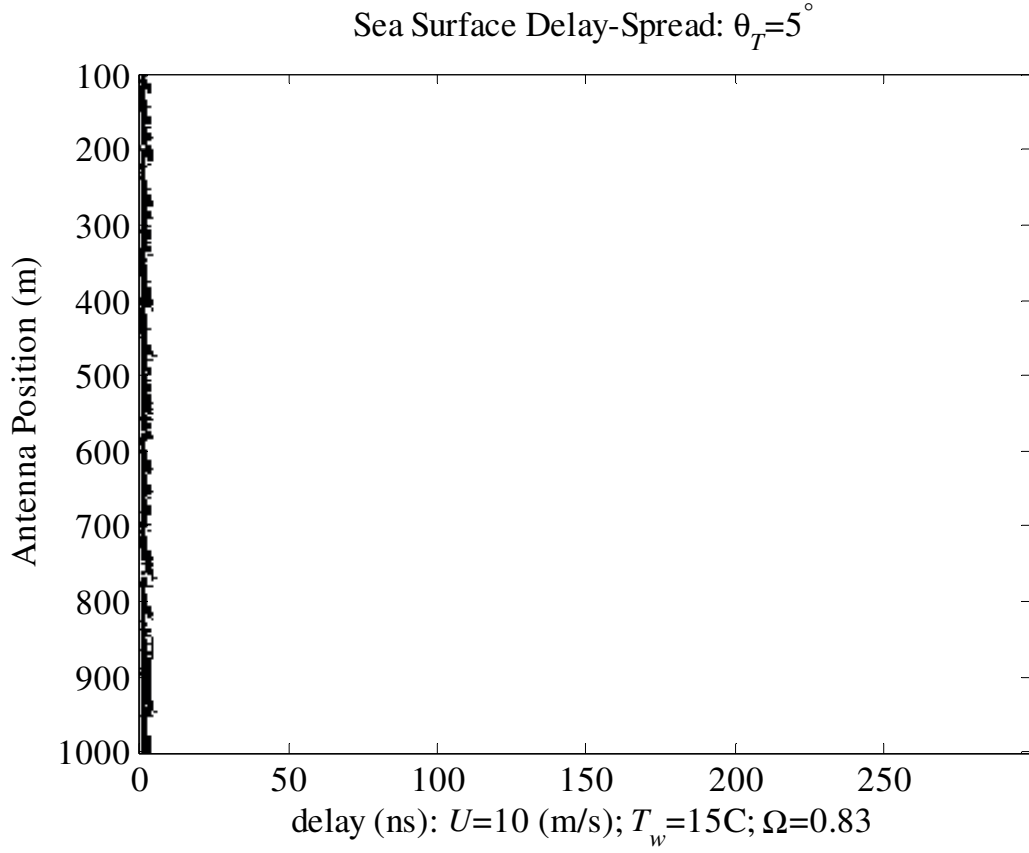


Figure 38: Range and delays of the sea surface; transmitter's elevation $\theta_T = 5^\circ$.

Table 4 lists the channel from the $\theta_T = 5^\circ$ simulation. The delays are not in order because neighboring reflectors shoot rays that land anywhere in the antenna aperture covering the height between 3 and 4 meters. (See the closeup in Figure 31.) Consequently, this 1-meter aperture “jumbles” the delays. (The same effect occurs in Table 3.) The reflection coefficients are still relatively large because the grazing angle is between 2 to 10 degrees.

Table 4: Reflection data: $f = 250$ (MHz); $\sigma_\zeta = 0.5028$ (m); $\theta_T = 5^\circ$.

$\Delta\tau$ (ns)	θ_n (deg)	$ \Gamma_{0,C} $	$\angle\Gamma_{0,C}$ (deg)	θ_g (deg)
2.261470	−13.246107	0.776118	−10.120476	8.866531
2.540322	−10.765743	0.770639	−10.348577	8.591683
1.855261	−9.942833	0.732873	−11.907600	7.024713
1.987390	−9.211891	0.728725	−12.077468	6.880722
1.812893	−7.967224	0.702353	−13.151415	6.062877
2.082713	−6.274682	0.695311	−13.436511	5.869202
1.798164	−3.639959	0.636543	−15.789676	4.550052
1.662531	−2.565343	0.591438	−17.567117	3.795084

As the elevation angle decreases, the number of scatterers decreases. Although some rays were still arriving when the elevation angle was $\theta_T = 2^\circ$, dropping the elevation angle to 1 degree eliminated the specular reflection: **no rays were reflected into the antenna aperture**. At this low grazing angle, only the wave tops are potential scatterers. This restriction of the scattering to the wave tops significantly reduces the scattering area. Moreover, the sea surface is discretized at increments of size $\Delta r = 0.1$ meter. The relatively few tangent plates that approximate the random wave top typically will not precisely align in both height and angle to scatter into the antenna—provided no shadowing or blocking occurs. Therefore, the specular reflections will decrease with decreasing elevation angle.

7 Specular Multipath Noise Simulations

The tangent-plane scattering model is applied to several sea surfaces to simulate the multipath noise caused by specular reflections. Section 7.1 examines the multipath receive by the Baseline Quadrifilar Antenna. Section 7.2 applies the same simulations to the OE-538 Low-Angle Antenna. The simulations show the following:

- The specular multipath noise migrates to the upper elevation angles as the sea becomes rougher
- For the smoother seas, the specular multipath noise peaks in the low angles
- The specular multipath rolls off at very low grazing angles

7.1 Baseline Quadrifilar Antenna

The Baseline Quadrifilar Antenna is assumed to be an ideal RCP antenna. In the flat-surface scattering model of Equation 11, this antenna receives the direct path and the single specular reflection as

$$h(r) = G_R(\theta_T)^{1/2} + G_R(-\theta_T)^{1/2}\Gamma_{0,C}(\theta_T).$$

For this antenna, the direct-to-specular ratio (DSR) from this flat surface is

$$\text{DSR}(\theta_T) = \frac{G_R(\theta_T)}{G_R(-\theta_T)|\Gamma_{0,C}(\theta_T)|^2}.$$

Figure 39 plots the DSR for a flat sea surface. As the elevation angle θ_T decreases to zero, $G_R(\pm\theta_T)$ converges to $G_R(0)$ and the reflection coefficient vanishes. Consequently, the DSR becomes unbounded as θ_T decreases to zero. This same effect appears in the sea-surface simulations, but is confounded by shadowing and blocking.

Figures 40, 41, and 41 plot the specular multipath noise scattered from the sea surface. The multipath noise is obtained from the 1-meter aperture of Figure 32. The antenna pattern of Figure 13 resides in the aperture. The antenna starts at $r = 100$ and moves 100 meters in 0.1-meter increments. At each increment, the multipath noise of Equation 16 is computed. This magnitude of the noise is plotted as a function of range. The dB plot scales the noise to the direct path. As the elevation angle θ_T decreases, the surface appears smoother and the RCP reflection coefficient decreases.

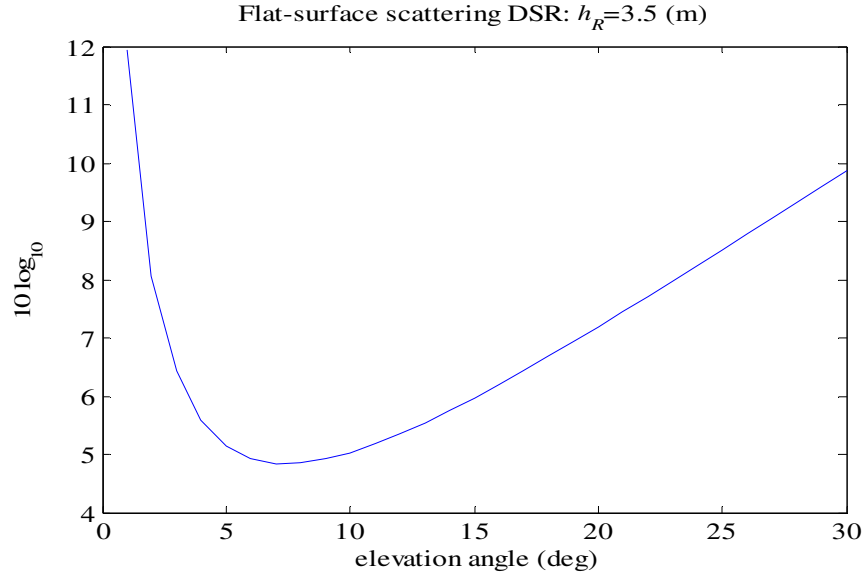


Figure 39: Baseline Quadrifilar Antenna DSR.

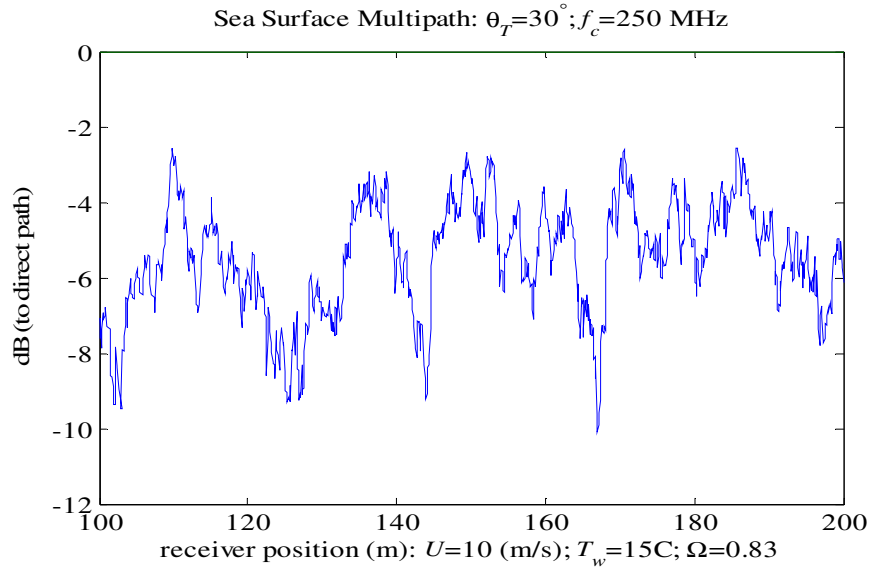


Figure 40: Sea-surface multipath; transmitter at 30° elevation; Baseline Quadrifilar Antenna.

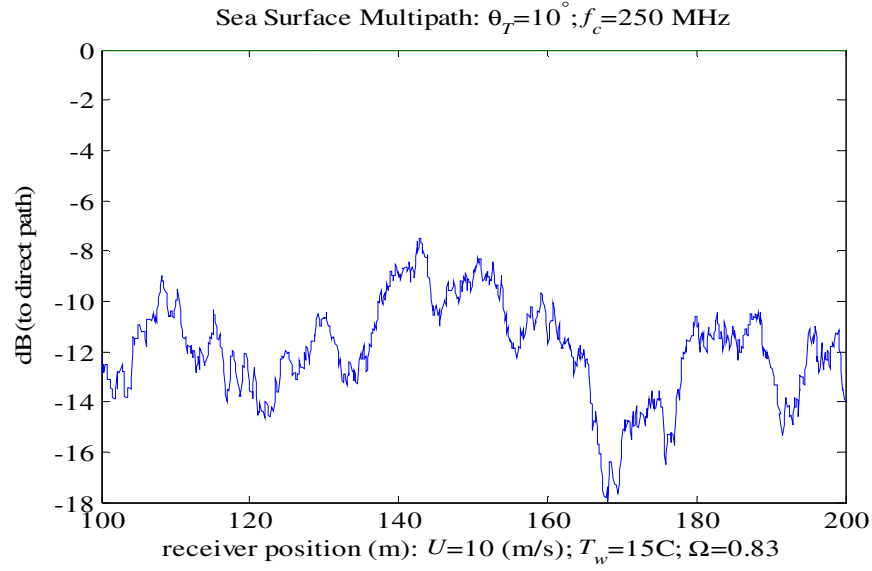


Figure 41: Sea-surface multipath; transmitter at 10° elevation; Baseline Quadrifilar Antenna.

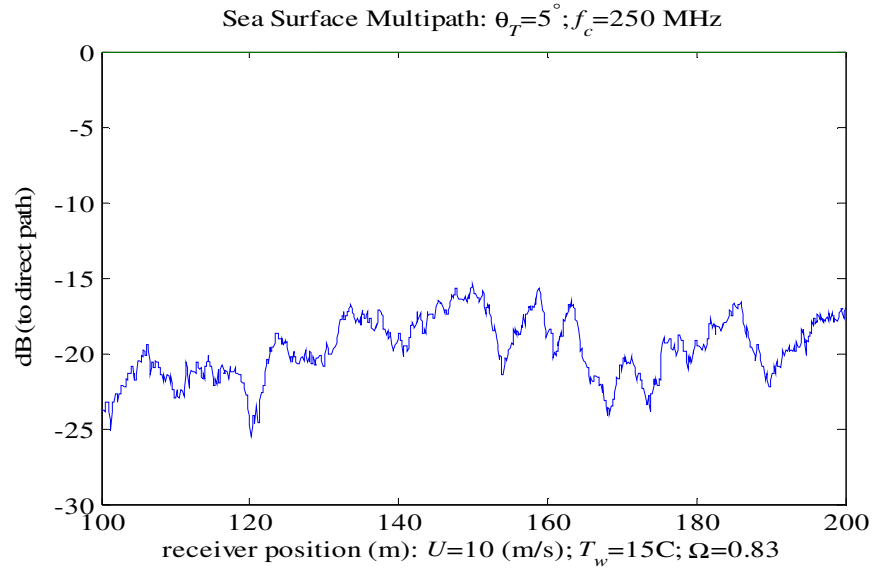


Figure 42: Sea-surface multipath; transmitter at 5° elevation; Baseline Quadrifilar Antenna.

Figure 43 displays all the preceding noise plots in the context of the range and elevation angle plane. The antenna is held at a height of 3 meters and moved across the sea surface. At each range, the elevation angle sweeps over 0 to 30 degrees. The noise power—scaled to the direct path—is plotted as a function of range and elevation angle. The image shows a relatively strong return at the higher elevation angles and little return at the lower angles. At the lower elevation angles, the grazing angles tend to be small. Consequently, the sea surface reflects less of the incident RCP signal. Moreover, at very low angles, almost all of the specular reflections are blocked—the waves either shadow the scattering patches or, after reflection, the waves block the reflected ray to the antenna. Consequently, this ray-tracing model has the specular noise rolling off as the elevation angle is decreased.

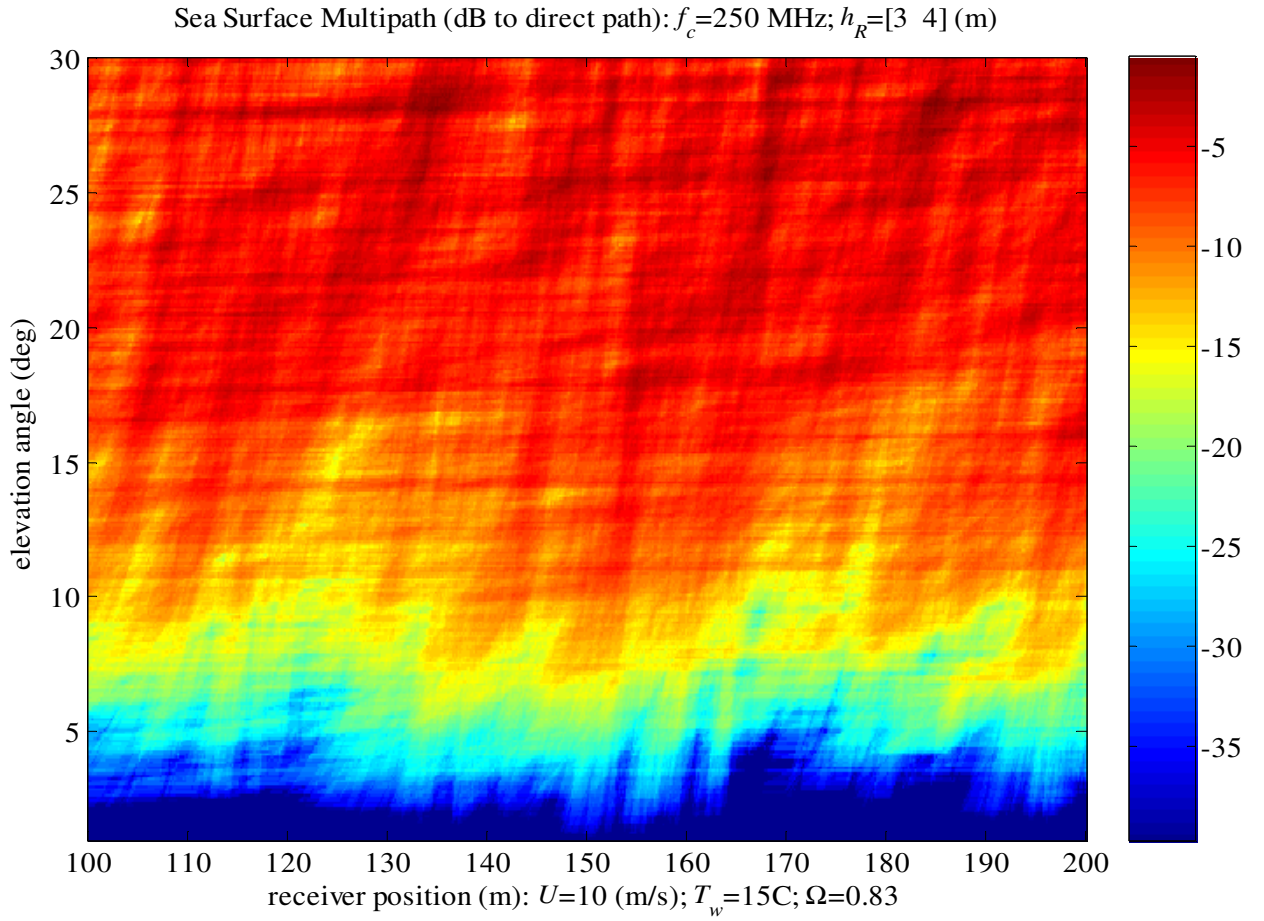


Figure 43: Sea-surface multipath for the Baseline Quadrifilar Antenna.

Figure 44 shows that when the wind is decreased to 5 m/s, the sea surface becomes smoother and the significant wave height decreases. The large-scale waves still line up orthogonal to the wind. Consequently, the bulk of the scattering will be close to the incident plane and is approximated by in-plane scattering off a slice of the sea surface taken along the r_1 axis.

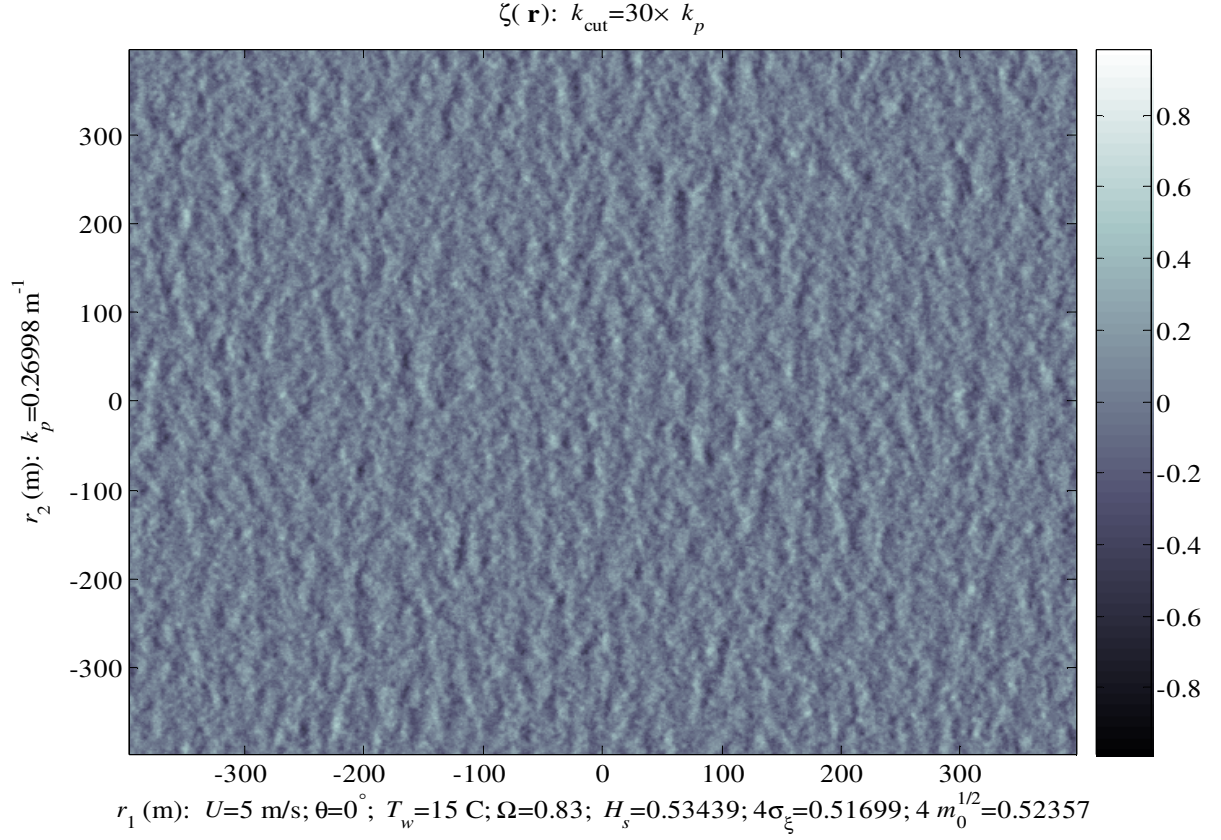


Figure 44: Sea-surface realization with wind at 5 m/s.

Figure 45 shows the corresponding the scattering image from such a sea surface—the wind is only moving at 5 m/s rather than the 10 m/s of Figure 43. There is still blockage and shadowing at the low elevation angles—but the effect is less than the rougher sea with the 10 m/s wind.

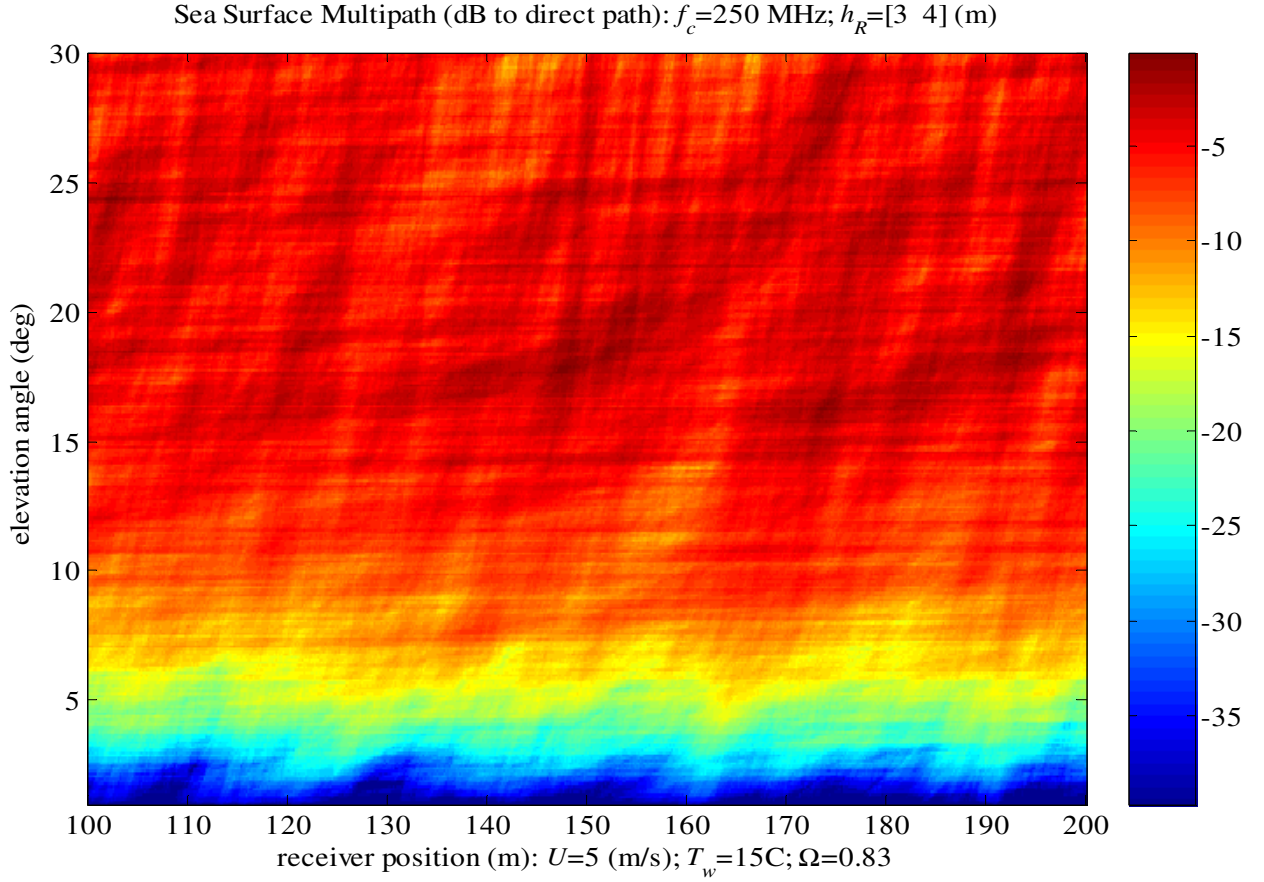


Figure 45: Sea-surface multipath for the Baseline Quadrifilar Antenna; wind at 5 m/s.

As the wind decreases, the sea becomes smoother. Figure 46 shows that when wind is only blowing at 1 m/s, the scattering is nearly uniform in range and follows the DSR curve of Figure 39.

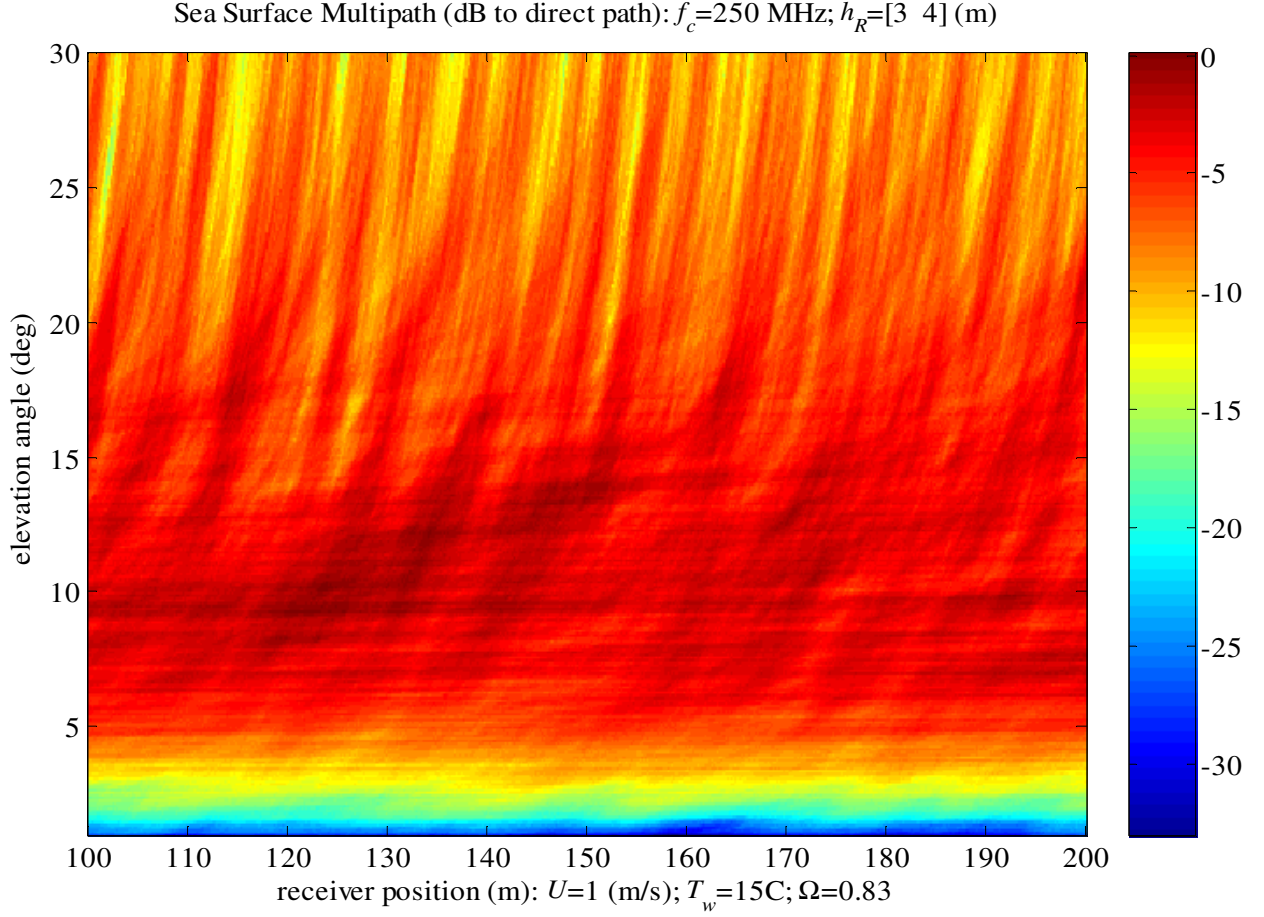


Figure 46: Sea-surface multipath; Baseline Quadrifilar Antenna; wind at 1 m/s.

7.2 OE-538 Antenna

The flat-surface scattering model of Equation 12 consists of the direct path and the single specular reflection that splits the RCP signal into RCP and LCP rays that arrive at a non-ideal antenna:

$$h(r) = G_{R,RCP}(\theta_T)^{1/2} + G_{R,RCP}(-\theta_T)^{1/2}\Gamma_{0,RCP}(\theta_T) \\ + G_{R,LCP}(-\theta_T)^{1/2}\Gamma_{0,LCP}(\theta_T).$$

The DSR for this flat-surface model and antenna is

$$\text{DSR}(\theta_T) = \frac{G_{R,RCP}(\theta_T)}{|G_{R,RCP}(-\theta_T)^{1/2}\Gamma_{0,RCP}(\theta_T) + G_{R,LCP}(-\theta_T)^{1/2}\Gamma_{0,LCP}(\theta_T)|^2}.$$

Figure 47 plots the flat-surface DSR for a sea surface. As the elevation angle θ_T decreases to zero, the reflection coefficient $\Gamma_{0,RCP}(\theta_T)$ converges to zero so that

$$\text{DSR}(0^\circ) = \frac{G_{R,RCP}(0^\circ)}{G_{R,LCP}(0^\circ)|\Gamma_{0,LCP}(0^\circ)|^2} < \infty.$$

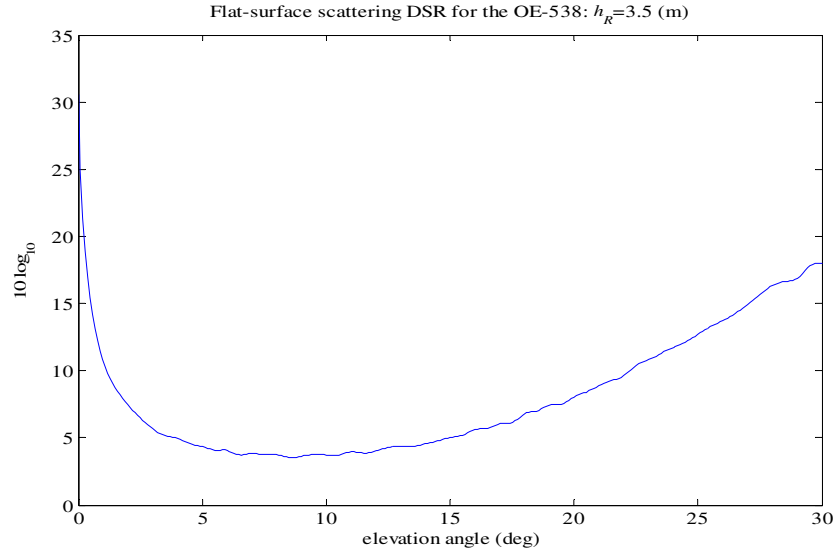


Figure 47: DSR for the OE-538

In contrast to the Baseline Quadrifilar Antenna, the OE-538 is still responding to the cross-polarized reflections so that the DSR does not become unbounded as θ_T decreases to zero. This same effect appears in the sea-surface simulations, but is confounded by shadowing and blocking. Figures 48, 49, and 50 show the specular multipath for the wind at 10, 5, and 1 m/s. Decreasing the wind gives a smoother sea surface. The smoother sea surfaces migrate the multipath noise from the upper elevations angles to the lower elevation angles. The smoothest sea reflects the multipath noise essentially as the DSR curve in Figure 47.

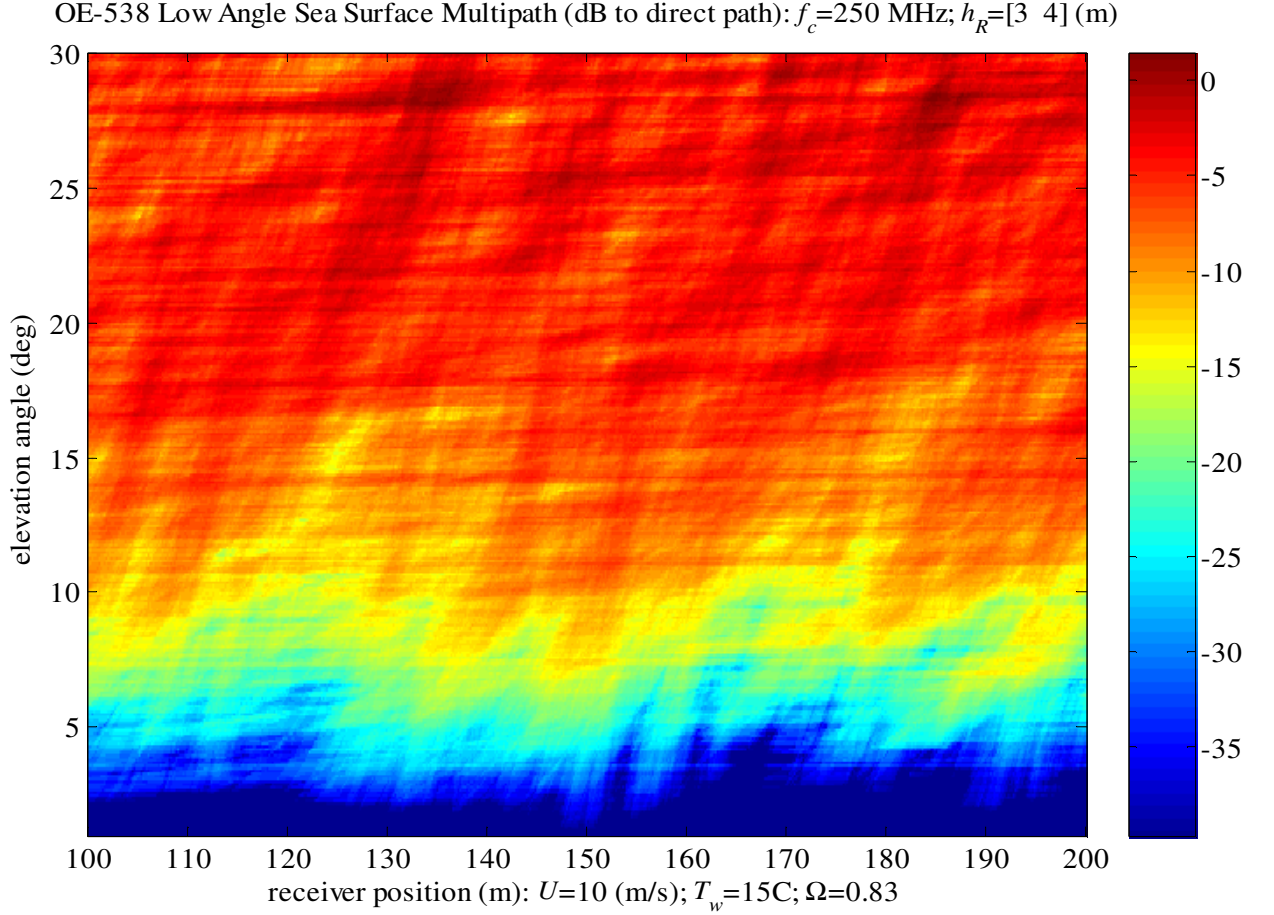


Figure 48: Sea-surface multipath for the OE-538 Low-Angle Antenna.

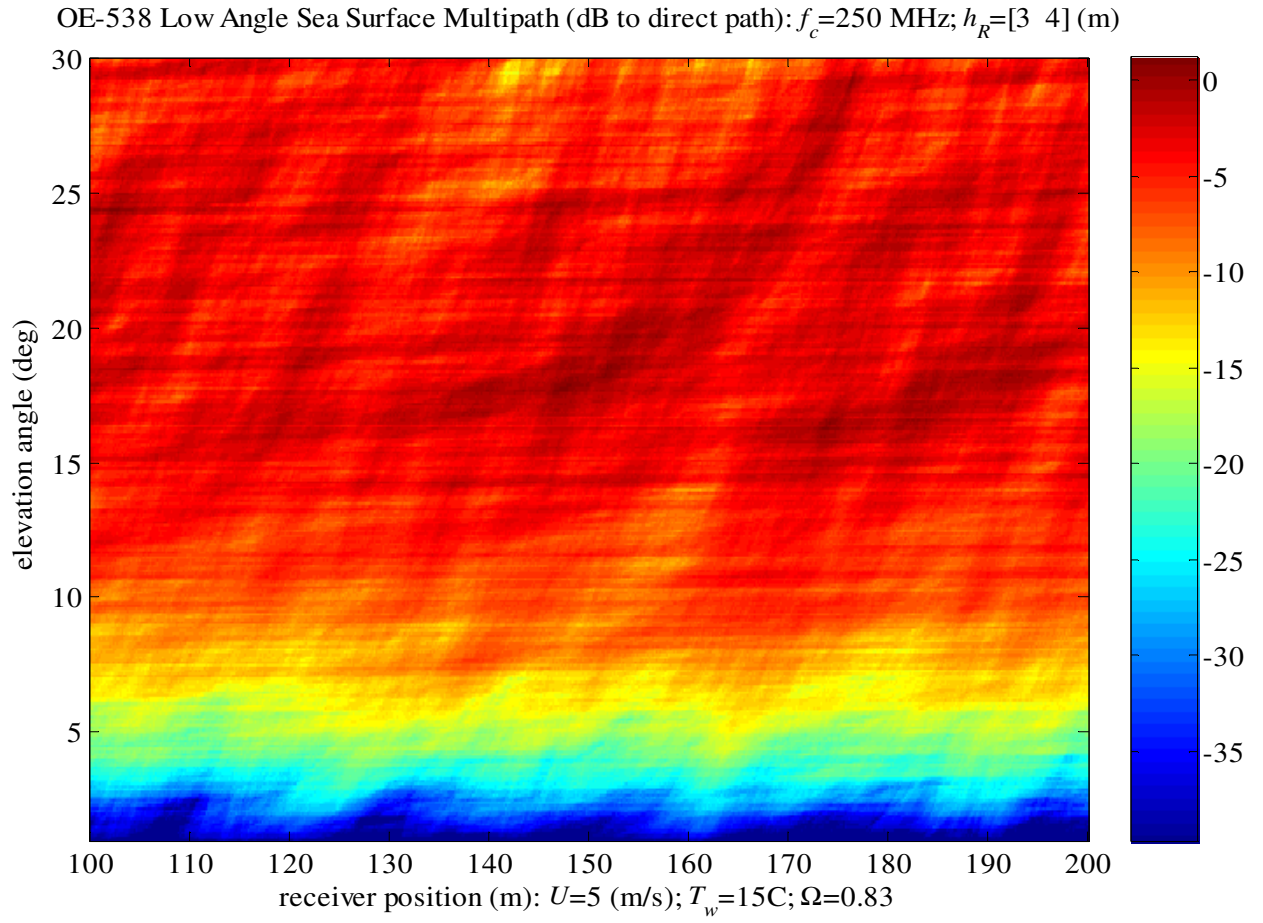


Figure 49: Sea-surface multipath for the OE-538 Low-Angle Antenna; wind at 5 m/s.

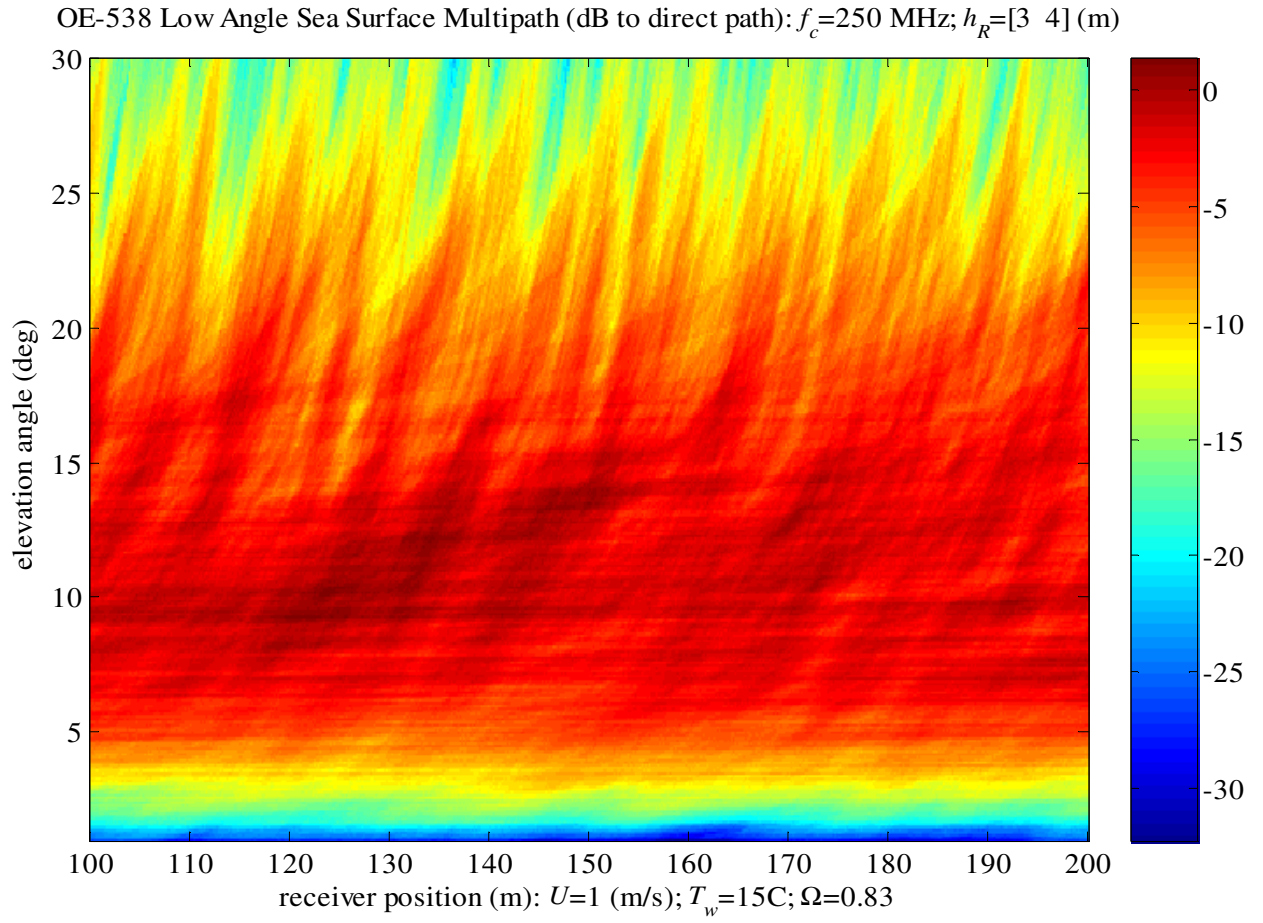


Figure 50: Sea-surface multipath for the OE-538 Low-Angle Antenna; wind at 1 m/s.

7.3 Multipath Phase

The multipath noise is at baseband, so takes on complex values. The preceding section plotted the amplitude as a function of the receiving antenna's range and the transmitter's elevation angle. This section shows the corresponding plots for the multipath phase. Figure 51 shows that the phase is relatively stable for each elevation angle. The exceptions are found at the low elevation angles where the magnitude is small and no phase unwrapping was used to keep the angle continuous. Tables 3 and 4 show why the phase is relatively stable—the contribution of the delays to the phase is negligible. These tables also show that the grazing angle does not vary much—probably because of the narrow aperture of the receiving antenna and its short distance from the sea surface. Because the grazing angles are relatively constant, the phase of the reflection coefficient is also relatively constant.

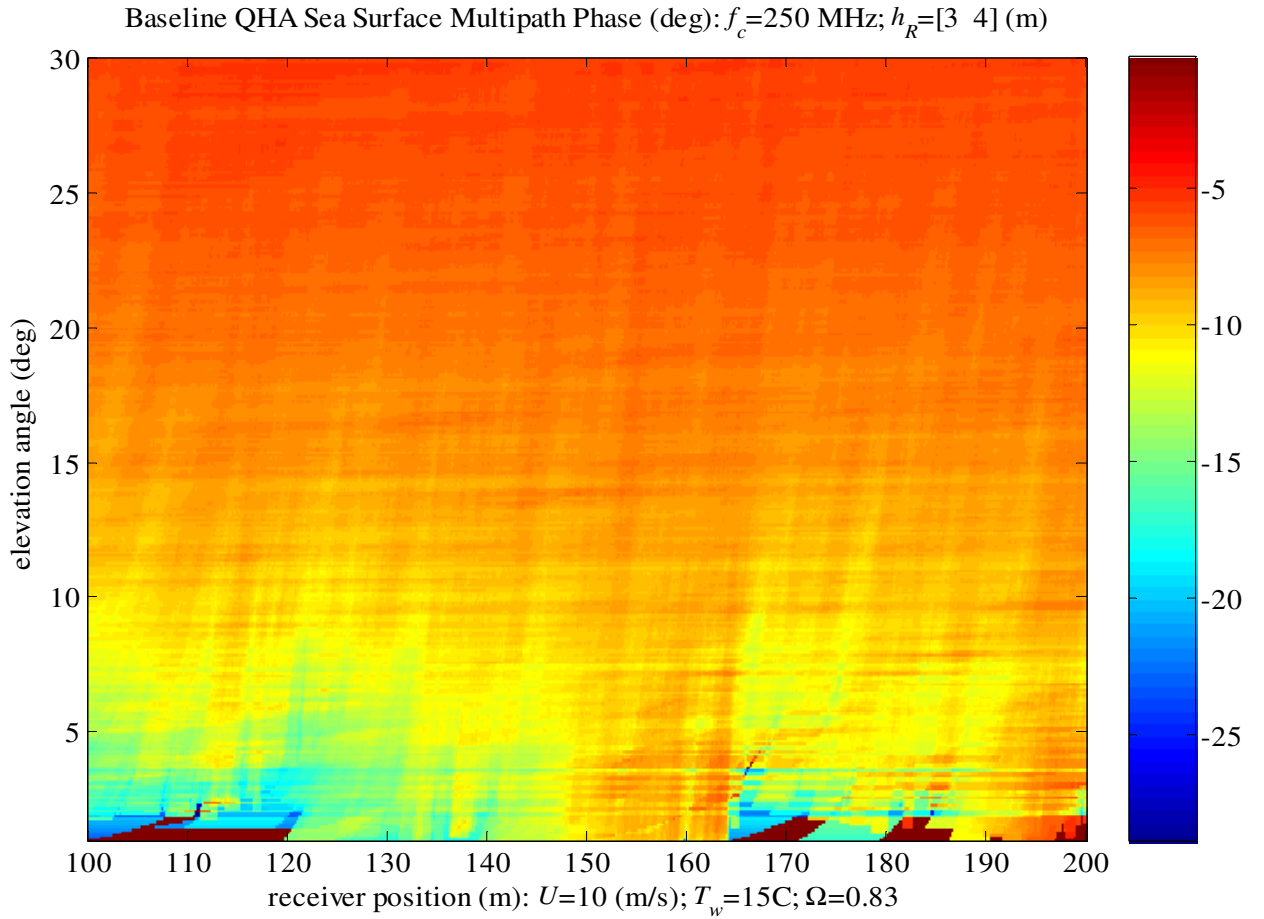


Figure 51: Multipath phase; baseline QHA; wind at 10 m/s.

Figures 52 and 53 plot the phase of the multipath as the wind decreases or the sea surface gets smoother. These plots show that as the sea surface smoothes out, the phase stabilizes at each elevation angle. Consequently, these phase plots make the obvious observation that rougher seas cause greater phase variations than a smooth sea.

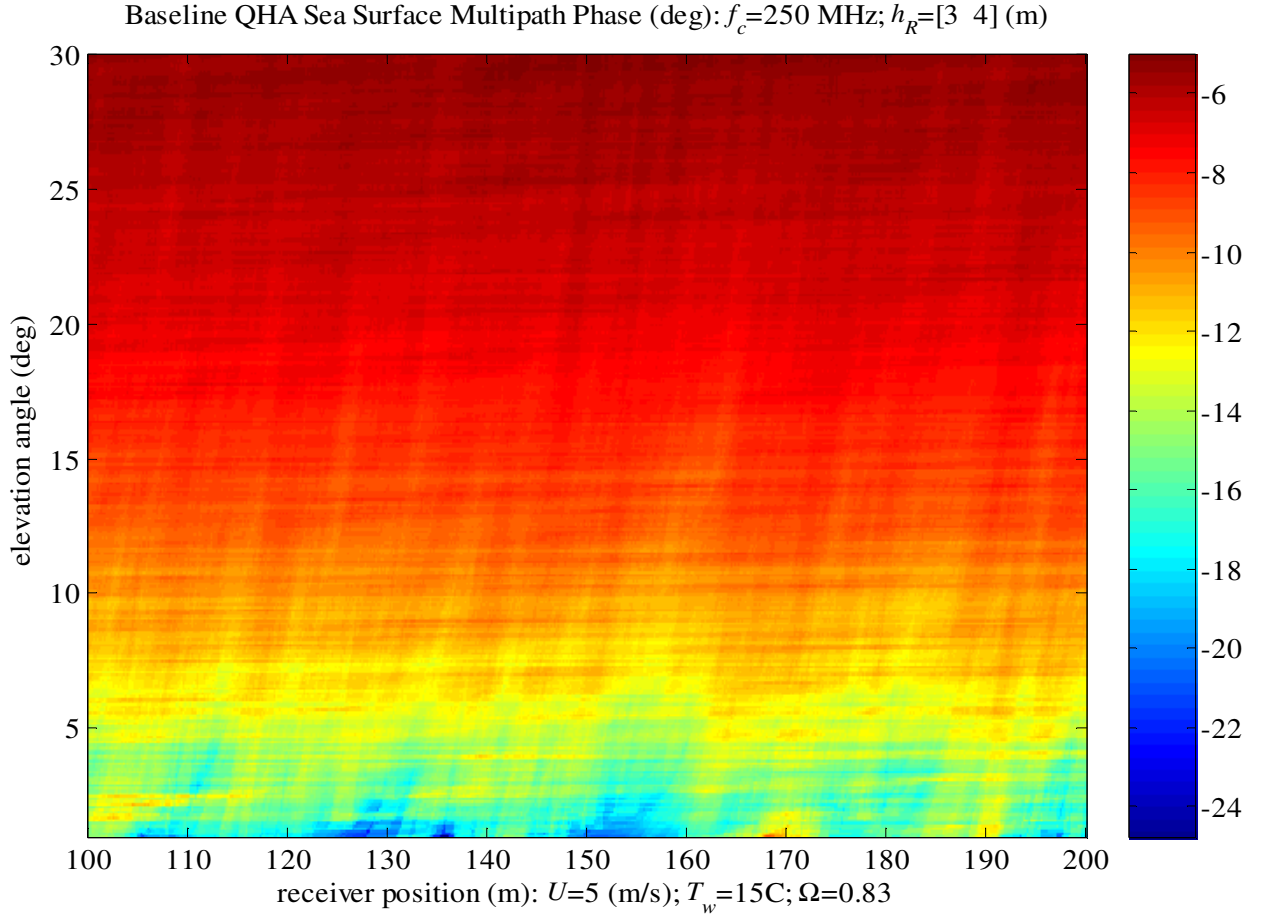


Figure 52: Multipath phase; baseline QHA; wind at 5 m/s.

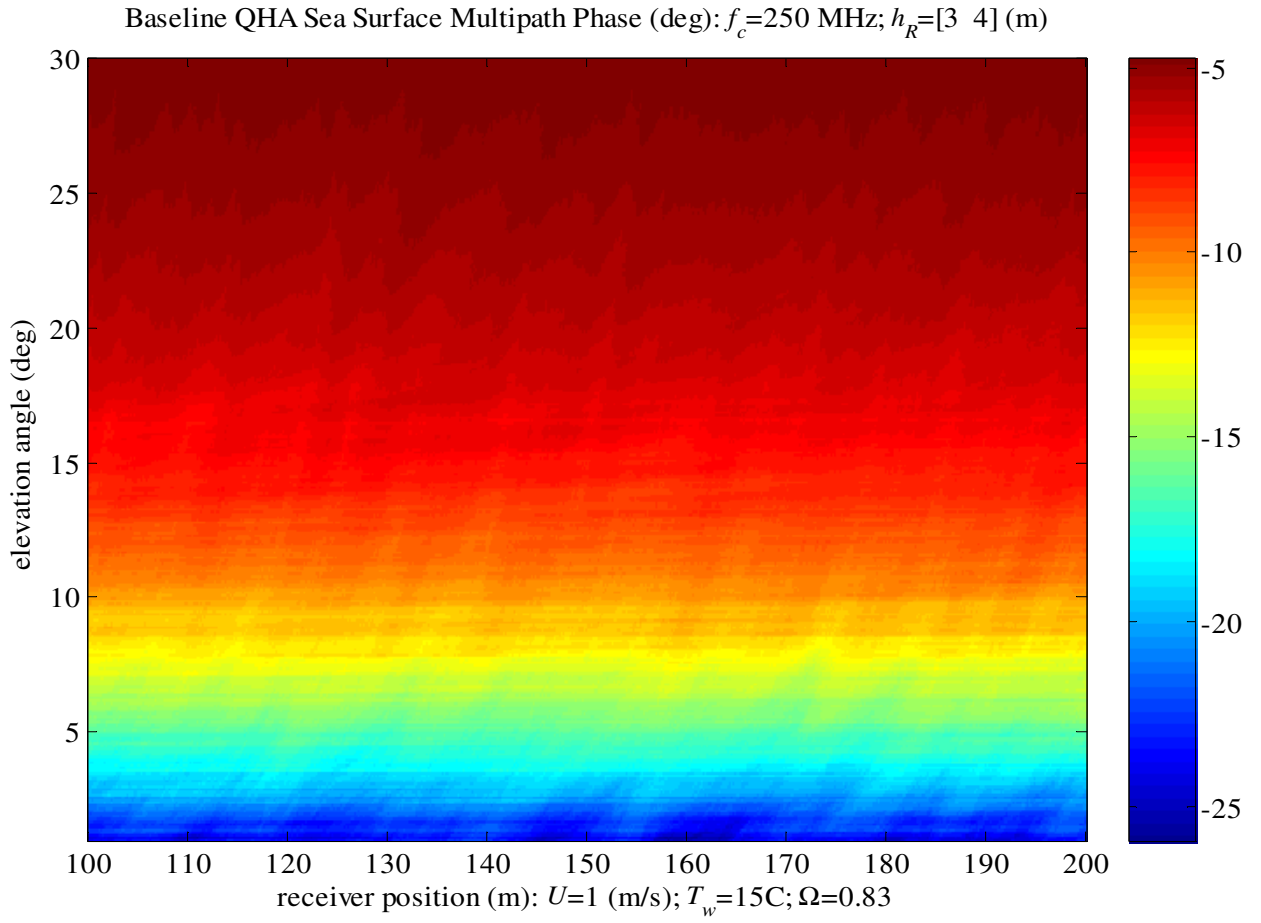


Figure 53: Multipath phase; baseline QHA; wind at 1 m/s.

7.4 Multipath Correlation

Figure 54 estimates the correlation of the specular multipath. Each elevation angle of the transmitter produces a multipath noise. The plot shows the correlation between these multipath noises as a function of elevation angle. Although some correlation is visible at the lower angles, there is also little power at these angles. In the upper angles, the multipath is decorrelated, except at the highest angles.

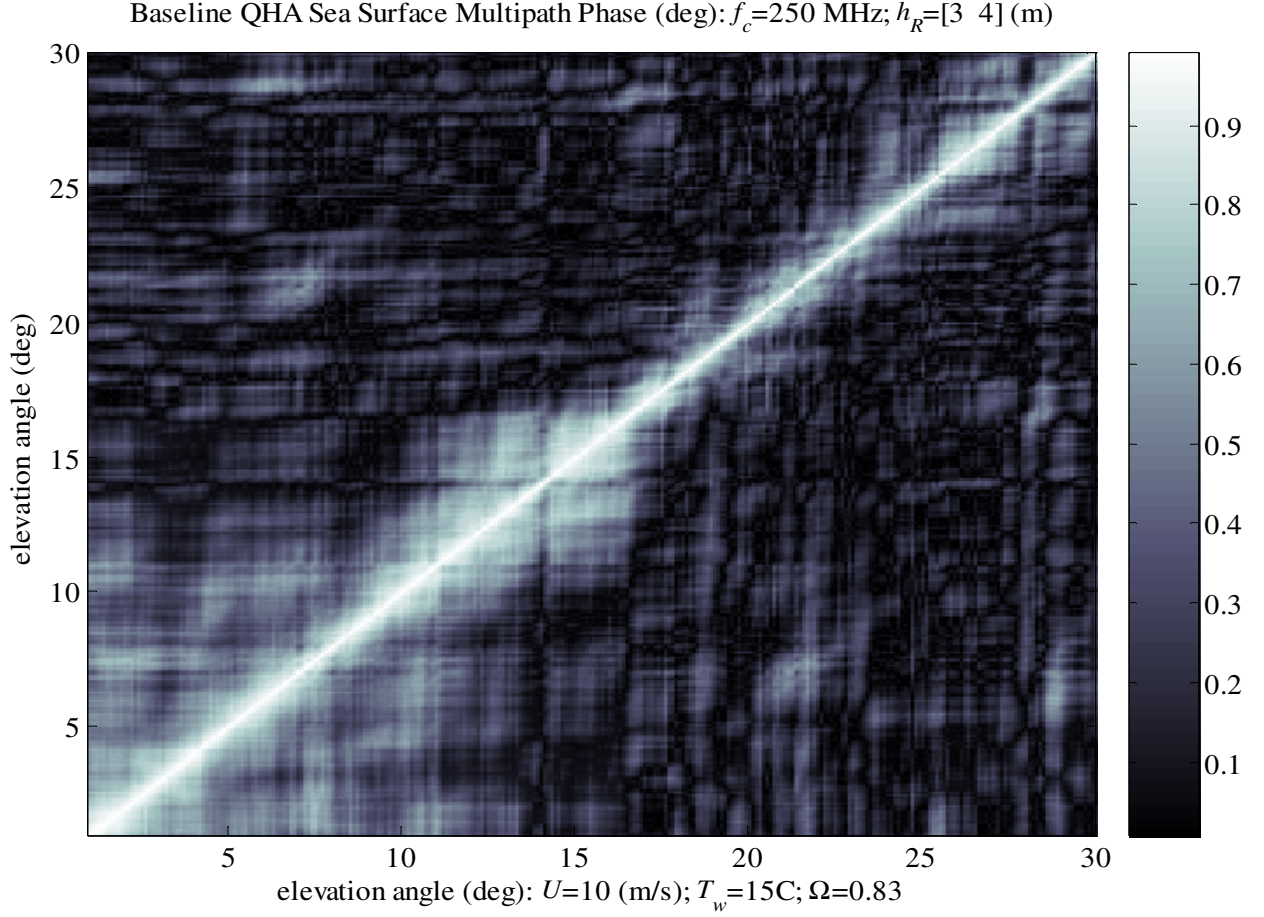


Figure 54: Multipath correlation; baseline QHA; wind at 10 m/s.

Figure 55 shows a decorrelation in the low-elevation angles as the wind decreases or the sea surface gets smoother. Correlation in the upper angles increases.

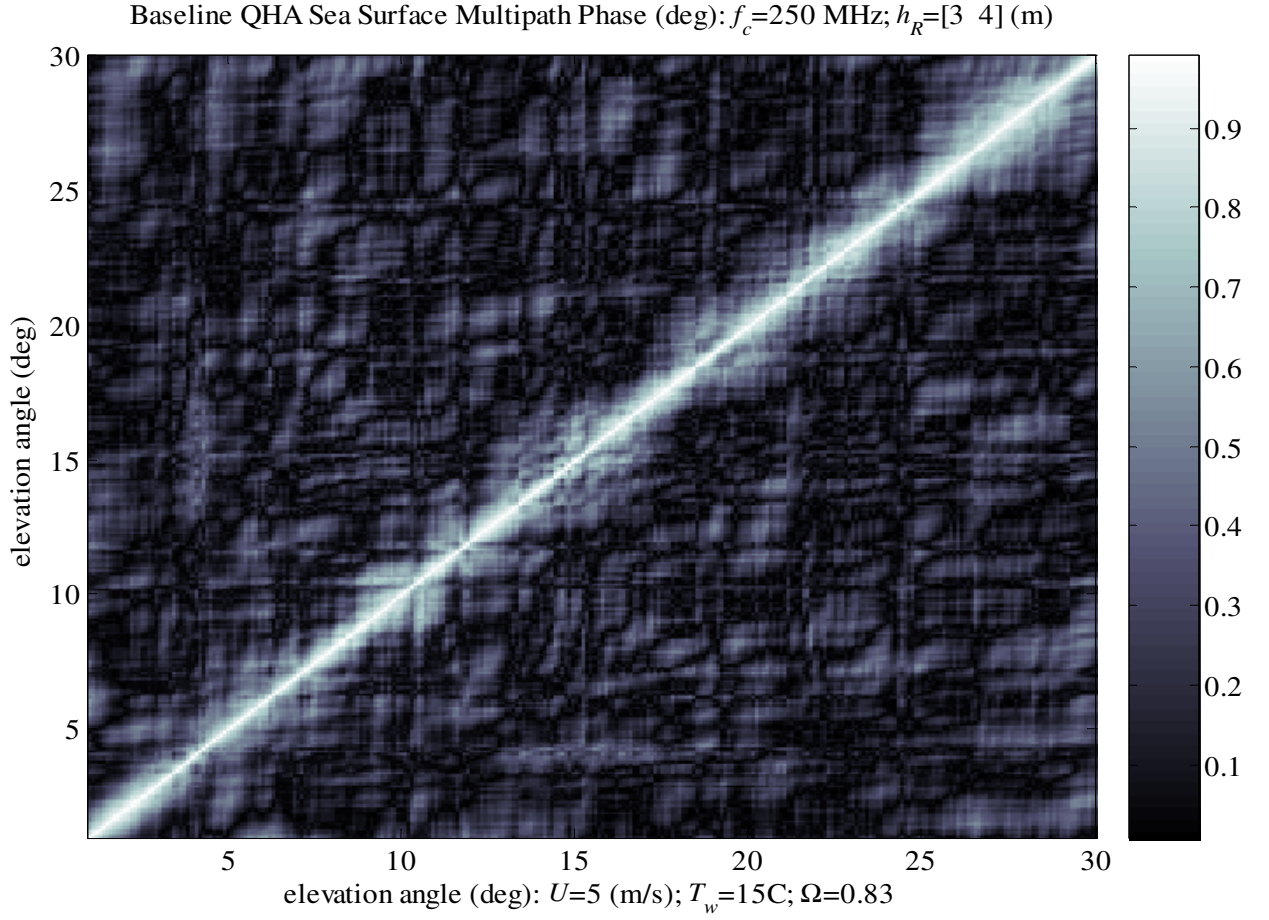


Figure 55: Multipath correlation; baseline QHA; wind at 5 m/s.

Figure 56 shows that as the sea smooths further when the wind decreases to 1 m/s, the multipaths are starting to correlate at the upper elevation angles. One conjecture to explain these correlation plots is to consider a single small plate tangent to the sea surface. Even if the plate reflects into the antenna aperture, slight perturbations of the plate will throw the reflecting ray out of the antenna aperture. Consider now a collection of reflecting plates. On a rough sea surface, this set can reflect into the aperture over a small variation in the transmitter's elevation angle. A large shift in elevation angle illuminates an entire different set of reflectors—an uncorrelated set. Only when the surface is sufficiently smooth do large patches of the sea surface become correlated.

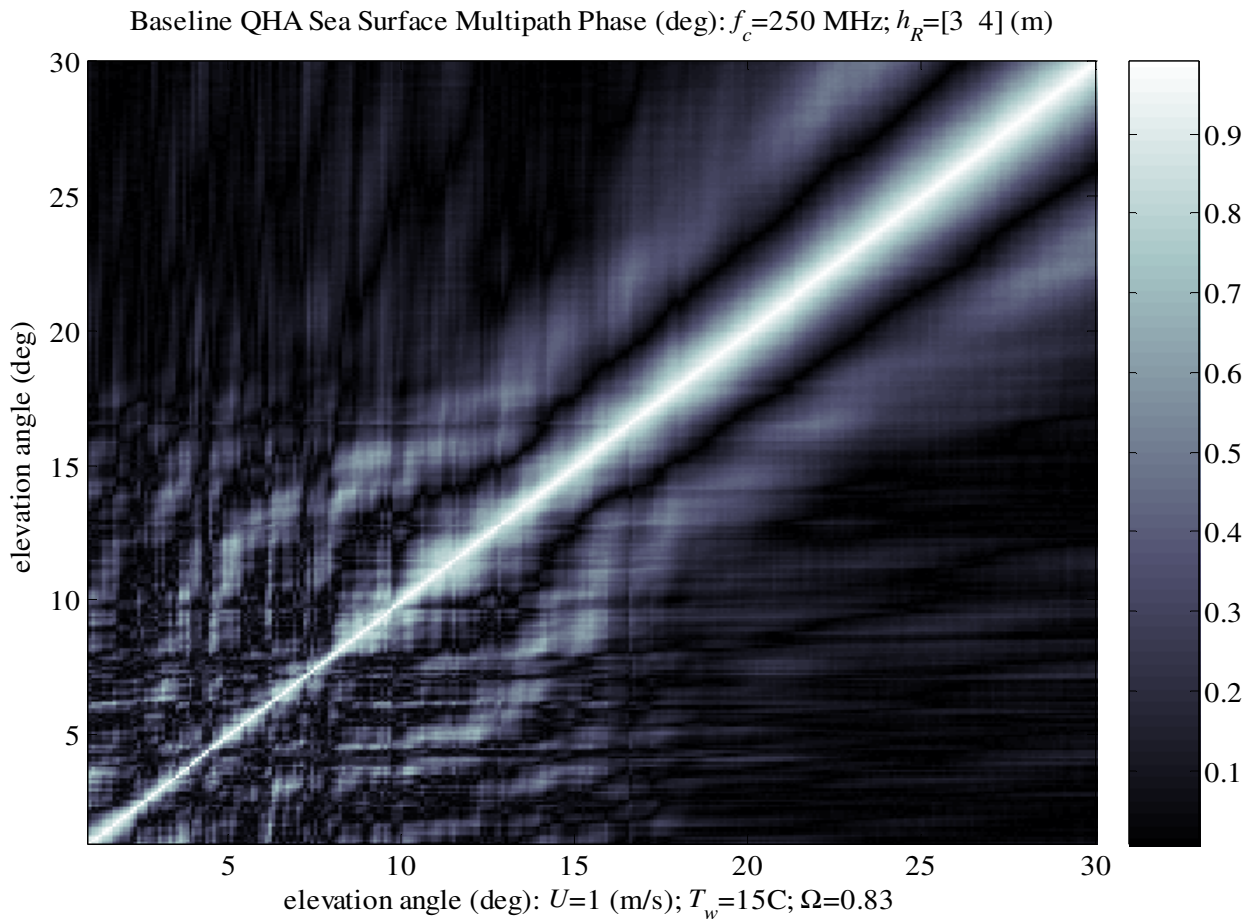


Figure 56: Multipath correlation; baseline QHA; wind at 1 m/s.

7.5 Multipath Envelope

Identifying the envelope of noise is a cottage industry for the communication and radar engineers. This envelope identification problem forms an excellent interface between these engineers and the statisticians. The statistician's non-parametric density estimators require an immense number of independent samples. The envelopes that the communication engineers do acquire are typically narrow band. Consequently, the independence assumption is lost. Therefore, extending the non-parametric density estimator to handle narrow-band time series is an excellent research topic.

Figure 57 presents an Average Shifted Histogram (ASH) estimate of the probability density of the multipath envelope [39]. The ASH estimates the unknown probability distribution using a weighted average of shifted histograms. The plot shows all samples of $\{|h(r, \theta)|\}$ lumped into a single sample. The problem with this approach is that each “channel”—each $\{|h(r, \theta)|\}$ for a fixed elevation angle θ —has a different power level that confounds the identification problem.

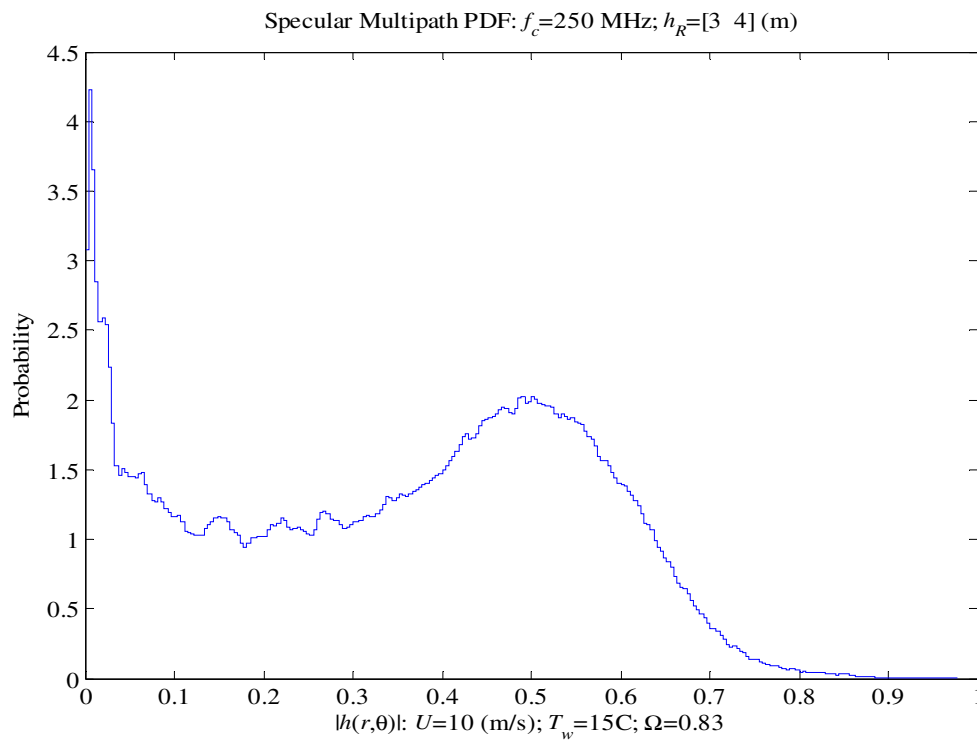


Figure 57: Multipath probability density estimate; baseline QHA; wind at 10 m/s.

Figure 58 is an estimate of the root-mean-square (RMS) power or standard deviation of the multipath at each elevation angle. Power is lost by shadowing and blocking at the low angles.

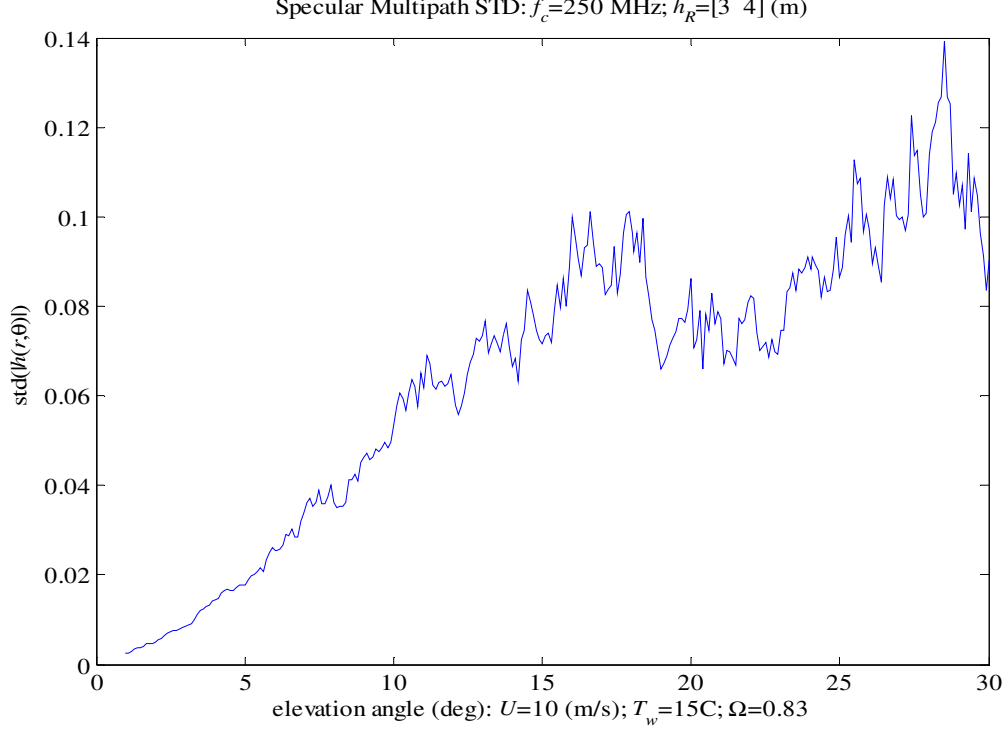


Figure 58: Multipath standard deviation estimate; Baseline QHA; wind at 10 m/s.

To reduce the effects of power confounding the envelope identification problem, each channel is normalized by dividing by its estimated standard deviation. Figure 59 applies a Rician goodness-of-fit (GOF) test to these normalized channels. This plot tests if these normalized channels all share the same Rician density [36, Eq. 5.59]:

$$p(u) = \frac{u}{\sigma^2} \exp\left(-\frac{u^2 + s^2}{2\sigma^2}\right) I_0\left(\frac{us}{\sigma^2}\right),$$

where u denotes the envelope, s denotes the magnitude of the specular component, and σ^2 is the variance of the uncorrelated noise. These parameters are estimated from the normalized channels and appear on the plot. This plot also provides an estimate of the specular-to-diffuse ratio or K factor [36, Eq. 5.60]:

$$K = 10 \log_{10}\left(\frac{s^2}{2\sigma^2}\right) \quad [\text{dB}].$$

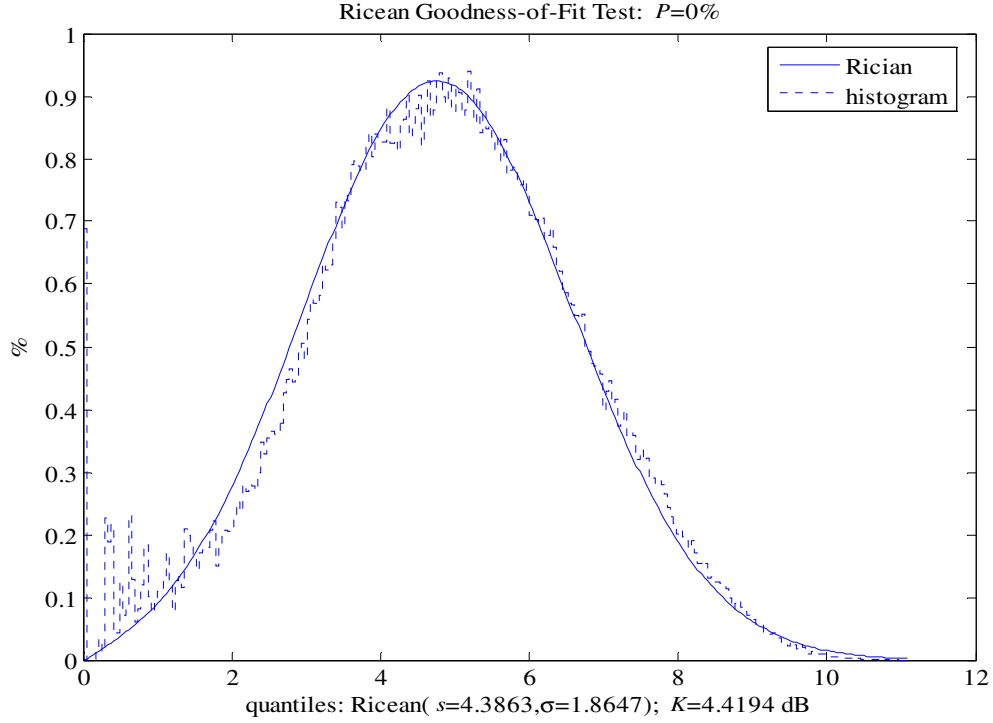


Figure 59: Ricean GOF of the normalized multipath; baseline QHA; wind at 10 m/s.

This GOF test compares a histogram against the Rician density. The fit is good for the large magnitudes but deviates from Rician in the small magnitudes. The GOF is the *observed significance level* P that measures how closely the histogram follows the Rician density. Small values of the observed significance level ($P < 0.1$) reject the fit. However, a key assumption for the significance test is that the samples be independent. Dropping the independence assumption is a basic research problem for GOF theory. No data pruning or whitening was applied to this multipath. Consequently, the low significance is confounded by the correlations in the multipath.

Because of the good fit over the large envelope values, it is natural to remove the small magnitudes from the multipath and test again. Specifically, the multipath channels with $\theta < 5^\circ$ were omitted from the normalized multipath. Figure 60 shows a GOF applied to this multipath with the low angles removed. The small deviations from Rician are omitted, but the fit is still not tight on the Rician density.

Similar results can be obtained with the Weibull and the K -distributions. This blind fitting is a **pitfall of non-parametric identification**. That is, it is very tempting to throw densities at the multipath and hope to “get lucky” with a large significance level. In contrast, some clutter research mixes physics and statistics to

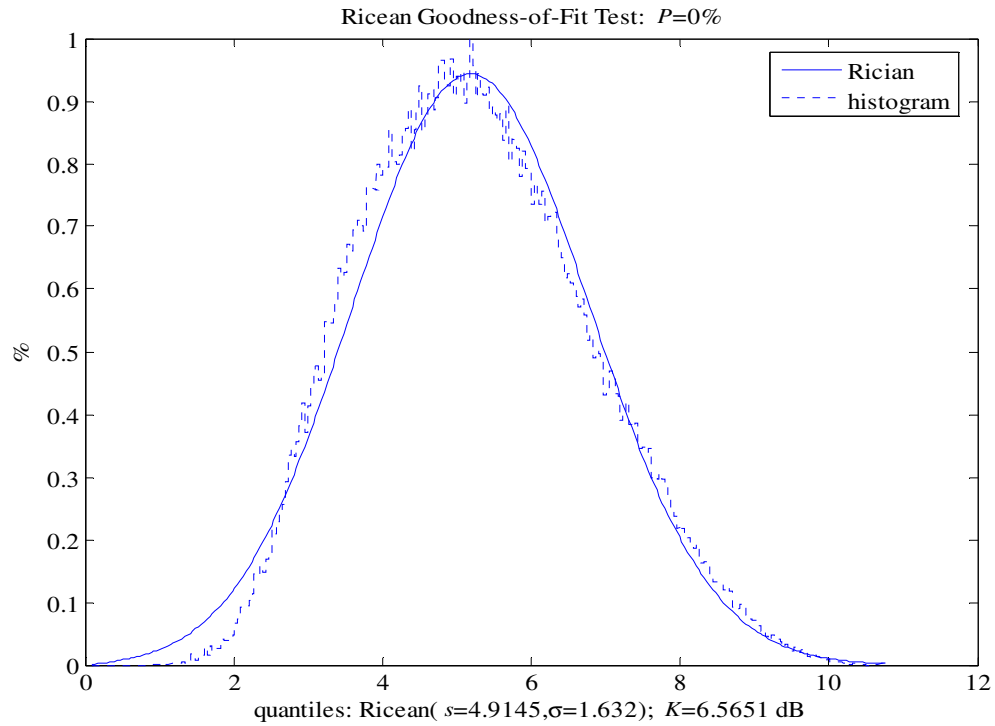


Figure 60: Rician GOF of the normalized multipath—angles below 5° omitted; baseline QHA; wind at 10 m/s.

arrive at new GOF test and distributions [12]. A fully rational approach asks:

Given the Gaussian sea surface and specular scattering, what envelope density will we see based on physical reasons?

This question is part of the larger question that asks how the sea-surface statistics (i.e., the variance of the wave heights, the surface correlation length, the slope statistics) map to the multipath statistics.

8 Modeling Issues

This model provides qualitative simulations of specular sea-surface multipath impinging upon a surface-level antenna. This ray model assumes the following:

- Ray propagation
- Narrow-band receiver
- Transmitter and receiver aligned with the wind
- Fully developed sea
- Signal wavelength approximately 1 meter
- Local tangent-plane scattering
- No surface aerosol effects
- No atmospheric effects
- Far-field antenna pattern

The surface-level antenna and narrow-band receiver force the time delays of each ray into the nanosecond regime. A receiver with a kilohertz bandwidth cannot register these time delays. Consequently, the time delays can be ignored.

Aligning the transmitter and receiver with the wind over a fully developed sea puts the rays orthogonal to the bulk of the waves. Consequently, most scattering is in-plane. In-plane scattering lets us scatter from a “slice” of the sea surface rather than scattering over the entire surface.

The transmitter’s wavelength λ_T is approximately 1 meter. Consequently, scattering from sea-surface features that are less than 0.1 meters in size can be ignored. Because the capillary waves are millimeter size, the rough-surface coefficient is approximately 1 and limits the diffuse scattering. For this reason, specular reflecting patches are limited to 0.1 meters in size. The tangent-plane scattering does not model the curvature effects of the surface nor the reflections off the top of the waves. Likewise, the effects of the surface aerosols, whitecaps, bubbles, and spray are omitted.

The atmosphere is assumed to deliver plane waves to the scattering region around the antenna. Consequently, atmospheric scintillation and ducting are omitted. Only straight-line ray propagation is used.

Finally, antenna-to-surface coupling effects are ignored by keeping the antenna at least a wavelength away from the local surface. These simplifications allow a straight-forward model description:

Each tangent plane on the surface may reflect a specular ray into the antenna aperture, provided the ray is not shadowed or blocked.

This simple model provides a qualitative description of the specular multipath effects for a surface-level antenna. In light of these approximations, it makes little sense to polish a small model part in the presence of the following large-scale effects and approximations. First, the antenna pattern changes as the antenna gets closer to the sea surface. The simulations of this report kept the base of the antenna 3 meters above the mean sea surface. The largest significant wave height was 2 meters, which allows the waves to come within a wavelength of the antenna. The sea surface will modify the antenna pattern. For example, a tilting ground plane will distort the main beam. Consequently, the near-field effects of the sea surface must be computed whenever the antenna is within a wavelength of the sea surface.

Second, two-dimensional propagation over the sea surface “slice” needs to be compared to 3-D propagation over the full sea surface. However, comparing ray models does not address the quality of the simulations. The real comparison should be between the ray models and high-quality, partial-differential equation models. For example, the Variable Terrain Radio Parabolic Equation (VTRPE) code handles the rough-surface scattering over a slice of a sea surface [37]. Comparing the two-dimensional ray model against the VTRPE simulation provides a practical assessment of the ray model propagating over a slice. If this comparison is “good enough” for communication simulations, extending the ray model to 3-D propagation is justified.

Third, this multipath simulation is essentially local. We assume that *plane waves* carry the signal into the scattering region. This plane-wave assumption implies that there is no distortion by ducting or ionospheric scintillation—even at low elevation angles. This assumption is questionable and the effect on the signal needs to be quantified and compared to the multipath effect. For example, measurements of low-elevation SATCOM signals over a sea surface have been carried out at the Scripps Pier in La Jolla by Ken Anderson, SSC San Diego [2]. Figure 61 reports on the received SNR as a function of increasing satellite range or, equivalently, decreasing elevation angle as the GPS satellite heads down toward the horizon. Reexamination of these measurements or conducting a similar field experiment provides a low-cost measurements that can

- quantify the plane-wave assumption
- recover the multiplicative noise
- benchmark the multipath simulations

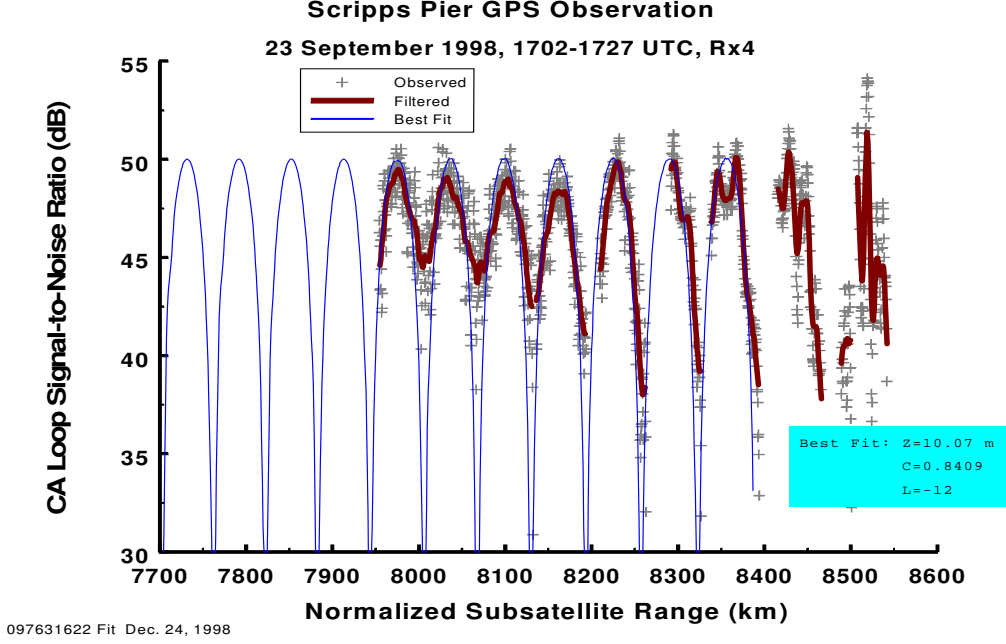


Figure 61: Measured GPS satellite SNR at a sea-level receiver.

Fourth, the antenna measurements need to be upgraded to include the *effective length* or *effective height* \mathbf{h} of the antenna [32, Chapter 14]. The effective length determines the received voltage V_0 at the antenna's terminals as

$$V_0 = \mathbf{h}^T \mathbf{E}_i,$$

where \mathbf{E}_i is the incident electric field plane wave [40]. If the electric field is composed several plane waves, say

$$\mathbf{E}_i = \mathbf{E}_{i,1} + \mathbf{E}_{i,2} + \mathbf{E}_{i,3},$$

the effective length the antenna's response to each plane with the correct relative phase is

$$V_0 = \mathbf{h}^T \mathbf{E}_{i,1} + \mathbf{h}^T \mathbf{E}_{i,2} + \mathbf{h}^T \mathbf{E}_{i,3}.$$

Therefore, getting the effective length by the Numerical Electromagnetic Code or measurements is necessary for multipath simulations.

Finally, regardless of how the multipath is computed, there is fascinating research linking the sea-surface statistics—the standard deviation of the height, the correlation length, the distribution of the slopes—to the statistics of the specular multipath.

A Back Reflections

These simulations use only reflections from the sea surface in front of the surface-level antenna. Here, “front” refers to the region between the receiver and the transmitter. If the transmitter’s elevation angle is small and the sea is relatively smooth, almost no rays ever reflect from behind the antenna. This appendix quantifies this claim so that these rare events can be omitted.

Figures 62 and 63 display reflections arriving from behind the antenna. Both figures show a relatively steep wave face is needed to bounce a low-angle ray back into the surface-level antenna. The relevant question is—how common are such steep waves?

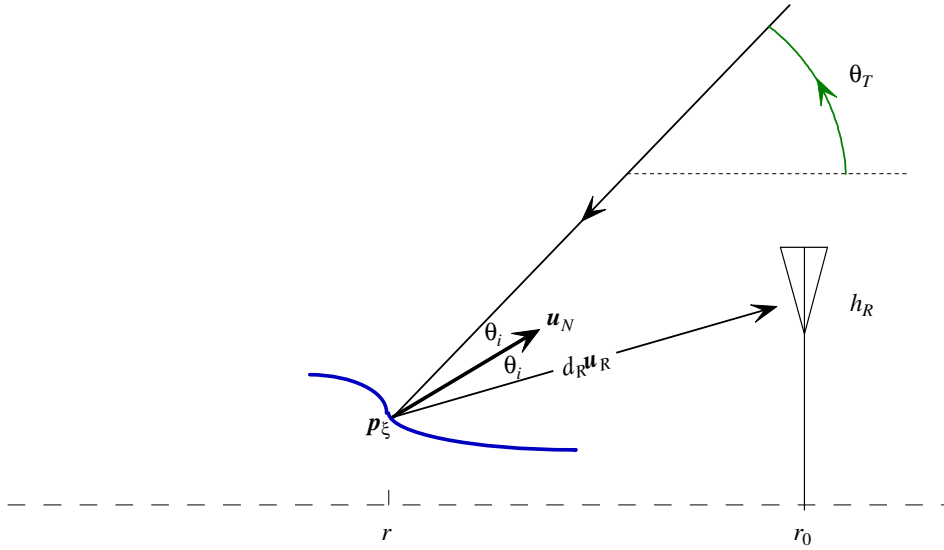


Figure 62: Back reflection—upper ray.

Recall that $\zeta(\mathbf{r})$ denotes the sea surface and $\zeta(r_1, 0)$ denotes a slice of the sea surface. The slopes of the waves,

$$\zeta'(r_1, 0) := \frac{\partial \zeta}{\partial r_1}(r_1, 0),$$

have a Gaussian distribution. For the sea surface with the wind of 10 m/s, $\zeta'(r_1, 0)$ is zero mean with a estimated standard deviation

$$\sigma_{\zeta'} \approx 0.1616.$$

Assume a back reflection shown in Figure 62 occurs at sea level with a transmitter at 30 degrees elevation. The wave slope required typically exceeds -75 degrees but the

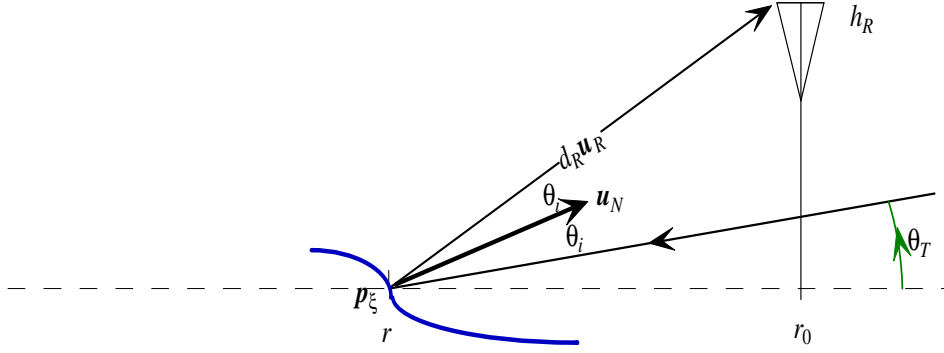


Figure 63: Back reflection—lower ray.

smallest wave slope is -38 degrees. The probability of such a slope is small:

$$\text{Prob}[\tan(\text{slope}) < -40^\circ] = \text{Prob}[\text{slope} < \text{atan}(-38^\circ)] = 2.1 \times 10^{-5}.$$

The probability that **no** back reflections of this type happen over the 100 meters behind the receiver's antenna exceeds 98%—assuming that no shadowing or blocking occurs. Consequently, if the transmitter's elevation angle is small and the sea is relatively smooth, the back reflections are ignored.

References

- [1] Allen, J. and S. L. Hobbs [1997] Spectral Estimation of Non-Stationary White Noise, *Journal of the Franklin Institute*, 334B(1), pages 99–116.
- [2] Anderson, Kenneth D. [2000] Determination of Water Level and Tides Using Interferometric Observations of GPS Signals, *Journal of Atmospheric and Oceanic Technology*, 17(8), pages 1006–1015.
- [3] Banner, Michael L. [1990] Equilibrium Spectra of Wind Waves, *Journal of Physical Oceanography*, Volume 20, pages 966–984.
- [4] Beard, C. I. [1961] Coherent and Incoherent Scattering of Microwaves from the Ocean, *IRE Transactions on Antennas and Propagation*, AP-9, pages 470–483.
- [5] Beard, C. I., I. Katz, and L. M. Spetner [1956] Phenomenological Vector Model of Microwave Reflection from the Ocean, *IRE Transactions on Antennas and Propagation*, AP-4, pages 162–167.
- [6] Beckmann, Petr [1968] *The Depolarization of Electromagnetic Waves*, The Golem Press, Boulder, CO.
- [7] Bello, Philip A. [1963] Characterization of Randomly Time-Variant Linear Channels, *IEEE Transactions on Communications Systems*, CS-11, pages 360–393.
- [8] Bello, Philip A. [1965] Some Techniques for the Instantaneous Real-Time Measurement of Multipath and Doppler Spread *IEEE Transactions on Communication Technology*, COM-13, pages 285–292.
- [9] Bello, Philip A. [1969] A Troposcatter Channel Model, *IEEE Transactions on Communication Technology*, COM-17, pages 130–137.
- [10] Bello, Phillip A. [1973] Aeronautical Channel Characterization, *IEEE Transaction on Communications*, COM-21, pages 548–563.
- [11] Biglieri, Ezio and Valerio Zingarelli [1994] Coded Modulation for Channels Affected by Noise, Correlated Rice Fading, and Doppler Frequency Shift, *IEEE International Conference on Communications ICC '94*, pages 18–22, New Orleans, LA.
- [12] Billingsley, J.B., A. Farina, F. Gini, M.V. Greco, L. Verrazzani [1999] Statistical analyses of measured radar ground clutter data *IEEE Transactions on Aerospace and Electronic Systems*, 35(2), pages 579–593.
- [13] Boithias, Lucien [1987] *Radio Wave Propagation*, McGraw-Hill Book Company, New York, NY.

- [14] Department of Geosciences, University of Houston, Houston, TX. Geol 3377: Introductory Oceanography,
<http://www.uh.edu/~rmaddock/3377/3377lecture9b.html>
- [15] Didascalou, Dirk, Martin Döttling, Norbert Geng, and Werner Wiesbeck [2003] An Approach to Include Stochastic Rough Surface Scattering Into Deterministic Ray-Optical Wave Propagation Modeling, *IEEE Transactions on Antennas and Propagation*, 51(7), pages 1508–1515.
- [16] Donelan, Mark A. and Willard J. Pierson [1987] Radar Scattering and Equilibrium Ranges in Wind-Generated Waves with Application to Scatterometry, *Journal of Geophysical Research*, 92(C5), pages 4971-5029.
- [17] Durden, Stephen L. and John F. Vesecky [1985] A Physical Radar Cross-Section Model for a Wind-Driven Sea with Swell, *IEEE Journal of Oceanic Engineering*, OE-10(4), pages 445–451.
- [18] Fores, Giulio Ruffini [1999] Surface Waves in the Ocean
www.ieec.fcr.es/gps/KNMI_slides/node24.html.
- [19] Gel'fand, I. M. and N. Ya. Vilenken [1964] *Generalized Functions*, Volume 4, Academic Press, New York, NY.
- [20] Katz, Isadore [1963] Radar Reflectivity of the Ocean Surface for Circular Polarization, *IEEE Transactions on Antennas and Propagation*, pages 451–453.
- [21] Kerr, Donald (ed) [1951] *Propagation of Short Radio Waves*, McGraw-Hill Book Company, NY.
- [22] Kilgus, C. C. [1968] Multielement, Fractional Turn Helices *IEEE Transactions on Antennas and Propagation*, AP-16(4), pages 499–500.
- [23] Kilgus, C. C. [1969] Resonant quadrafilary helix *IEEE Transactions on Antennas and Propagation*, AP-17(3), pages 349–351.
- [24] Kinsman, Blair [1965] *Wind Waves*, Dover Publications, Inc., New York, NY.
- [25] Long, Maurice W. [1983] *Radar Reflectivity of Land and Sea*, Second Edition, Artech House, Inc., Deham, MA.
- [26] Loo, Chun and Norman Secord [1991] Computer Models for Fading Channels with Applications to Digital Transmission, *IEEE Transactions on Vehicular Technology*, 40(4), pages 700–707.
- [27] Massel, Stanisław R. [1996] *Ocean Surface Waves: Their Physics and Prediction*, World Scientific, Singapore.

- [28] Matthews, P. A. [1965] *Radio Wave Propagation: V.H.F and Above*, Chapman and Hall Ltd, London.
- [29] Miyagaki, Yoshiya, Norihiko Morinaga, Toshihiko Namekawa [1983] Double Symbol Error Rates of M -ary DPSK in a Satellite-Aircraft Multipath Channel, *IEEE Transactions on Communications*, COM-31(12), pages 1285–1289.
- [30] Mott, Harold [1986] *Polarization in Antenna and Radar*, John Wiley & Sons, New York, NY.
- [31] North, Richard C. and James R. Zeidler [1994] Multichannel Adaptive Equalization for Improved Performance in LOS Digital Radio, *1994 IEEE Military Communications Conference*, Fort Monmouth, NJ.
- [32] Orfanidis, Sophocles J. [2004] *Electromagnetic Waves and Antennas*, ECE Department, Rutgers University, 94 Brett Road, Piscataway, NJ 08854-8058. <http://www.ece.rutgers.edu/~orfanidi/ewa>
- [33] Parsons, David [1992] *The Mobile Radio Propagation Channel*, Halstead Press, New York, NY.
- [34] Pritchard, Wilbur [1997] The Calculation of System Temperature for a Microwave Receiver, in *The Communications Handbook*, Jerry D. Gibson (editor), CRC Press.
- [35] Proakis, John G. and Masoud Salehi [1994] *Communication Systems Engineering*, Prentice Hall, NJ.
- [36] Parsons, J. David [1992] *The Mobile Radio Propagation Channel*, John Wiley & Sons, New York.
- [37] Ryan, Frank J. [1996] Variable Terrain Radiowave Parabolic Equation (VTRPE) RF propagation, *SPAWAR TR 1999*.
- [38] Sainati, Robert A., John J. Groppelli, Ralph C. Olesen, Andrew J. Stanland [1982] A Band-Switched Resonant Quadrifilar Helix, *IEEE Transactions on Antennas and Propagation*, AP-30(5), pages 1010–1013.
- [39] Scott, David W. [1992] *Multivariate Density Estimation*, John Wiley & Sons, Inc., New York, NY.
- [40] Sinclair, George [1950] The Transmission and Reception of Elliptically Polarized Waves, *Proceedings of the IRE*, 38, pages 148–151.
- [41] Sjöblom, Anna [2004] Influence of Sea Surface Waves on the Marine Atmospheric Boundary Layer, *Nordic Meteorological Meeting*, June 7–11, 2004, Bergen, Norway.

- [42] Stutzman, Warren L. [1993] *Polarization in Electromagnetic Systems*, Artech House, Boston, MA.
- [43] Zavorotny, Valery U. and Alexander G. Voronovich [1998] Two-Scale Model and Ocean Doppler Spectra at Moderate- and Low-Grazing Angles, *IEEE Transactions on Antennas and Propagation*, 46(1), pages 84–92.

Approved for public release; distribution is unlimited.